HETEROGENEOUS KINETICS OF SOME ATMOSPHERICALLY RELEVANT REACTIONS. EXPERIMENTS AND MODELING

PAR

Lukas GUTZWILLER

Ingénieur physicien diplômé EPF
originaire de Bâle (BS)

para Cristina

"Entia non sunt multiplicanda,
praeter necessitatem."

Wilhelm von Occam (1285-1350)
"doctor invincibilis"

Abstract

A low pressure reactor (Knudsen cell) coupled to molecular beam modulated mass spectrometry was used to study the heterogeneous kinetics of the following three systems: (1) NO_2 on amorphous carbon, (2) H_2O vapor on ice and (3) gaseous HCl on ice. The first system was investigated at ambient temperature while the two last ones were investigated at temperatures typical of the stratosphere, that is roughly between 160 and 220K. The solid phase samples correspond to model surfaces whose physico-chemical properties come very close to the ones of atmospheric particulates.

Firstly, we studied the interaction of gaseous NO_2 with three different commercial samples of amorphous carbon having widely differing physicochemical properties. Using *in situ* laser-induced fluorescence, the only major product was unambiguously determined to be NO with the oxidation product of carbon apparently remaining on the surface. Probing the gas phase with mass spectrometry (MS), both pulsed valve dosing and steady state experiments were performed and revealed a complex reaction mechanism for both the uptake as well as product formation. The initial uptake coefficient γ_0 for NO_2 was $(6.4\pm2.0)\cdot10^{-2}$ and proved to be identical within experimental uncertainty for all three types of amorphous carbon. The initial NO_2 uptake rate was independent of the mass of the carbon sample and scaled with its external geometrical surface. Applying a simple chemical kinetic model to both pulsed dosing and steady state experiments resulted in an effective surface for uptake on amorphous carbon ranging between a factor of 2.8 to 8.4 larger than the geometrical surface area, but inversely proportional to the measured BET surface area of the three types of amorphous carbon. This means that the amorphous carbon with the highest BET surface (FW2) had the lowest external surface for NO_2 adsorption. The chemical kinetic model included competing processes between Langmuir-type adsorption and inhibition controlling the adsorption kinetics of NO_2 and revealed that the NO generation rate differed greatly between the three carbon samples examined. All samples showed saturation effects of differing degree that were partially reversible through prolonged pumping at 10^{-4} Torr and/or heating. Virgin amorphous carbon samples did not take up H_2O vapor at 20 mTorr, and no HONO and/or HNO_3 was detected in simultaneous NO_2/H_2O exposure experiments. CO and CO_2 were detected when a sample previously exposed to NO_2 was heated by an incandescent lamp. Moreover, upon heating such a sample, a MS signal m/e 62 originating from NO_3 and/or N_2O_5 was detected.

In addition to the experiments conducted on the three commercial carbon samples, we carried out uptake experiments of NO_2 on acetylene soot. Originating from the flame of an acetylene burner, this soot was freshly deposited on glass dishes before each experiment. The initial uptake coefficient γ_0 for NO_2 was measured to be $(3.0\pm1.1)\cdot10^{-2}$ is smaller by a factor of two compared to γ_0 observed in the uptake on commercial samples whose mass was a factor of 10 higher. In addition to NO, a net formation of HONO (m/e 47) was observed. This HONO formation is strongly dependent

on the instantaneous water desorption from the sample as well as on the NO_2 partial pressure in the reactor. On the other hand, it is not enhanced by an external water flow which did not show any interaction with the carbon sample. Upon heating the sample using an incandescent lamp, significant amounts of water desorbed, suggesting that the water vapor had condensed into the micropores of the soot during combustion. No quantitative results are presented yet. However, as no correlation between HONO formation and NO partial pressure has been observed so far, we suggest a reaction mechanism that only involves NO_2 and H_2O but no NO: $2 NO_2 (g) + H_2O <=> HONO + HNO_3$

In a second study, the kinetics of condensation and evaporation of water on ice was determined in the temperature range of 170 to 220K. The rate of evaporation F_{ev} corresponds to the evaporation of 70±10 monolayers of H_2O per second at 200K. The condensation rate constant k_c has a negative activation energy of -3.1±1.5kcal/mol which is significantly larger than the one recently measured by Haynes et al. We report the first real time kinetic measurements of water condensation on ice at stratospherically relevant temperatures. At temperatures above 160K, pulsed dosing experiments show a dose dependence of the condensation rate coefficient. For example, the condensation rate coefficient increases by a factor of five with a 1000 fold increase of the H_2O dose from $1 \cdot 10^{15}$ to $1 \cdot 10^{18}$ molecules per pulse at 180K. This pressure dependence of the condensation rate constant may be explained by an autocatalytic mechanism involving the competition of two condensation channels. These two channels feed two different surface species, one of which leads to autocatalytic condensation. This mechanism gives insight into the manner in which a gas phase molecule is stepwise incorporated into tetrahedrally coordinated bulk ice.

In a third and ongoing study, the uptake kinetics of HCl on ice has been investigated by pulsed valve experiments in the temperature range of 180 to 210K and are discussed as a function of the state of the surface. In fact, some of the pulsed valve experiments present a relaxation to a steady state level. It is shown that this level originates from the evaporation of a liquid solution corresponding to a temperature specific HCl concentration. The threshold of the injected dose leading to this solution layer is estimated to be $8 \cdot 10^{14}$ molecules. This threshold corresponding to a fraction of a monolayer may be explained by the formation of small domains along grain boundaries or other lattice imperfections. Within detection limit, no difference in k_{eff} has been observed for pulses on the solution or on a previously exposed sample without formation of the solution. In the case of pulses forming a solution layer, a fraction of 20±20% of the injected molecules remain permanently adsorbed on the surface. In the temperature range from 210 to 180K, the pulsed valve experiments yield values of k_{eff} roughly between 5 and $25s^{-1}$ and an activation energy of -1.6±0.7kcal/mol which are consistent with the values observed by Flueckiger in steady state experiments using the 15mm escape aperture (k_{uni} varying from 12 to $23s^{-1}$ and an activation energy of -1.9±0.25 kcal/mol).

Version Abrégée

Un réacteur à basse pression (cellule Knudsen) couplé avec un spectromètre de masse est utilisé pour l'étude de la cinétique hétérogène des trois systèmes suivants: (1) NO_2 sur du carbone amorphe, (2) vapeur d'eau sur la glace et (3) HCl gazeux sur la glace. Le premier système est étudié à température ambiante alors que les deux derniers sont étudiés à des températures situées entre 160 et 220K typiques de la stratosphère. Les échantillons solides sont des surfaces modèles possédant des propriétés physico-chimiques proches de celles des particules atmosphériques.

Tout d'abord, on a étudié l'interaction du NO_2 gazeux avec trois échantillons commerciaux de carbone amorphe ayant des propriétés physico-chimiques complètement différentes. En utilisant *in situ* la fluorescence induite par laser, le seul produit majeur identifié est le NO, le produit d'oxydation du carbone restant apparemment sur l'échantillon. En examinant la phase gazeuse par spectrométrie de masse (MS), les deux types d'expériences, c.-à-d. à vanne pulsée et à l'état stationnaire, ont révélé un mécanisme de réactions complexes pour l'adsorption, tout comme pour la formation du produit. Le coefficient de collage initial γ_0 pour le NO_2 est de l'ordre de $(6.4\pm2.0)\cdot10^{-2}$ et se révèle être identique dans la plage d'erreur pour tous les trois types de carbone amorphe. Le taux de collage initial du NO_2 est indépendant de la masse, mais dépend linéairement de l'aire géométrique de l'échantillon. L'application d'un modèle cinétique simple aux deux types d'expériences (vanne pulsée et état stationnaire) nous donne une surface d'adsorption effective, qui est un facteur 2.8 à 8.4 fois plus grande que l'aire géométrique de l'échantillon. Par contre, cette surface est inversement proportionnelle à la surface BET de chacun des trois échantillons de carbone amorphe. Le modèle cinétique révèle que l'adsorption du NO_2 est contrôlée par un processus de type Langmuir et un processus inhibiteur. Il révèle que le taux de production diffère fortement entre les trois échantillons de carbone étudiés. Tous les échantillons montrent des phénomènes de saturation à des degrés différents qui sont partiellement réversibles lors du pompage prolongé à 10^{-4} Torr et/ou lors du chauffage. Les échantillons de carbone amorphe vierges n'adsorbent pas la vapeur de H_2O à 20 mTorr, et aucun HONO et/ou HNO_3 n'est détecté lors de l'exposition simultanée au NO_2/H_2O. CO et CO_2 sont détectés lorsque du carbone amorphe, préalablement exposé au NO_2, est chauffé par une lampe incandescente. De plus, on détecte un signal MS m/e 62 dû au NO_3 et/ou au N_2O_5.

En plus des expériences menées sur les trois échantillons commerciaux de carbone, on a effectué des expériences d'adsorption de NO_2 sur la suie d'acétylène. Générée par la flamme d'un chalumeau à l'acétylène, cette suie est fraîchement déposée sur une plaque de verre avant chaque expérience. Le coefficient de collage initial γ_0 pour le NO_2 mesuré à $(3.0\pm1.1)\cdot10^{-2}$ est deux fois plus petit que celui observé pour les échantillons commerciaux, pour lesquelles une masse d'un facteur 10 plus élevée a été utilisée. En plus du NO, une formation nette de HONO (m/e 47) est observée. Cette formation de HONO est fortement dépendante de la désorption instantanée d'eau

provenant de l'échantillon, tout comme de la pression partielle de NO2 dans le réacteur. D'autre part, elle n'est pas augmentée par un débit d'eau externe. L'eau n'interagit pas avec l'échantillon de carbone. Aucun résultat quantitatif n'est présenté pour le moment. Toutefois, puisqu'aucune relation entre la formation du HONO et la pression partielle de NO n'est observée, on suggère un mécanisme de réaction dans lequel intervient NO2 et H2O, mais pas NO: $2\,NO_2\,(g) + H_2O \iff HONO + HNO_3$

Dans une deuxième étude, la cinétique de condensation et d'évaporation de l'eau sur la glace a été déterminée dans l'intervalle de température entre 170 et 220K. Le taux d'évaporation F_{ev} correspond à une évaporation de 70±10 monocouches de H2O par seconde à 200K. La constante de vitesse correspondant à la condensation k_c possède une énergie d'activation négative de -3.1±1.5kcal/mol qui est sensiblement plus élevée que celle mesurée récemment par Haynes et al. Nous présentons les première mesures en temps réel de la cinétique de condensation de l'eau sur la glace à des températures typiques de la stratosphère. A des températures supérieures à 160K, les expériences à vanne pulsée montrent une dépendance en dose du coefficient de condensation. Par exemple, le coefficient de condensation augmente par un facteur cinq lorsque la dose de H2O varie de trois ordres de grandeur passant de $1 \cdot 10^{15}$ à $1 \cdot 10^{18}$ molécules par pulse à 180K. Cette dépendance en pression du taux de condensation peut être expliquée par un mécanisme autocatalytique avec deux processus concurrentiels. Ces deux processus alimentent deux différents types de site à la surface dont un mène à la condensation autocatalytique. Ce mécanisme démontre de quelle façon les molécules de la phase gazeuse sont incorporées pas à pas dans la structure tétraédrique de la glace massique.

Dans un projet en cours, la cinétique d'adsorption de HCl sur la glace a été étudiée par des expériences à vanne pulsée dans l'intervalle de température entre 180 et 210K. Elle est discutée en fonction de l'état de la surface car en effet, certaines expériences à vanne pulsée présentent une relaxation vers un niveau stationnaire. On peut montrer que ce niveau stationnaire est dû à l'évaporation d'une solution caractérisée par une concentration en HCl spécifique de la température. Le seuil de dose injectée menant à la formation de cette couche de solution est estimé à $8 \cdot 10^{14}$ molécules par pulse. Il correspond à une fraction de monocouche et peut être expliqué par la formation de petits domaines le long des joints de grain ou d'autres imperfections du réseau cristallin. Dans les limites de détection, aucune différence n'a été observée dans les k_{eff} mesurés, que les pulses aient été injectés sur cette solution ou sur un échantillon précédemment exposé au HCl sur lequel la solution ne s'est pas formée. Dans le cas des pulses menant à une couche de solution, une fraction de 20±20% de la dose injectée reste adsorbée sur la surface de manière permanente. En passant d'une température de 210 à 180K, les valeurs de k_{eff} déterminées dans des expériences à vanne pulsée varient approximativement entre 5 et 25s^{-1}, correspondant à une énergie d'activation de -1.6±0.7kcal/mol. Ces observations sont en accord avec les valeurs déterminées par Flueckiger dans des expériences à l'état stationnaire utilisant l'orifice de 15mm (k_{uni} variant de 12 à 23s^{-1} correspondant à une énergie d'activation de -1.9±0.25 kcal/mol).

Table of Contents

Chapter One - Introduction

In October 1995, the three atmospheric scientists Molina, Rowland and Crutzen were awarded the Nobel Prize in chemistry for their "contribution to our salvation from a global environmental problem that could have catastrophic consequences". They showed that human activities such as the use of spray cans and air conditioners can imperil the fragile ozone layer that protects the world from the dangerous ultraviolet radiation of the sun. In fact, without the protective layer of stratospheric ozone, animals and plants could not exist on land. Significant depletion of ozone can cause increased skin cancer, weakening of the immune system of humans and damage to plants, crops in particular, with famine as its worst consequence.

In 1970, Crutzen showed that nitrogen oxides accelerate the rate of ozone depletion. In fact, another threat to the ozone layer came from the supersonic aircraft planned in the 1970s, which would be capable of releasing nitrogen oxides among other emissions right in the middle of the ozone layer at altitudes of 20 km [1].

In 1974, Molina and Rowland realized that the chemically inert chlorofluorocarbons (CFC) could gradually be transported up to the ozone layer by diffusion and convection, there to be met by such intensive ultra-violet light that they would be separated into atomic and molecular fragments, notably chlorine atoms [2]. They calculated that if human use of CFC gases was to continue at an unaltered rate the ozone layer would be depleted by many percentage points after some decades. Molina and Rowland's report led to certain restrictions on CFC release during the late 1970s and early 1980s, banning all non-essential uses of CFCs. There was not any real urgency in the international negotiations on release restrictions until 1985 when the real shock came. That year, Farman and coworkers noted a drastic depletion of the ozone layer over the Antarctic [3], the "ozone hole". The depletion was, at least periodically, far greater than expected from earlier calculations of the CFC effect. The debate among researchers now intensified. The surprisingly rapid depletion of the ozone layer on the time scale of tens of days over Antarctica could not be explained by transport processes or by gas phase chemical reactions. Scientists realized that an alternative mechanism had to exist which would accelerate the decomposition of ozone. Crutzen, among many other colleagues identified the missing part of the mechanism as chemical reactions on the surface of atmospheric particles in the stratosphere. Thus, the Antarctic ozone depletion appears to be connected with the extremely low prevailing temperatures, which lead to condensation of

water and nitric acid to form "polar stratospheric clouds" (PSCs). The ozone-
decomposing chemical reactions are greatly reinforced in the presence of
atmospheric particles. This early insight has led to an exciting new branch of
atmospheric chemistry, namely "heterogeneous" chemical reactions on particle
surfaces.

While the collision frequency of a gas molecule with an average particle is only
about $10^{-5}s^{-1}$ in the stratosphere, there are considerably more such collisions in
the troposphere. The collision frequency in a highly polluted urban environment
is about $1s^{-1}$, and loss processes with efficiencies of even 10^{-4} can compete with
homogeneous gas phase processes. Thus heterogeneous chemistry is not only
important in stratospheric ozone depletion but also in the troposphere where
atmospheric particulates are abundant near the ground. The most common
particles are sulfate, nitrate and ammonium aerosols and soot particles (carbon)
[4]. While ozone in the stratosphere has a protective role, tropospheric ozone is a
component of the photochemical smog which is a well known nuisance to humans
adversely affecting the air quality. The photochemical smog is furthermore
controlled by the availability of NO_x (the sum of nitric oxide NO and nitrogen
dioxide NO_2), hydrocarbons and sunlight.

The ozone problem also has interesting connections with the issue of how
mankind is affecting the climate. In fact, tropospheric trace gases like ozone,
methane and also CFCs contribute to the greenhouse effect, that is, they absorb
infrared light [5]. This trapping of light contributes then to the warming of the
atmosphere and to the subsequent climate change. Numerous model calculations
have shown that the climate is specially sensitive to changes in the ozone content
in the troposphere. Here the ozone content has increased markedly during the
past century, chiefly because of the release of nitric oxide, carbon monoxide and
gaseous hydrocarbons from vehicles and industrial processes and from the
combustion of biomass in the tropics. However, it is not known so far, which
heterogeneous reactions, if any, may be contributing to the formation of
tropospheric ozone. The global atmosphere is a very complex system of
interacting radiative, transport and chemical processes so that the only reliable
tool for projections into the future are sophisticated models. The question which
heterogeneous reaction may or may not be important under atmospheric
conditions must be answered by such models.

        The plume of jet aircraft is another example where heterogeneous
reactions may be important in the troposphere and which are studied intensively
[6]. It seems that the formation of visible contrails at temperatures below -40°C
is due to nucleation of water vapor on local soot and sulfuric acid aerosols.

In order to make accurate model predictions on the evolution of the atmosphere, reliable input data is needed. This data not only includes the best available knowledge of the physico-chemical composition of the atmosphere, but also a sound understanding of the transport and radiation processes as well as of the chemical transformations involved. So far, relatively accurate data are available describing homogeneous gas phase reactions [7]. As shown in the summary of historical events above, reliable projections of the future state of the atmosphere have been partly limited because of the lack of data in heterogeneous chemistry. The goal of this study is to assess the kinetics, that is the chemical mechanism, of certain heterogeneous reactions that are thought to be important in the atmosphere. Assuming the mechanism determined in laboratory experiments does not change abruptly as a function of reactant density, it may then be extrapolated to atmospheric conditions. In the present laboratory experiments on model surfaces whose physico-chemical properties come close to the ones of atmospheric particulates, we determined uptake coefficients or reaction probabilities. These two parameters express the fraction of gas phase molecules which remain adsorbed or lead to reaction after collision with the surface. Hence, these parameters allow one to calculate the chemical transformation of an air parcel at a known ratio of the total particle surface in that volume [8].

The present work has been performed using a low pressure reactor (Knudsen cell) coupled to molecular beam modulated mass spectrometry. In addition to traditional steady state experiments, we performed pulsed valve experiments in which a burst of molecules is injected and their effusion from the reactor is followed in real time. Based on this newly developed technique and using model surfaces, the heterogeneous kinetics of the following three systems has been studied: (1) NO_2 on amorphous carbon, (2) H_2O vapor on ice and (3) gaseous HCl on ice. The first system was investigated at ambient temperature while the two latter ones were investigated at temperatures "typical" of the lower stratosphere, that is roughly between 160 and 220K. The present work is divided into four main chapters in whose introduction the atmospheric relevance of the above systems is discussed in detail, and references are given.

Firstly, we studied the interaction of gaseous NO_2 with three different commercial samples of amorphous carbon having widely differing physico-chemical properties. NO_x and solid carbon are major pollutants of the atmosphere [9], [10] and thus their interaction might be of importance. A dominant fraction of both pollutants, NO_x and soot, is of anthropogenic origin

and stems from the oxidation of carbon containing fuels during combustion [11], [12]. The majority of NO_x is emitted as NO which subsequently may be oxidized by ozone to form NO_2. NO_2 may be photolyzed to yield NO. From a chemical point of view, the plume of a combustion source could potentially be a very reactive medium for heterogeneous processes because water vapor, NO_x, unburnt hydrocarbons, carbonaceous aerosol particles, and a number of oxidizing species in small concentrations such as O atoms, OH and HO_2 radicals are emitted into the atmosphere.

In the present study, the only major product of the interaction of NO_2 with carbon soot was unambiguously determined to be NO with the oxidation product apparently remaining on the carbon surface. By probing the gas phase using mass spectrometry (MS), both pulsed valve and steady state experiments were performed and revealed a complex reaction mechanism for both the uptake as well as product formation. This complex mechanism has been assessed using a detailed chemical kinetic model.

In addition to the experiments conducted on three commercial carbon samples, we carried out uptake experiments of NO_2 on "acetylene soot". Originating from the flame of an acetylene burner, this soot was freshly deposited on glass dishes before each experiment. This sample preparation allowed homogeneous deposition on the sample dishes of much smaller mass of soot than using the commercial samples. The initial uptake coefficient for NO_2 was found to be smaller by a factor of two compared to the one observed in the uptake on commercial samples whose mass used in the uptake experiments was higher by a factor of 10, however. In addition to NO as a reaction product, the formation of nitrous acid (HONO) was observed depending on the water content of the soot sample. Nitrous acid is an important atmospheric trace species whose chemistry remains largely uncharacterized and whose source is still uncertain [13], [14]. In the troposphere, and in particular near cities, HONO has been found to accumulate during nighttime to reach levels as high as 8ppb just before sunrise [15], [16]. Because HONO is easily photolyzed, it may be responsible for a "pulse" of hydroxyl radicals at sunrise that sets off the diurnal oxidative chain reactions [17], [18].

In a second study, the condensation and evaporation of water on ice was determined in the temperature range of 170 to 220K. Interest in this topic is motivated by its significance in understanding how processes such as cloud formation and growth occur in the atmosphere [19]. The condensation and evaporation coefficients of H_2O on ice have met with increasing interest since recent atmospheric studies have revealed the role of heterogeneous chemistry on ice particles [20], [21], [22], [23]. In particular, the ozone hole over Antarctica in

the spring is intimately linked to the presence of ice particles known as polar stratospheric clouds. Furthermore, the condensation of water vapor also plays an important role in the chemistry occurring in aircraft contrails, especially at high cruise altitude (8 to 15km) [6].

We report the first real time kinetic measurements of water condensation on ice at stratospherically relevant temperatures. By using an autocatalytic mechanism involving the competition of two condensation channels we are able to account for the experimentally observed positive pressure dependence of the rate of condensation. In particular, this mechanism gives insight into the manner in which a gas phase molecule is stepwise incorporated into tetrahedrally coordinated bulk ice.

In a third study, the uptake kinetics of HCl on ice has been investigated by pulsed valve experiments in the temperature range of 180 to 210K and are discussed as a function of the state of the surface. The interaction of HCl with ice is one of the most important heterogeneous "reactions" occurring on the surfaces of polar stratospheric clouds (PSC), because HCl together with $ClONO_2$, both of which are abundant reservoirs of chlorine, may be transformed into Cl_2 which is photolyzed to chlorine atoms catalyzing ozone depletion [21], [22], [24], [25].

The presented pulsed valve experiments reveal the formation of a solution of specific HCl concentration which is suggested to occur along grain boundaries or other lattice imperfections. Moreover, the measured adsorption constant has a slightly negative temperature dependence pointing towards a complex mechanism. Ongoing experiments will guide the model calculations in order to assess this mechanism.

References

[1] Graedel, T. E. and Crutzen, P.J., Atmosphere, climate and change. Scientific American Library, 1995.

[2] Rowland, F. S. and Molina, M. J., Ozone depletion: 20 years after the alarm, Chemical and Engineering News, 72, 8, 1994

[3] J. C. Farman, B. G. Gardiner, J. D. Shanklin, Nature 1985, 315, 207.

[4] B.J. Finlayson-Pitts and J.M. Pitts Jr., Atmospheric Chemistry:
     Fundamentals and Experimental Techniques, John Wiley & Sons, New
     York, 1986.

[5] Campbell, I.M., Energy and the Atmosphere: A Physical-Chemical Approach.
     Second Edition,1986, John Wiley and Sons, Chichester, UK.

[6] AERONOX, The Impact of NOx Emissions from Aircraft Upon the
     Atmosphere at Flight Altitudes 8-15km, editor: U. Schumann, EC-DLR
     Publication on Research related to Aeronautics and Environment,1995.

[7] IUPAC, Evaluated Kinetic and Photochemical Data for Atmospheric
     Chemistry, Suppl. V., R. Atkinson; D.L. Baulch; R.A. Cox; R.F. Hampson,
     Jr.; J.A. Kerr; M.J. Rossi and J. Troe, J. Phys. Chem. Ref. Data, in press.

[8] Turco, R.P.; Toon, O.B.; Hamill, P., J. Geophys. Res., 1989, 94, 16493.

[9] L. A. Barrie, Atmospheric Environment 1986, 20, 643;

[10] A. D. A. Hansen and T. Novakov, J. Atmos. Chem. 1989, 9, 347; A. D. A.
     Hansen, B. A. Bodhaine, E. G. Dutton and R. C. Schnell, Geophys. Res.
     Lett. 1988, 15, 1193.

[11] J. B. Heywood, 1988, Internal Engine Combustion Fundamentals, McGraw
     Hill Book Co., New York; J. B. Heywood, Prog. Energy. Comb. Sci. 1976.
[12] P. Degobert, Automobile et Pollution, Editions Technip, Paris 1992.

[13] Calvert,J.G.; Yarwood,G.; Dunker,A.M., Res. Chem. Intermed. 1994, 20, 463

[14] Platt,U., Nato ASI Series, Chemistry of Multiphase Atmospheric Systems,
     Springer Verlag, 1986.

[15] Perner,D.; Platt,U., Geophys. Res. Lett. 1979, 6, 917.

[16] Harrison,R.M.; Kitto,A.-M. N., Atmos. Environment 1994, 28, 1089.

[17] Jenkin,M.E.; Cox,R.A.; Williams,D.J., Atmos. Environment 1988, 22, 487

[18] Harris, G.W.; Carter, W.P.L.; Winer, A.M.; Pitts, J.N., Environ. Sci. Technology 1982, 16, 414.

[19] Pruppacher, H. R. Microphysics of Clouds and Precipitation; D. Reidel Pub. Co.: Dordrecht, Holland, 1978.

[20] Solomon, S., Rev. Geophys. 1988, 26, 131.

[21] Molina, M.J; Tso, T.-L.; Molina, L.T.; Wang, C.-Y., Science 1987, 238, 1253.

[22] Tolbert, M.A; Rossi, M.J.; Malhotra, R; Golden, D.M., Science 1987, 238, 1258.

[23] R. P. Turco, Atmospheric Effects of Stratospheric Aircraft: A First Program Report, NASA Ref. Publ. 1992, 63, 1272.

[24] Leu, M.-T., Geophys. Res. Lett., 15, 851, 1988.

[25] Hanson, D. R., and A. R. Ravishankara, J. Geophys. Res., 96, 5081, 1991.

Chapter Two - Experimental Setup

2.1 The Principle of the Knudsen Cell Coupled to MS Detection

The present study was carried out by using a low-pressure reactor (LPR) being part of a flowing gas experiment shown schematically in **Figure 2.1**. The basic considerations for the use of this Knudsen reactor is described as follows: the reactor has a sample compartment containing the model surface whose overall bulk chemical composition is identical to or at least comes very close to the one for atmospheric particulates such as combustion aerosols like soot and ice crystals. This sample compartment can be isolated from the main reactor by an O-ring sealed plunger to allow for non reactive reference experiments. The escape aperture can be varied by lowering a plunger-mounted plate with pin holes onto a permanent aperture. This way and by changing the flowrate into the reactor, we may control the densities and residence times of the species in the reactor. Total pressure is kept low enough to ensure that the reactor remains in the molecular flow regime which is dominated by the preponderance of gas-wall collisions compared to gas-gas collisions. It is equipped with two types of entry ports, one of which is a needle valve or a glass capillary, the other is a wide ($\approx$1cm) port onto which a pulsed valve is mounted. The pulsed valve was supplied by General Valve (Series 9, 2mm diameter). The investigations presented in this work have been carried out using three different designs of Knudsen cells, one of which is displayed in **Figure 2.2**. The characteristic parameters of these reactors like volume, area of the sample surface and escape rate constants are presented in each introduction to the chapters 3 to 6. There we also specify additional experimental details such as heating to 340K or using a Teflon coated reactor in order to passivate the reactor walls with respect to potential heterogeneous interaction.

As presented schematically in **Figure 2.1**, molecules escaping through a selected effusion orifice form an effusive (thermal) molecular beam which is coaxially aligned and monitored using an electron-impact quadrupole mass spectrometer (Balzers QMG 420). Prior to ionization, the molecular beam is chopped by a 150 Hz tuning fork or variable speed chopper wheel located in the lower of the two differentially pumped chambers. Phase sensitive detection (PSD) of the modulated component of the ion current was performed using a lock-in amplifier (Stanford Research Systems SR 850). The PSD scheme was used to discriminate the reactant or product effusive molecular beam from the background within the stainless steel chamber housing the mass spectrometer.
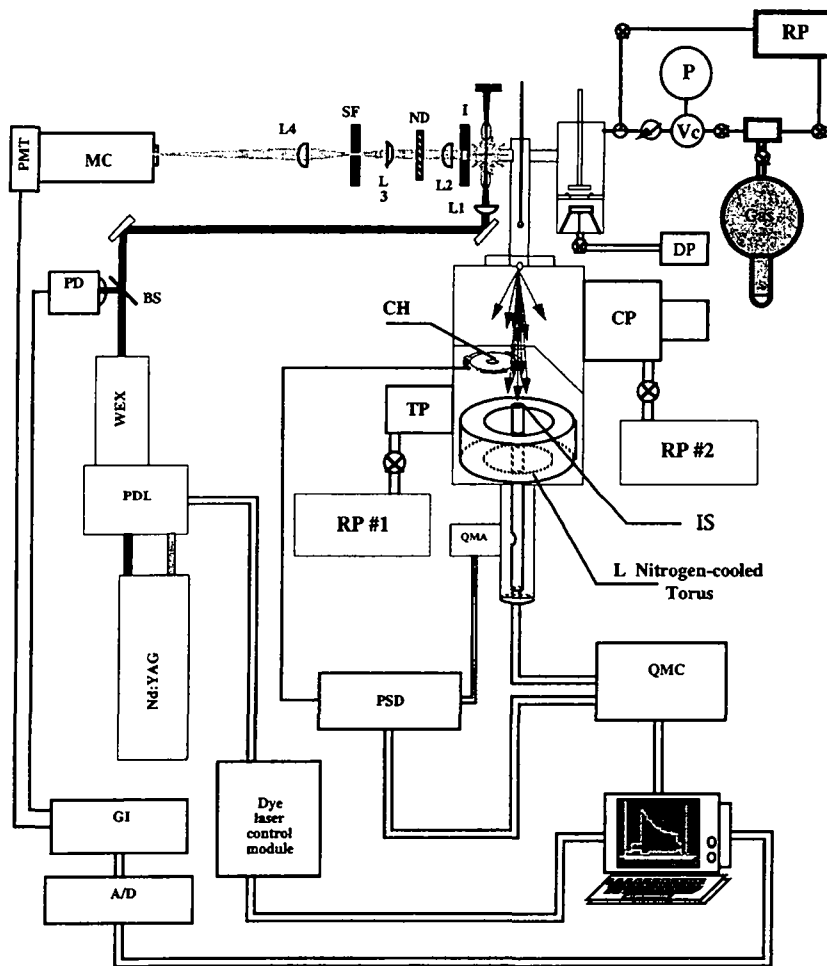
Figure 2.1: Schematic overview of the experimental system. The gas handling manifold (upper right) and LPR part of the system consists of rough pump (RP), pressure measuring device (P) and calibrated volume (Vc). Diffusion pump (DP) is used to evacuate the sample compartment. The tuning fork or chopper wheel (CH) modulates the molecular beam before entering the ion source (IS) of the MS. Cryopump (CP) and turbo molecular pump (TP) differentially pump the high vacuum chamber. The output of the quadrupole mass analyser (QMA) is monitored via the lock-in amplifier (PSD). Alternatively, LIF detection used with monochromator (MC) and a PMT-gated intergrator (GI). The Nd:YAG pumped dye laser (PDL) provides tunable frequency light which may be mixed (WEX) to provide the excitation light.

For certain experiments (especially when dealing with ice), the annular concentric trap in the MS chamber was filled with liquid nitrogen thus lowering the background pressure by additional pumping and subsequent improvement of the signal-to-noise ratio.

The gas-phase densities in the Knudsen reactor are determined by measurements of the flow rate. These are carried out by monitoring the pressure drop in a small calibrated volume (about 40 cm^3) located between the vacuum gas handling line and the inlet valve of the cell. The pressure change is monitored using a 0-100 Torr capacitance manometer (Baratron) for the NO_2 calibration or a 0-2 Torr manometer (Baratron) for the H_2O calibration. The mass-spectrometer signal is thus related to mass-flow which is determined from the pressure change (dp/dt) in the calibrated volume. For the systems using water ice, the water inlet line was heated to the same temperature as the cell (340K) in order to minimize the loss of water vapor onto the walls of the calibrated volume, thus introducing a virtual source term which negatively affects the H_2O flowrate calibration.

The kinetic meter of the Knudsen cell is the escape rate whose rate constant is referred to as k_e; this quantity corresponds to the first-order rate constant for the loss of a gas phase species from the cell by passage through the aperture. The residence time τ and density [G] of a gas phase species are directly related to the value of k_e by the relations $\tau = 1/k_e$ and $[G] = \dfrac{F^o}{k_e \, V}$, where F^o is the flow effusing out of the reactor. The rate of adsorption onto the condensed phase sample surface is determined by competition with the rate of escape; it is therefore necessary to have an accurate measurement of this parameter. Therefore, we conducted experiments with aperture sizes representing an order of magnitude of variation in k_e. The value of k_e associated with an aperture size is determined experimentally by either (1) stopping abruptly the flow of gas into the cell at the inlet and following the first-order disappearance of that species or (2) admitting a short pulse of gas into the cell using the pulsed valve inlet and monitoring the first-order decay. The value has been found to be independent of the admission scheme and scales with the mass as $M^{-0.5}$ as given by gas-kinetic theory: $k_e = \dfrac{\bar{c}}{4 \, V} A_h$ with $\bar{c} = \sqrt{\dfrac{8RT}{\pi M}} = 14'600 \cdot \sqrt{\dfrac{T}{M}}$ (cm/s) the mean speed of a gas phase molecule, A_h the geometric area of the reactor orifice, R the gas constant, T the temperature of the gas and M the molar mass of the molecule under consideration. Deviations from this relation are apparent for very large orifices and are consistent with the hypothesis that a sticky gas like water vapor
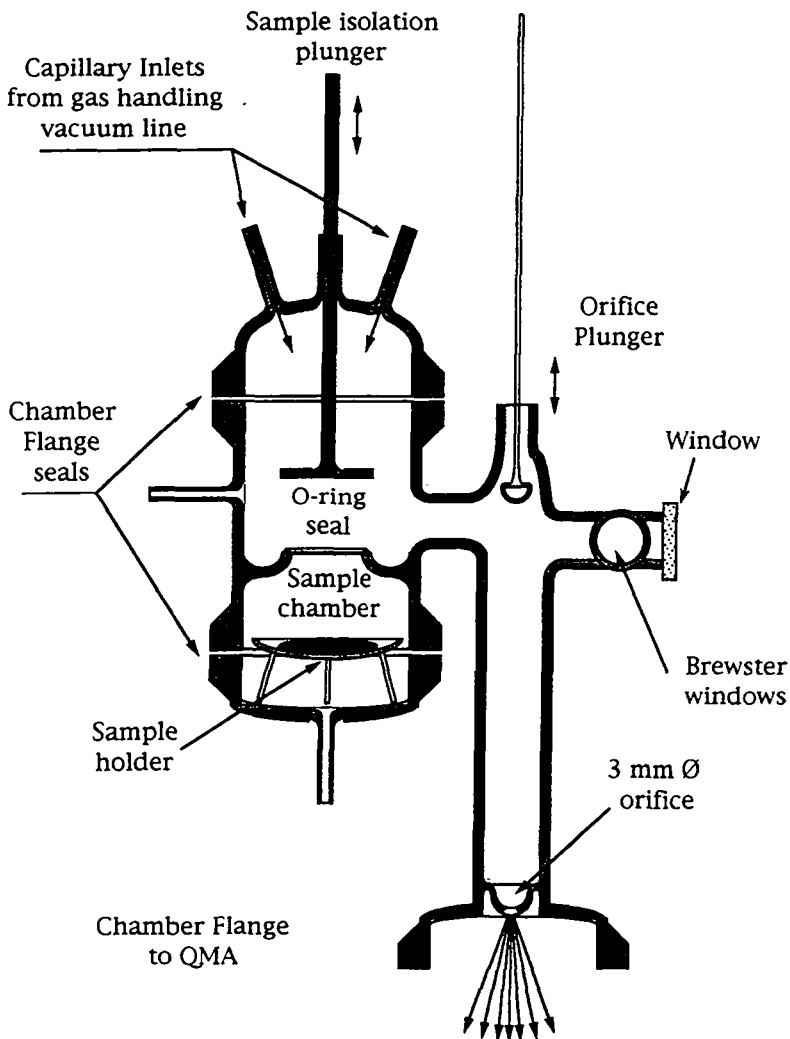
Figure 2.2: Initial design of a low pressure reactor (LPR, Knudsen cell) made out of glass. The total volume of the LPR is 750cm^3, the one of the sample compartment is 215cm^3.

has some non-negligible surface residence time on the walls of the Knudsen reactor. For this reason, the tabulated k_e for H_2O (see introductory part to Chapter 5) were measured with Argon (m/e 40) and mass-scaled to water (m/e 18). According to Fenter [1], deviations from the above relation for large

orifices $\left(\dfrac{A_h}{V} > \dfrac{1}{2000} \text{cm}^{-1} \right)$ are also due to diffusion limitations of the molecules

moving towards the reactor orifice.

Another important parameter is the collision frequency of the gas phase molecules with the sample surface. This sample collision frequency is calculated as $\omega = \dfrac{\bar{c}\, A_s}{4V}$, where the area of the reactor orifice A_h in the formula for k_e is replaced by the geometric area of the sample surface A_s.

2.1.1 Steady State and Pulsed Valve Experiments

The partial pressure in the LPR is given by the balance of source terms such as the flow rate of the gas into the LPR and sink terms such as the rate of effusion through the escape orifice and the heterogeneous loss of the species on the reactive surface. In the absence of a reactive surface, the flowrate into the reactor (F^i) equals the rate of effusion out of the reactor (F^o), that is $F^i=F^o=[G_0]\cdot k_e\cdot V$, where $[G_0]$ is the steady state concentration of the reactive gas in the reactor. The introduction of an active surface into the LPR contributes to the disappearance of the reactant molecule through heterogeneous interaction and therefore constitutes the sink term which we seek to quantify. It is this additional decrease in the partial pressure of the reactant molecule that carries the desired kinetic information. The simplest analysis of uptake experiments can be achieved by defining a first order adsorption rate constant $k_{uni} = \dfrac{I_0 - I}{I} k_e$

(s^{-1}) , where I_0 and I are mass spectrometric intensities of the reactive gas in the absence and presence of the active surface, respectively (for further details see Golden et al. [2]). This kinetic result can be cast in the form of a dimensionless constant $\gamma = \dfrac{k_{uni}}{\omega}$ which is independent of the surface to volume ratio A_s/V of the system. This uptake coefficient then describes the probability of uptake by the surface using the sample collision frequency as an internal clock for the heterogeneous interaction. In particular, this coefficient describes the net uptake corresponding to the difference between adsorption and desorption rate. The range of uptake coefficients that are accessible to measurement using a Knudsen cell lies in the range $10^{-6} \leq \gamma \leq 1.0$. This large dynamic range in the measurement of γ is made possible by changing A_h by two orders of magnitude.

In practice, however, it turns out that the rate law of many reactions does not correspond to a first order process. In particular, this is the case when (1) the uppermost layer of the sample is altered by the incident molecules or (2) the rate law for adsorption shows a pressure dependence. While the first case results generally in an increase of I as a function of time, the second case may be verified by either significantly changing the flow rate into the reactor (i.e. by an order of magnitude), or by changing the size of the escape orifice thus leading to a different pressure in the reactor. If one of these two operations, that is changing the flowrate or the size of the escape aperture, affects the algebraic value of k_{uni}, we know that the rate law for adsorption is different from first order.

Above we defined the net uptake coefficient γ corresponding to the difference between adsorption and desorption rate. So far, no technique has been developed which allows to distinguish between the rate of adsorption (described by the mass accommodation coefficient) and the rate of desorption of the molecules leaving the surface after a certain residence time. However, the present work has been performed using a new approach of measuring the uptake kinetics in real time. Based on the Knudsen cell, this approach involves pulsed admission of molecules interacting with easily saturable surfaces such as soot and ices. A known number of gas molecules are admitted across a pulsed solenoid valve into the reactor and interact with the active surface. The decay of the gas burst is followed in real time using mass spectrometry. In the case of heterogeneous interaction with the sample, the residence time of the molecules in the reactor will be reduced with respect to the non reactive case (reference experiment), and the decay of the time-dependent MS signal $S(t)$ will be faster according to the relation:

$$S(t) = S_0 \cdot exp\{ -(k_e + k_{eff}) \cdot t \} , \qquad\qquad (1)$$

where S_0 corresponds to the initial amplitude and k_{eff} is the effective rate constant of adsorption. In the case where the rate of adsorption is faster by an order of magnitude than the rate of desorption, k_{eff} is a good approximation of the accommodation coefficient. Moreover, this approach has the advantage over the traditional steady-state technique that it avoids surface saturation and contamination phenomena. In fact, injecting a dose corresponding to about 1% of a formal monolayer may be considered a "weak" surface probe which does not alter the surface within the detection limit.

As in the steady state experiments, k_e in such pulsed valve experiments should be comparable to the kinetic parameter that we wish to measure, for example k_{eff}. In fact, if the rate of effusion and rate of adsorption are competing,

it can be shown that the initial amplitude S_0 is linearly dependent on k_e, that is, the larger k_e, the higher the initial amplitude S_0. In fact, the MS signal intensity S_0 is proportional to $F^0 = [G_i] \cdot k_e \cdot V$, where $[G_i]$ is the instantaneous density after admission of the gas pulse. Therefore, the signal to noise ratio is best for the largest orifice available which is particularly important in the case of a fast reaction ($k_{eff} \geq 10s^{-1}$).

2.2 The Setup for Detection based on Laser Induced Fluorescence

In order to unambiguously determine the reactants and products in the system NO_2 on carbon, three optical ports attached to the LPR provided for *in situ* real-time laser-based gas phase detection. Laser-based diagnostics were used to probe the density, that is the concentration [G], of both the reactant NO_2 and product NO inside the LPR. A Nd:YAG pumped dye laser system (Spectra-Physics GCR 4-10 (seeded), PDL-3) was used in conjunction with either crystal mixing modules (WEX-2) or a Raman shifter to provide light of suitable wavelength for LIF detection of both NO_2 and NO. The tunable output of the laser system is focused via L1 (f.l.=400 mm,) through the optical attachment of the LPR. The fluorescence signal of either NO or NO_2 was collected at 90° to the laser propagation vector and, using a variety of transfer optics, spatial filters including either a bandpass filter or 0.25 m monochromator (Jobin-Yvon HR-250), imaged onto a 1P28 photomultiplier tube. The photoelectric signal of the PMT was then measured using a gated integrator, digitized and stored on computer disk for subsequent analysis.

2.3 The Low Temperature Support used for Ice Surfaces

Figure 2.3 shows a schematic drawing of the low temperature support (LTS). The main part of the LTS is a cylindrical copper core whose top forms the sample dish (37mm diameter). This dish is brazed onto 3/10 mm thick steel walls of 15 mm height in order to minimize the heat conductance so as to keep the temperature gradient to a maximum. Two type K thermocouples are screwed under the sample dish, one in the center and one at the edge. The stem underneath is wrapped with resistance heating wire (12 Ohm, Philips) in order to counterheat the sample dish. The bottom part of the copper core is immersed into a stainless steel Dewar which can be filled with liquid nitrogen (inlet, outlet). This device is placed into a steel vessel serving as a vacuum jacket for thermal insulation. The outer dimensions of the whole vessel are 18 cm in height and 6.5 cm in diameter.

The temperature regulation of the LTS was performed by an Eurotherm (900 EPC Series) controller. It actuated alternatively a heating or cooling loop. Whereas the heating wire was connected to a 220/24 VAC transformer by an intermediate thyristor, the cooling loop consisted of compressed air which was controlled by a magnetic solenoid valve. This circuit exchanged heat by means of

a copper tubing spiral immersed into a Dewar filled with liquid nitrogen in which the compressed air was condensed to a liquid. In order to avoid back streaming and subsequent condensation of ambient water in the spiral, the solenoid valve was by-passed ensuring a minimum flow of pressurized "dry" air.

The of the LTS afforded temperature control within 0.5 K down to 135 K. The maximum temperature gradient across the sample dish corresponding to the difference between center and edge thermocouple readings was 3±1 K at 135K and gradually decreased with increasing temperature. The accurate absolute temperature for an experiment was obtained from measurements of the H2O vapor pressure as a function of temperature given in the literature [3], [4].
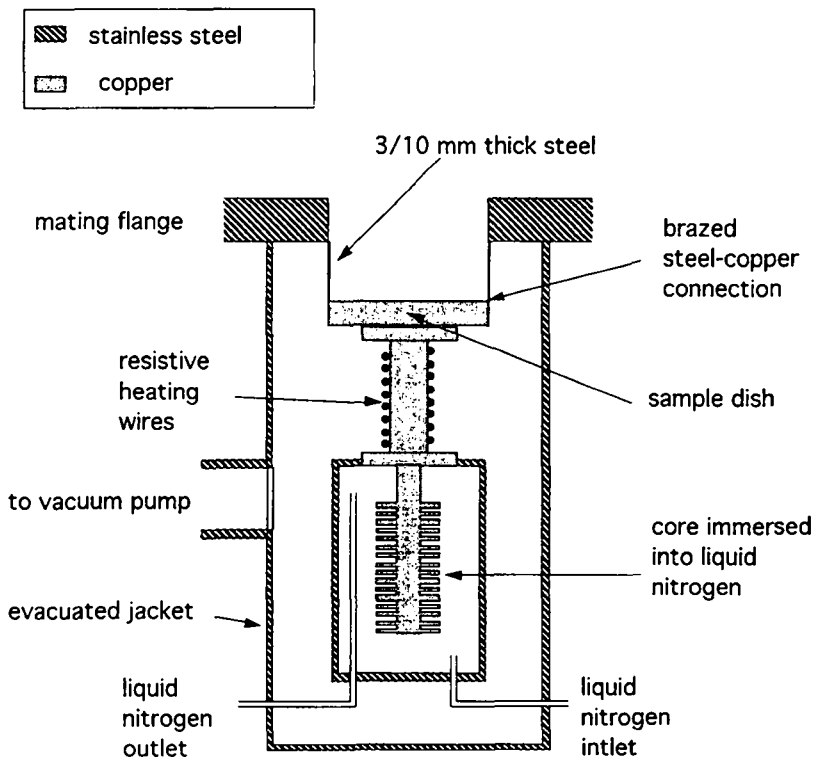
Figure 2.3: Schematic drawing of the low temperature support (LTS). A copper core is immersed into a Dewar containing liquid nitrogen. Resistive counter heating allows temperature regulation within ±1K. A 3/10mm steel wall allows for thermal insulation.

2.4 Simulation of Transient MS-Signals by Lock-in Detection

In our experimental setup we use the lock-in amplifier in order to discriminate the molecular beam effusing out of the Knudsen reactor from the background present in the mass spectrometer (MS) chamber. Especially in experiments in which a pulse of water molecules is superimposed on a continuous signal level due to the evaporation of water from the ice surface, the background pressure may be significant. In order to obtain a high quality signal due to the exponential decay of the MS-signal in the aftermath of a pulse, it is necessary to use the lock-in amplifier. As a consequence it is necessary to determine up to which frequency of decay of an exponentially decaying pulse the used instrument (SRS 850 lock-in) is able to follow the modulated MS signal correctly in order to reliably recover the amplitude decaying as a function of time. In the present case the molecular beam is modulated at approximately 150 Hz.
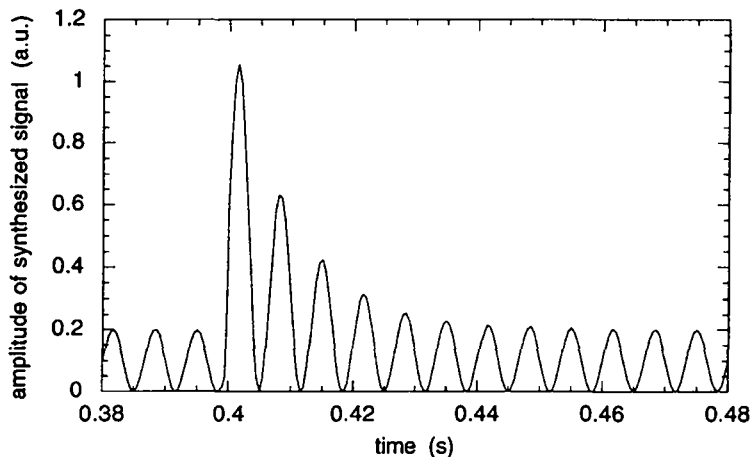
Figure 2.4: Typical synthesized function without noise, given by $f(t) = \{1+\sin(150 \cdot t)\} \cdot \{A_1+A_2 \cdot \exp(k_{dec} \cdot [t-t_0]\}$, where $A_1=0.2$, $A_2=1.0$, $t_0=0.4s$ and $k_{dec}=k_{eff}+k_e=100s^{-1}$. The amplitudes correspond to relative units, and the absolute voltage as well as the DC-offset are defined on the function generator.

In this work we present experiments in which a synthesized analog signal was processed by the lock-in amplifier in the same way as a raw MS signal normally would be. In practice, a digital function representing the raw MS signal was

created on a PC using software developed by Oppliger [5]. By analogy to the chopped molecular beam, this digital function is modulated at 150Hz and corresponds to the following type:

$$f(t) = \{1+\sin(150 \cdot t)\} \cdot \{A_1 + A_2 \cdot \exp(k_{dec} \cdot [t-t_0]\} + A_3 \cdot \{noise\} , \qquad (2)$$

where A_i are different amplitudes and t_0 is the delay of the pulse. The term {noise} is a function taking random values in the interval [-1,+1]. A typical digital function without noise is presented in **Figure 2.4**. The synthesized function composed of 16000 points corresponding to a total length of 1s was then read into a function generator (Stanford Research Systems (SRS) DS345) by means of the transfer program AWC supplied by SRS. Using the function generator an analog signal corresponding to the digital function was then transferred to the lock-in amplifier. The total amplitude A_1+A_2 of this analog signal and its dc-offset were chosen on the function generator, while the internal reference of the lock-in amplifier was set to a modulation of 150Hz.
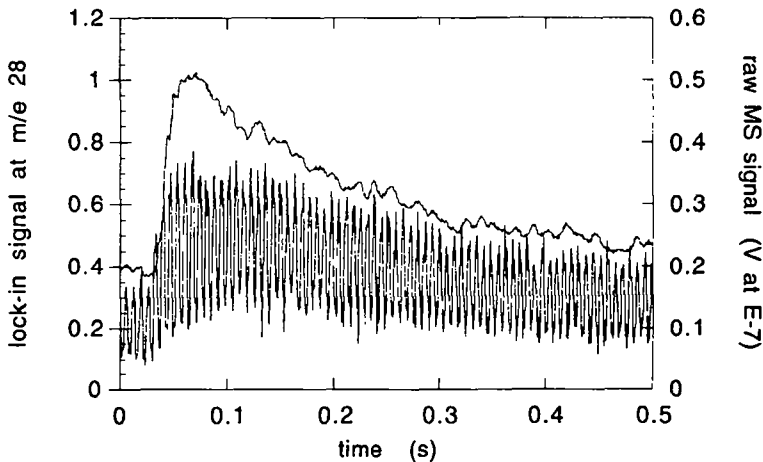
Figure 2.5: Lock-in amplified signal (left hand ordinate, upper trace) and raw MS signal (right hand ordinate, lower trace) of an experiment where a pulse of N_2 was superimposed to a steady state flow of N_2.

We were able to show that the amount of dc-offset chosen on the function generator does not influence the response as long as the lock-in input signal does not exceed 1.4 Volts as specified by SRS. The total amplitude A_1+A_2 set on the

function generator was linearly proportional to its response amplitude on the lock-in amplifier, as expected.

In a first stage, ideal signals such as displayed in **Figure 2.4**, i.e. without the {noise} term, were processed by the lock-in amplifier. These signals could easily be reproduced up to $k_{dec}=150\pm10s^{-1}$. This surprising result can only be explained by assuming exact backtransformation/digital deconvolution of the modulated 150Hz signal. This ideal situation, however, is rarely encountered in practice.

In the second stage, signals composed of a function with the {noise} term were processed by the lock-in amplifier. In order to estimate the amplitude of this {noise} term, raw MS data were acquired and their noise level determined. **Figure 2.5** shows both the raw and the lock-in amplified signal of an experiment where a pulse of N_2 was superimposed to a steady state flow of N_2. Clearly the MS-signal (lower trace) is modulated at 150Hz. Moreover, the signal amplitude not only increases during the light periods due to the higher intensity of the chopped molecular beam, but also during the dark periods due to the increase in background pressure originating from the injected burst of molecules. The
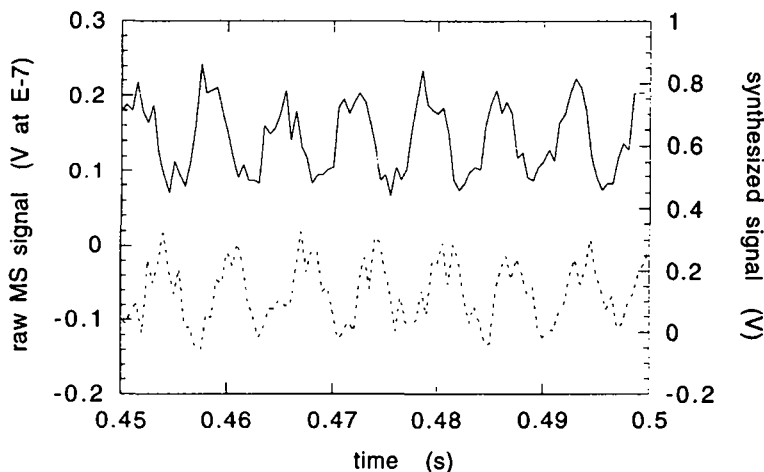
Figure 2.6: Comparison of the raw MS-signal (solid line, left hand ordinate) and the synthesized function (dashed line, right hand ordinate) with $A_3=0.15$ before processing by the lock-in amplifier. At a time resolution of 0.5ms A_3 has been adjusted in order to result in an equivalent signal to noise ratio for both cases.

ratio of the chosen pulse amplitude A_2 to the amplitude A_1 representing the signal at steady state is approximately 2/1 while the decay constant corresponds to $k_e = 5.6s^{-1}$.

Figure 2.6 presents a comparison of a raw MS-signal and the synthesized function of $A_3 = 0.15$ before processing by the lock-in amplifier. Comparing the modulation depth (difference in signal amplitude at dark and light periods) to the variation of the signal amplitude during light periods for the raw MS signal, we find a signal to noise ratio of approximately 3/1. The signal to noise ratio for the synthesized function is given by A_1/A_3 and equals 4/3. At a time resolution of 2000Hz or 0.5ms we clearly see that the signal to noise ratio is similar in both cases which proves that the signals are equivalent and confirms our choice of the amplitude of the noise A_3.
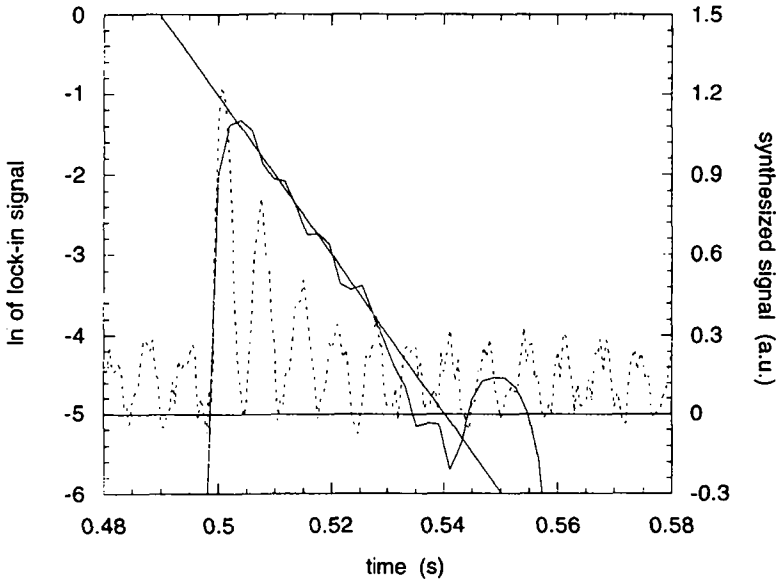
Figure 2.7: Synthesized pulse (dashed line, right hand ordinate) of $k_{dec} = 100s^{-1}$, $A_1 = 0.2V$, $A_2 = 1.0V$ and $A_3 = 0.15V$, and response after processing by the lock-in amplifier (solid line, left hand ordinate).

Figure 2.7 displays a synthesized pulse characterized by $k_{dec} = 100s^1$ (right hand ordinate) as well as the response after processing by the lock-in amplifier (left hand ordinate, logarithmic scale). While the total amplitude $A_1 + A_2$ is set on the function generator to be 1.2V, the ratio of pulse amplitude to steady state

flow A_2/A_1 corresponds to 5/1. The signal to noise ratio was chosen as 4/3
corresponding to the amplitude of the steady state flow and the noise of $A_1=0.2V$
and $A_3=0.15V$, respectively. Clearly, we see that the decay is single exponential
corresponding to $k_{dec}=100\pm10s^{-1}$. We therefore conclude that the lock-in
amplifier is able to record an exponential decay given by $k_{dec}=100s^{-1}$ within an
uncertainty of $\pm10\%$ following a signal having a realistic signal to noise ratio. We
have shown that the synthesized function given by $A_1=0.2$, $A_2=1.0$ and $A_3=1.5$ in
equation 2 with a corresponding ratio of $A_2/A_3=2/3$ yields a value of k_{dec} lying
between 96 and $130s^{-1}$. This means that an amplitude of A_3 which is larger than
A_2 yields values of k_{dec} within a 20% error. Consequently, the response of the
lock-in amplifier is rather sensitive to the ratio of A_3/A_1 or A_3/A_2 than to the one
of A_2/A_1.

2.5 Generalisation of the Experimental Rate Constants

The following paragraph deals with the problem of expressing the rate constants
in terms of transferable quantities independent of the surface-to-volume ratio of
the system used for their determination. We will therefore distinguish between
"system" parameters for which the rate of chemical transformation is expressed
in #s^{-1} and transferable parameters which are independent of the experimental
apparatus. The first ones correspond to ones used in our model calculation,
where "system" means our experimental apparatus, while the latter ones
correspond to unit surface-to-volume ratio. The symbol # is dimensionless and
corresponds to "number". We use the technique of dimensional analysis to
convert the system to transferable rate constants.

For demonstration purposes we will start with a purely homogeneous
albeit simple kinetic system as follows:

$$NO_2 + NO_3 \rightarrow N_2O_5 \qquad (k^{II}) \qquad\qquad (3)$$

The governing rate equation describing the rate of change for NO_2 in our
Knudsen cell reactor is given by equation (4) in which the reaction rate is

expressed in # s^{-1}. In our system units we define N_{NO2} as being the total number of NO2 molecules in the volume V, that is $N_{NO2} = (NO_2) \cdot V$. The symbol in round brackets corresponds to the number density (# cm^{-3}).

$$dN_{NO2}/dt = F^i_{NO2} - k_e \cdot N_{NO2} - k^{II} \cdot N_{NO2} \cdot N_{NO3} \qquad (4)$$

In order to obtain the dimension # s^{-1} for the rate (left hand side of equation 4), k^{II} must have the dimension #$^{-1}$ s^{-1}. In transferable units the rate equation is given by equation (5) with the rate expressed in # cm^{-3}s^{-1}:

$$d(NO_2)/dt = F^i_{NO2}/V - k_e \cdot (NO_2) - \tilde{k}^{II} \cdot (NO_2) \cdot (NO_3) \qquad (5)$$

In order to yield the dimension # cm^{-3}s^{-1} for the rate (left hand side of equation 5), $\tilde{k}^{II}$ must have the familiar dimension for a bimolecular reaction, namely #$^{-1}$ cm^{3}s^{-1}, where tilde refers to a transferable rate constant. Therefore, to convert k^{II} from system units to transferable units we have to multiply the system rate constant by the volume V of the reaction system. The unimolecular rate constant k_e still has the dimension s^{-1}.

Now we turn to the case of a combined homogeneous and heterogeneous reaction system which is the case of interest in the present work. As an example we will take a simple Langmuir-Hinshelwood adsorption reaction taking place in our Knudsen cell, with {S} being the number of free adsorption sites, the brackets meaning that it is a surface species:

$$NO_2 + \{S\} <=> \{NO_2 \bullet S\} \qquad (k_{ads}, k_{des}) \qquad (6)$$

The pertinent rate equation in system units with the rate expressed again in # s^{-1} is given in equation (7):

$$dN_{NO2}/dt = F^i_{NO2} - k_e \cdot N_{NO2} - k_{ads} \cdot N_{NO2} \cdot S_{tot} + k_{des} \cdot N_{NO2 \bullet S_{tot}} \qquad (7)$$

In this equation S_{tot} corresponds to the total number of free adsorption sites available on the active surface. It can be calculated as the specific number of surface sites per sample area (S) in units of # cm^{-2} multiplied by the geometric area of the active surface. The same holds for the occupied (covered) surface sites $N_{NO2 \bullet S_{tot}}$. The dimension of the rate constants k_{ads} and k_{des} in this unit system are #$^{-1}$s^{-1} and s^{-1}, respectively, because each term in equation (7) must have the

dimension # s^{-1}. The governing rate equation for NO_2 in transferable units is given in equation (8):

$$d(NO_2)/dt = F^i_{NO_2}/V - k_e \cdot (NO_2) - \tilde{k}_{ads} \cdot (NO_2) \cdot (S) + \tilde{k}_{des} \cdot (NO_2 \bullet S) \quad (8)$$

The symbols (S) and ($NO_2 \bullet S$) correspond to the specific number of respective surface sites on a per cm^2 basis. The dimension for $\tilde{k}_{ads}$ in the transferable units is $\#^{-1}cm^2s^{-1}$ and that for $\tilde{k}_{des}$ is $cm^{-1}s^{-1}$ because each term in equation (8) must have the dimension $\# s^{-1}cm^{-3}$. We now arrive at the important conclusion that *we have to multiply the system rate constants for adsorption,* k_{ads}, *by the geometric area of the sample surface in order to arrive at a transferable rate constant. The rate constant* k_{des} *has to be multiplied by the surface to volume ratio of the experimental system in question to arrive at* $\tilde{k}_{des}$ *in transferable units.*

2.6 References

[1] Fenter, F.F.; Caloz, F.; Tabor, K.; Gutzwiller, L.S. and Rossi, M.J., in preparation.

[2] Golden, D.M., Spokes, G.N. and Benson, S.W., Angew. Chem. 1973, 14, 602.

[3] Jancso, G.; Pupezin, J.; Van Hook, W.A. J. Chem. Phys. 1970, 74,2984.

[4] Marti, J.; Mauersberger, K. Geophys. Res. Lett. 1993,20, 363.

[5] Oppliger, R., unpublished results.

Chapter Three - Heterogeneous Kinetics of NO2 on Amorphous Carbon at Ambient Temperature

3.1 Introduction

The interaction of NO_x with solid carbon particulate, two pollutants of major importance, is expected to play a significant role in the atmosphere due to the simultaneous occurrence of both components on a global scale, even in remote regions [1], [2]. In fact, typical concentrations of NO_2 and NO range from 1 to 500 ppb and 0.05 to 2'000 ppb, respectively, while the emission of elemental carbon of a diesel engine has been measured to be 2.8 to 3.4 g per kg fuel [3]. A dominant fraction of both pollutants, NO_x and carbonaceous aerosols, is of anthropogenic origin and stems from oxidation of carbon containing fuels, for instance in internal combustion engines [4]. The carbonaceous aerosol is often called soot and consists of an organic fraction such as polycyclic aromatic hydrocarbons which are adsorbed to an insoluble fraction which contains elemental carbon that will henceforth be called amorphous carbon. From a chemical point of view, the plume of a combustion source, stationary or mobile, could potentially be a very reactive medium for heterogeneous processes as water vapor, NO_x, unburnt hydrocarbons, carbonaceous aerosol particles and a number of oxidizing species in small concentrations such as O atoms, OH and HO2 free radicals are emitted into the atmosphere. Naturally, this plume chemistry operates at higher densities than its low density analog occurring on a global scale. We therefore are looking for a unifying mechanism describing both the high and low density aspects of these heterogeneous processes in order to understand and thus predict the chemical fate of these pollutants under different emission scenarios.

The majority of NO_x originating from engine combustion is emitted as NO. However, depending on the mode of operation and the kind of internal combustion engine, up to 30% of NO_x can be emitted as NO_2 [5]. Increased emission of NO_2 can be expected from idling spark-ignited engines as well as from Diesel engines under low load conditions [6], [7]. In the middle atmosphere the occurrence of carbonaceous aerosols is also due to combustion processes linked to civil air transport, both subsonic as well as (projected) supersonic [8]. We expect *a priori* a similar emission spectrum from a jet engine under operating conditions compared to a stationary or mobile internal combustion engine on the earth's surface even though little quantitative work on jet engine emission has been undertaken so far. Even though this black carbon aerosol constitutes only a minor fraction of the total aerosol mass in the upper troposphere and lower

stratosphere (~1%), it may be important for the absorption of light and affect the radiative transfer in the atmosphere and thus the climate due to its uniquely high absorption cross section of 10 m^2/g across the visible spectral range [9]. Quite recently, the optical absorption properties of amorphous carbon have come under renewed scrutiny and have resulted in a finer picture that allows aging and chemical transformation of the black carbon aerosol to be assessed and helps to pinpoint its likely origin [10]. Recently, the NO_x emission in the plume of a subsonic aircraft has been measured [11], and various NO_x emission scenarios from a projected fleet of supersonic air transport could be pointing to the potential importance of the NO_x-amorphous carbon interaction with respect to ozone depletion in the lower stratosphere on both the local as well as the global scale [12].

Of the three lower nitrogen oxides, nitrous oxide (N_2O), nitric oxide (NO) and nitrogen dioxide (NO_2), only the latter reacts with amorphous carbon in a significant way. Smith and coworkers have studied the NO_2-amorphous carbon interaction at higher pressure with respect to the surface adsorbates which they studied using transmission FTIR [13]. One of the conclusions of their work was that only 1% or so of the NO_2 disappearing from the gas phase is observable by FTIR absorption spectroscopy as C-NO_2 or C-ONO functionalities [14]. A fairly complex dual site mechanism was proposed in which both NO_2 as well as N_2O_4 adsorbed on amorphous carbon at pressures from 5 to 120 Torr. No gas phase products resulting from the interaction of NO_2 with amorphous carbon were detected.

One scenario of the NO_2 chemical reactivity on amorphous carbon would be that it reacts on carbon particulate with adsorbed H_2O akin to its well known reactivity in liquid water or on moist Teflon™ surfaces according to reaction (1) [15], [16] even though this reaction is known to be slow [17]

$$2NO_2 + H_2O \rightarrow HONO + HONO_2 \tag{1}$$
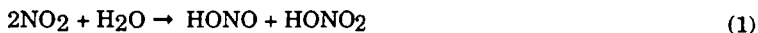
In this case the carbon particulate just provides the support for the heterogeneous chemical interaction without partaking itself in the chemistry. Another scenario would involve oxidation/reduction chemistry with the carbon being oxidized ultimately to CO and CO_2 under simultaneous reduction of NO_2 to some lower oxidation state of nitrogen such as NO according to reaction (2):

$$NO_2 + C_{am} \rightarrow NO + \{C\bullet O\} . \tag{2}$$
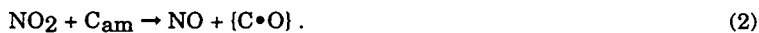
C_{am} is amorphous carbon and $\{C \bullet O\}$ is an oxidized yet non-volatile carbon species in its precursor form which will release CO and CO_2 when heated.

In this work we focus on a chemical kinetic study of NO_2 interacting heterogeneously with three well characterized albeit distinctly different amorphous carbon samples that serve as model substrates for atmospheric carbon particulate. Even though the kinetic study does not address chemical reactions on carbonaceous aerosol surfaces *per se*, the chemical properties of the model substrate are supposed to be similar to the amorphous carbon fraction of atmospheric carbonaceous aerosol right after emission by virtue of the manufacturing process through incomplete combustion of gaseous or liquid fuels under conditions where the organic fraction is held to a minimum. The goal of the present study is the understanding of the kinetics and the identification of the products at ambient temperature and low pressure in terms of *elementary chemical reactions* and the comparison of the chemical behavior between the three different albeit well characterized types of amorphous carbon on model substrates under controlled laboratory conditions.

3.2 Knudsen Cell Parameters and Sample Preparation

A 3.7 cm inside diameter Pyrex cup was used to contain the bulk solid samples. Typically 50 to 500 mg of any of three different amorphous carbon samples purchased from DEGUSSA were used for a given experimental run [18]. The specific samples were chosen to cover a wide range of internal surface: sample 1 was FW2™ with a BET surface of 460 m^2/g, sample 2 was Printex 60™ with 115 m^2/g and sample 3 was Lamp Black FS101™ with 20 m^2/g. Reference experiments were conducted using fumed silica Aerosil 130™ with a BET surface of 130 m^2/g. The carbon samples were used as provided by the manufacturer by dispersing them evenly over the surface of the Pyrex dish. The purity of NO_2 was ascertained before each experiment by addition of O_2 to a total pressure of about 150 to 300 Torr (approximately 1% NO_2 by volume) and subsequently purified by several freeze-pump-thaw cycles in darkness at liquid nitrogen temperature.

The rate of effusion out of the escape orifice is used as the internal clock with which the rate of the heterogeneous chemical processes are measured. **Table 3.1** presents the calibrated escape rate constants for the LPR shown in **Figure 2.2** (preceding chapter) expressed as $k_e = C_e \cdot (T/M)^{1/2}$ s^{-1}, where T is the temperature in Kelvin and M is the molar mass in grams. The two pairs of values for C_e correspond to the reference chamber volume (isolation plunger

closed) and total volume (reference + sample chamber volumes), respectively. The measurement of C_e was performed by observing the rate of change of the MS signal for the sampled effusive molecular beam with time after either pulsed valve addition of a gas or interruption of a continuous gas flow into the LPR. Various stable gases such as He, Ar, N_2 and CO_2 were used for this purpose as well as NO and NO_2. Within the experimental uncertainty values of C_e obtained in this way were in good agreement.

Table 3.1: Characteristic Parameters of the Low Pressure Reactor (LPR)

	reference chamber	reference + sample chamber
C_e^S a)	0.033	0.023
C_e^L a)	0.51	0.35
Volume (cm^3)	535	750

a) C_e^i: mass reduced escape rate coefficient for Knudsen cell $\left(k_e^i = C_e^i \sqrt{\dfrac{T}{M}} \; (s^{-1}) \right)$,

where i=L, S correspond to large and small escape aperture, respectively.

The result of a typical experimental sequence is presented in **Figure 3.1** in which exposure of a carbon sample (100 mg of FW2, sample 1) to a metered flow of NO_2 (1.3×10^{15} molecule s^{-1}) is monitored using the MS signals at m/e 46 and 30. At time t<0, the steady state non-reactive flow of NO_2 into the reference chamber is established. During this period, only masses corresponding to the parent NO_2^+ and daughter NO^+ are observed with no contribution to m/e 30 arising from neutral gas phase NO (trace marked with triangles). Upon opening of the sample chamber to the gas flow at t=0, a prompt decrease in the m/e 46 signal (trace with squares) and a corresponding increase in the m/e 30 signal (trace with circles) is observed reflecting the uptake (trace with squares) and conversion to NO (trace with circles) of the NO_2 on the carbon sample. The lower curve (trace with triangles) with the same shape as the one corresponding to m/e 30 (trace with circles) is a MS signal at m/e 30 corrected for the contribution of NO_2 to its fragment peak at m/e 30 and is proportional to the flux of product NO leaving the LPR Ensuing saturation of the carbon follows until at time t≈230 s the sample chamber is isolated from the gas flow and non-reactive steady state flow of the NO_2 is once again reestablished. At time t≈250 s, the NO_2 flow is stopped until all signals drop to zero intensity. Finally at t≈285 s, the sample chamber is once again opened and the residual trapped gas is allowed to escape from the LPR.
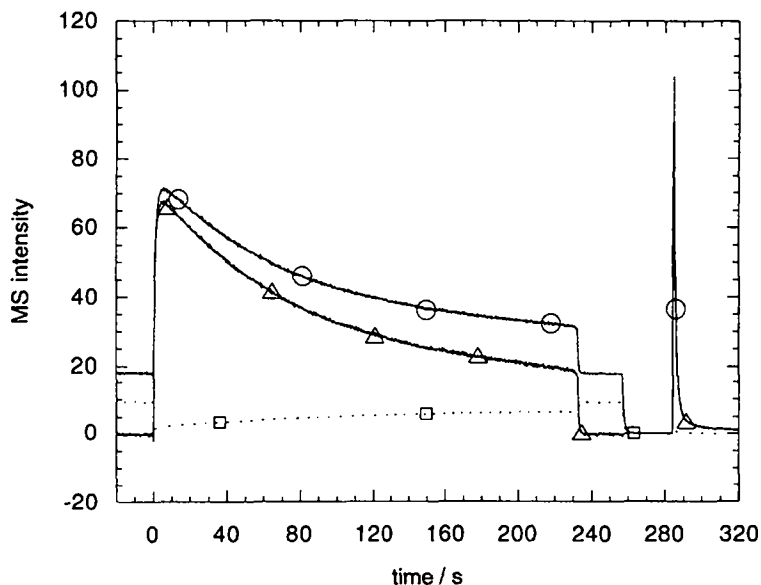
Figure 3.1: Measurement protocol using large orifice (3mm i.d.). Example showing results from experimental run of NO_2 (flow rate: $1.3 \cdot 10^{15}$#/s) with FW2 amorphous carbon. Traces with open circles and squares correspond to raw MS data. The trace with open triangles is from the signal at m/e30 corrected for the NO_2 contribution at m/e30.

An important albeit subtle transient effect at short reaction times is shown in **Figure 3.2 a** using the unreactive case of Ar exposed to a carbon sample in comparison to NO_2 exposure (reactive case, **Figure 3.1**). At time t=0 s a constant flow rate of Ar is exposed to the sample in the small aperture LPR upon which a transient drop in MS signal at m/e 40 is observable. This is due to the fact that a given number of Ar atoms, previously in the volume of the reference chamber, is now distributed over the total LPR volume including the sample chamber after opening the sample compartment. Apparently the Ar flow rate (source term) is not large enough to instantly fill the previously empty volume to the steady state pressure. This volume filling effect, in short called the PV term, must also be present in the reactive case of NO_2 exposure (see **Figure 3.2 b**) and can be corrected for in closed mathematical form only under the assumption of no heterogeneous interaction occurring during relaxation to steady-state conditions. The condition of no chemical interaction during PV relaxation does certainly not hold in the present case of NO_2 interacting with carbon because the time scales for PV relaxation and heterogeneous uptake are similar. For reasons presented

in the next section we had to resort to numerical modeling of the NO_2 uptake kinetics that naturally included the PV relaxation.
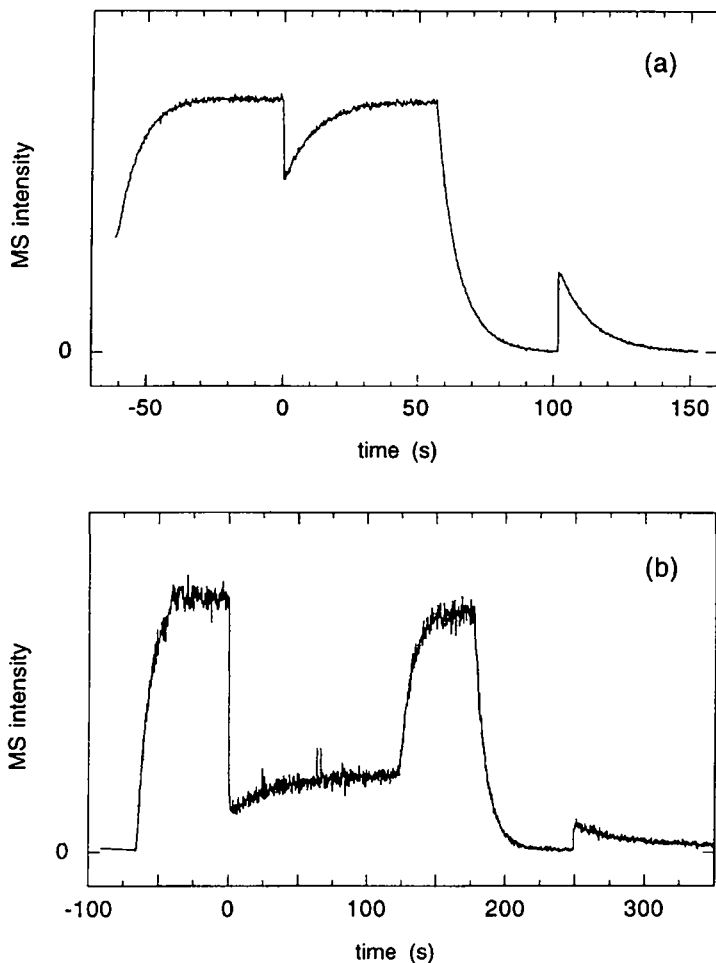
Figure 3.2 a and b: Transient pressure behaviour revealed while using the small orifice (1mm i.d.). Comparison is between (a) non reactive argon and (b) reactive NO_2 exposed to 50mg FW2 amorphous carbon sample. Flowrates: (a) Ar flow rate=$8.0 \cdot 10^{15}$#/s; (b) NO_2 flow rate=$1.5 \cdot 10^{15}$#/s.

3.3 Chemical Kinetic Model

A chemical kinetic modeling program based on coupled differential equations describing the rate of change of each species was developed to (1) simulate the real-time change of the NO_2 flow rate for steady-state and pulsed-valve experiments and (2) resolve the apparent discrepancy between the values of k_{uni} measured for the two different LPR orifices. The simplest analysis of uptake experiments in terms of first order adsorption of NO_2 leads to a first order rate constant k_{uni} (in s^{-1}) for uptake given by equation (3):

$$k_{uni} = k_e \, (I_0 - I)/I \qquad\qquad\qquad (3)$$

where I_0 and I are mass spectrometric intensities of NO_2 at m/e 46 in the absence and presence, respectively, of the amorphous carbon. An important test of the first-order rate law is a constant value for k_{uni} measured in the small and large aperture LPR. In the present case values for k_{uni} obtained using small aperture data are between a factor of three to nine smaller than the ones measured using large aperture data, depending on the experimental conditions. This implies that the mechanism for NO_2 uptake is complex, and that chemical kinetic modeling had to be used in the interpretation of the uptake kinetics.

In anticipation of the next section on experimental results and discussion, we present the detailed chemical kinetic model at this point in order to be able to emphasize the quantitative differences between the three representative amorphous carbon samples. In our experiments and model simulations we emphasize the early stages of the NO_2-amorphous carbon interaction at low dose because of its relevance to atmospheric conditions. The justification for focusing on the shortest possible time scale in our uptake experiments becomes clear when one considers that the collision frequency, ω, of an ambient NO_2 molecule with the surface of a carbon particle is on the order of 1 s^{-1} for a polluted atmosphere [19]. In comparison, ω for the active surface within our reactor is 136 s^{-1} at ambient temperature. This means that an average NO_2 undergoes as many collisions in approximately 10 ms inside our Knudsen cell as an ambient NO_2 under atmospheric conditions in one second. While clearly the most appropriate conditions for approximating the real atmosphere are limited to the large orifice LPR at low flow rates of NO_2, results using the small orifice LPR and higher flow rates thus leading to higher pressures provide additional information necessary to probe the details of the chemical mechanism. From the following comparison of the experimental results with the model it will become obvious that this simple mechanism fits the main features of NO_2 uptake and

NO production fairly well at early reaction times covering the first few hundred NO_2-carbon collisions which is the time domain of interest in the present work.

In view of the emphasis on the low dose behavior of amorphous carbon the following set of chemical kinetic equations constituted the reaction mechanism, where the surface-bound species are put in brackets {} and the gas phase species are left unlabeled:

$$NO_2 + \{S\} \quad \underset{k_{-1}}{\overset{k_1}{\rightleftharpoons}} \quad \{NO_2 \bullet S\}_p \tag{4}$$

$$NO_2 + \{S\} \quad \underset{k_{-2}}{\overset{k_2}{\rightleftharpoons}} \quad \{L\} \tag{5}$$

$$\{NO_2 \bullet S\}_p \quad \overset{k_3}{\longrightarrow} \quad \{NO_2 I\} + \{S\} \tag{6}$$

$$\{NO_2 \bullet I\} \quad \overset{k_4}{\longrightarrow} \quad \{NO_2 R\} \tag{7}$$

$$\{NO_2 \bullet I\} \quad \overset{k_5}{\longrightarrow} \quad NO + \{C \bullet O\} \tag{8}$$
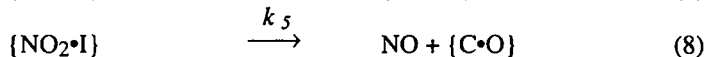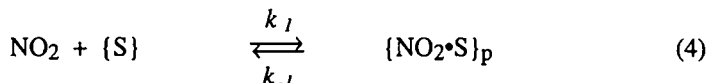
It is important to realize that the model description of processes taking place simultaneously in the gas phase as well as on surfaces of a given experimental system are in terms of global rates for the system under study. This means that the model keeps track of the rate of conversion throughout the total volume of the LPR, and not on a per cm^3 basis as is the case for the description of purely homogeneous kinetics. Similarly, the rate of conversion for a heterogeneous process applies to the total surface area in the system on which the process is taking place, thus automatically taking into account the surface-to-volume ratio of the given experimental system.

Equations (4) and (5) describe the elementary adsorption steps of NO_2 onto a formally unoccupied adsorption site {S}, the only sites accessible to the gas [20]. The initial adsorption may form either a weakly bound "physisorbed" and reactive species {$NO_2 \bullet S$}$_p$ going on to reaction products, or a non-reactive species {L}. As will be shown later, this competition for surface sites {S} or branching turns out to be crucial for the interpretation of the pressure and residence time dependence of the NO_2 uptake. Due to the fact that the number of adsorption sites is finite in every real heterogeneous reaction system, the adsorption rate will begin to decrease once a fraction of a monolayer coverage is obtained. We assume that the elementary adsorption step of NO_2 follows Langmuir adsorption kinetics and thus a rate law first order in both NO_2 and {S}

for early times where the reverse process, unimolecular desorption, can be neglected. In practice the available data from uptake experiments do not allow the separate determination of k_1, k_2 nor $\{S\}$ so that only the product $(k_1 + k_2) \cdot \{S\}$ can be determined. The separation into k_1, k_2 and $\{S\}$ can be accomplished only through direct probing of the surface species. To the best of our knowledge no such experiments have been performed to date.

Equation (6) describes the conversion of the weakly bound species into an intermediate $\{NO_2 \bullet I\}$. We associate this intermediate species with bonding of NO_2 transferred onto "deeper" sites (not explicitly shown) distributed over the internal surface of the sample. This step effectively frees-up a surface site that is available for further gas phase NO_2 adsorption. The intermediate $\{NO_2 \bullet I\}$ can either be transferred to a "reservoir" state $\{NO_2 \bullet R\}$ (equation (7)) or undergo irreversible reaction to product NO and a solid surface oxide $\{C \bullet O\}$ (equation (8)) [21]. Together, equations (7) and (8) may be viewed as representing surface diffusion processes. Including the branching of $\{NO_2 \bullet I\}$ into the model was necessary because of an often observed imbalance between the rate of NO formation and the rate of NO_2 uptake.

Of course, all the surface species can not be detected in the present experiment which monitors only the disappearance and generation of gas phase species NO_2 and NO. Reactions (4) to (8), nevertheless, represent the minimum number of equations required to model the NO_2 uptake on amorphous carbon within the limits of accuracy of our experimental determination.

2.4 Results and Discussion

2.4.1 Pulsed Valve Experiments

We begin the discussion with the pulsed-valve experiments because they are carried out in the limit of low NO_2 exposure on previously unexposed carbon samples. Using this method, the initial uptake of NO_2 is given solely by the forward processes in equations (4) and (5) at the earliest times of the exposure thus providing the most direct determination of the product $(k_1 + k_2) \cdot \{S\}$ for input into our chemical kinetic model. In order to minimize saturation effects the majority of the pulsed valve experiments were performed in the large aperture reactor ensuring the lowest possible instantaneous pressures in the LPR. Continued pulsed dosing reveals that poisoning becomes apparent after approximately ten pulses affecting the uptake of NO_2 as well as the NO

production. The multiplexed MS signals of both NO_2 and NO could be resolved on the time scale needed to follow subsequent uptake kinetics.

The initial experiment using the pulsed valve addressed the question how the quantity and geometric area of the amorphous carbon related to the observed decay time of NO_2 in the Knudsen cell. The range of the NO_2 dosing (3 to $6 \cdot 10^{14}$ molecules per pulse) corresponded to less than 6% of a monolayer. In order to measure the dose dispensed by the pulsed valve it was actuated once with the sample chamber closed. The area under the MS signal vs. time curve was integrated to yield the total number of NO_2 molecules admitted into the Knudsen cell in one pulse. Subsequently the same experiment was repeated with the sample chamber open. The only assumption referring to the dosage was that the pulsed valve admitted the same number of molecules into the LPR from one pulse to the next, that is in a reproducible manner, which was verified experimentally ($\pm 10\%$ variation). As will be discussed below, the notion "monolayer" of NO_2 on amorphous carbon is used in this context as a calculated, that is estimated, quantity. It provides guidance as to what the actual dose is relative to a closely packed arrangement of NO_2 on the geometrical surface area. This surface area is the projection of the real surface to a (horizontal) plane perpendicular to the macroscopic surface normal and is somewhat similar to the Fuchs surface that is relevant for atmospheric gas-uptake experiments on aerosols.

Figure 3.3 a and **b** display two representative pulsed valve experiments of NO_2 exposed to 500 mg of amorphous carbon sample 1 spread out over 10.8 cm^2, and 25 mg of sample 1 spread out over 2.3 cm^2 at limiting low doses, respectively. The decay rate constant k_{eff} of the NO_2 MS signal is given by equation (9) where the brackets [] denote either the gas phase concentration or the total number of surface species. The decay rate constant scales within experimental error with the exposed surface.

$$k_{eff} = (k_1 + k_2)\{S\} + k_e^L - k_{-1}[\{NO_2 \cdot S\}] / [NO_2] - k_{-2}[\{L\}] / [NO_2] \qquad (9)$$

Due to the fact that we are working with limiting low doses of NO_2 corresponding to 6% surface coverage at most, the rate of its desorption from the weakly bound state $\{NO_2 \cdot S\}_p$ and the surface species $\{L\}$ is negligible. For the current analysis, we have set both terms containing k_{-1} and k_{-2} in equation (9) to zero. However, if the pulsed valve experiments are conducted in the small aperture LPR, this assumption does not hold due primarily to a factor of 15 increase in residence time of NO_2 in the LPR and the concomitant
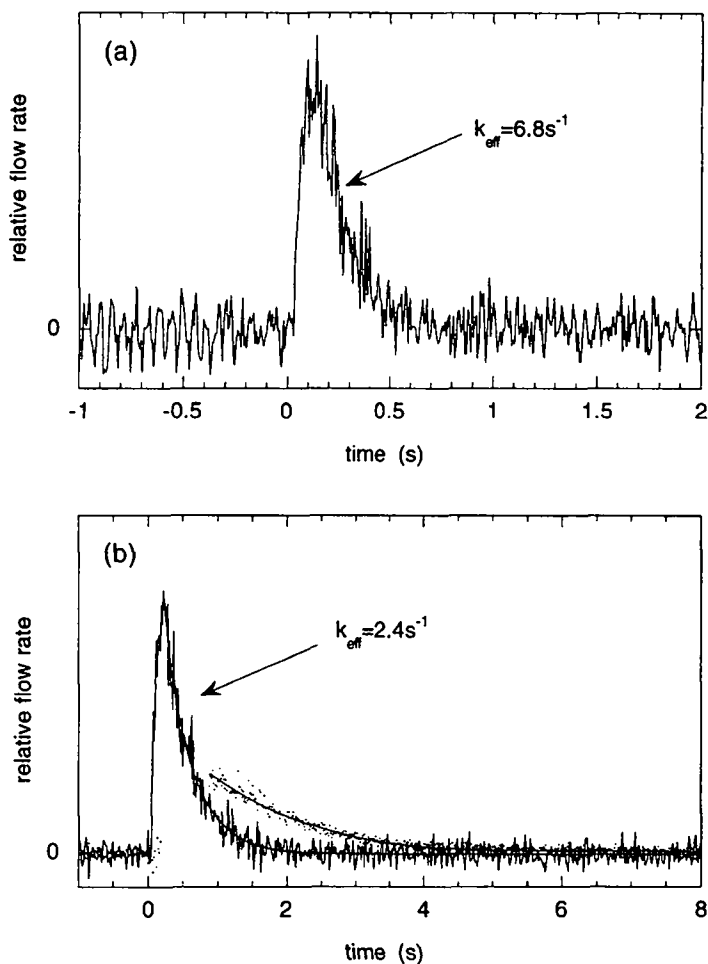
Figure 3.3 a and b: Area dependence of initial NO2 pseudo first order uptake rate constant k_{eff}, using the LPR large orifice (3mm i.d.) and pulsed valve delivery of NO2. (a) NO2 dose=$4.2 \cdot 10^{14}$ molecules on 500mg of FW2 dispersed over 10.8cm^2. (b) NO2 dose=$3.2 \cdot 10^{14}$ molecules on 25mg of FW2 dispersed over 2.3cm^2. Solid line corresponds to NO2, while the released NO is represented by dots.

increase in the gas-surface collision rate. In contrast to the large aperture LPR, the small aperture LPR data do not follow a single exponential decay over comparable time scales. The important result from similar large aperture LPR

data is that the NO_2 uptake scales with the sample geometric surface area and is independent of both the internal surface area and sample mass. A complicating factor is the long rise time of the MS signal (approximately 30 to 50 ms for the present experiments) associated with the non-ideal characteristics of the LPR such as for instance restricted molecular flow. This means that the single exponential decays can be followed only after about 200 ms following pulsed valve actuation. However, given the accuracy of the experimental data and the associated quality of the fits used for determination of the initial uptake rates, we are confident that we are observing the elementary steps of the mechanism responsible for the forward processes in equations (4) and (5).
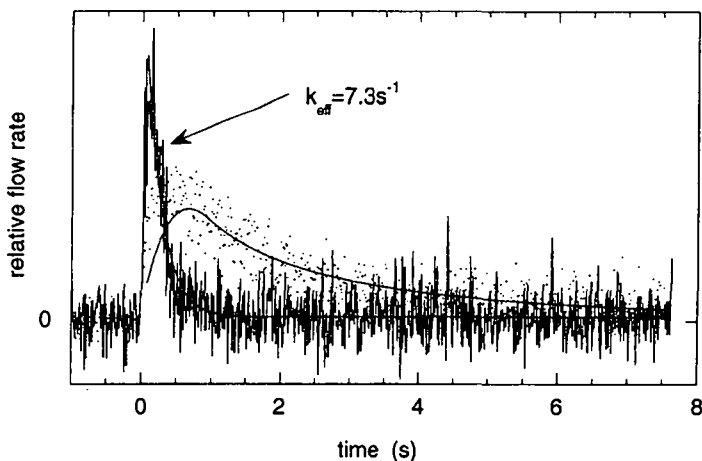
Figure 3.4: Pulsed valve NO_2 uptake (solid line) and NO release (small dots) using the large orifice (3mm i.d.) on a 50mg sample of FW2 used in determination of k_{eff}. NO_2 dose=$2.9 \cdot 10^{14}$ molecules. NO released =$2.9 \cdot 10^{14}$ molecules.

Figure 3.4 presents a pulsed valve experiment in which NO_2 molecules were exposed to 50 mg of sample 1 in the large aperture LPR. The integral under the m/e 46 signal represents $5.8 \cdot 10^{13}$ molecules of surviving NO_2 for a total NO_2 dose of $(2.9 \pm 0.4) \cdot 10^{14}$ molecules. The NO formation (corrected for contributions of NO_2 to m/e 30) is delayed in time with respect to NO_2 adsorption implying physisorbed or some other surface-bound NO_2 intermediate as a NO precursor. The integrated NO contribution to the m/e 30 signal corresponds to $(2.3 \pm 0.3) \cdot 10^{14}$ molecules of NO showing 100% of the mass balance appearing as gas phase product. The effective unimolecular decay rate constant k_{eff} for this example is

7.3 s^{-1} and pertains to a previously unexposed carbon sample. We note that the mass spectrometric detection of the fraction of NO_2 surviving the heterogeneous interaction is difficult when that fraction is small, as the limited signal to noise ratio of the data presented in **Figure 3.4** attest. In this case the surviving fraction is approximately 20% which carries the information about the residence time (k_{eff}) of NO_2 in the presence of the active surface in the sampling beam. This feature of the experimental approach serves to demonstrate the necessity of choosing an appropriate k_e for the system under investigation which should be on the same order of magnitude as the reactive contributions to k_{eff}.

An alternate approach is to monitor the NO_2 *in situ* and in the presence of the active surface inside the LPR, thus measuring the NO_2 residence time directly by observing the decay of the NO_2 density. To this end we have performed Laser Induced Fluorescence (LIF) measurements of both NO_2 and NO *in situ* . Even though the present measurements did not lead to an improvement in the precision of the uptake kinetics due to the limited sampling frequency (10 s^{-1}), they unambiguously identified NO as the major reaction product and justified our experimental procedure of correcting the MS signal at m/e 30 by the NO_2 contribution and interpreting it as NO. The distinction between LIF and MS detection is best demonstrated under steady-state conditions where, upon changing from large to small orifice, *in situ* measurements show an increase in the LIF signal by a factor of $k_e^L/k_e^S=15$ (**Table 3.1**) because it measures the *density*, while the MS signals remain unchanged because they monitor the constant flux across the LPR.

In situ detection of both NO_2 and product NO within the LPR was carried out using LIF following a protocol similar to the experimental time sequence of events described in **Figure 3.1**. The results presented in **Figures 3.5 a** and **b** show the fluorescent emission for NO_2 ($\Sigma <= \Pi$, **Figure 3.5 a**) and product NO ($X <= A$, **Figure 3.5 b**) following laser excitation at 411 nm and 226.9 nm, respectively. As indicated above, the primary purpose of the LIF experiments was to unambiguously prove the identity of NO monitored by mass spectrometry in the bulk of the present work. The experiments were carried out using 56 mg of sample 1 and the small LPR orifice in place. In **Figure 3.5 a** and t< -90 s, the LPR is evacuated with no NO_2 flowing into the cell. At t~ 90 s, the NO_2 flow is turned on until a steady state flow condition for the reference chamber is established. At t=0 s, the evacuated sample chamber containing sample 1 is opened. The prompt drop in the NO_2 signal is followed by a gradual increase until at t~ 50 s the sample chamber is again closed and the non-reactive steady state flow identical to the one for t>-90 s is reestablished. The NO_2 flow is then

Figure 3.5 a: Detection of NO_2 by LIF *in situ* probing using the small orifice (1mm i.d.) and 56mg of FW2. NO_2 flow rate: $(2.6\pm0.4)\cdot10^{14}$ #/s.

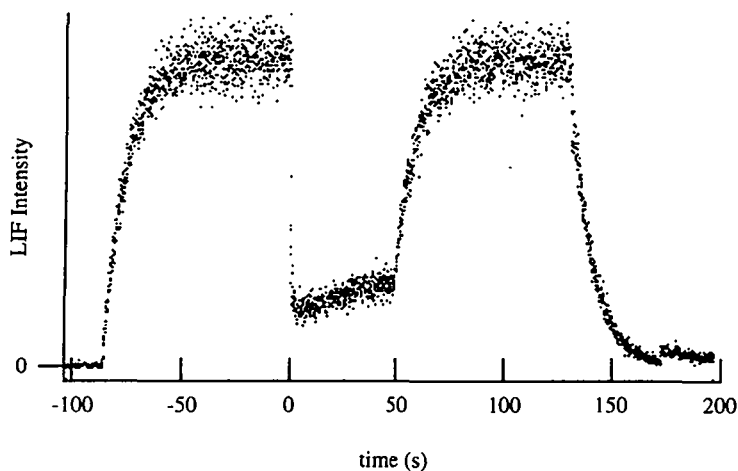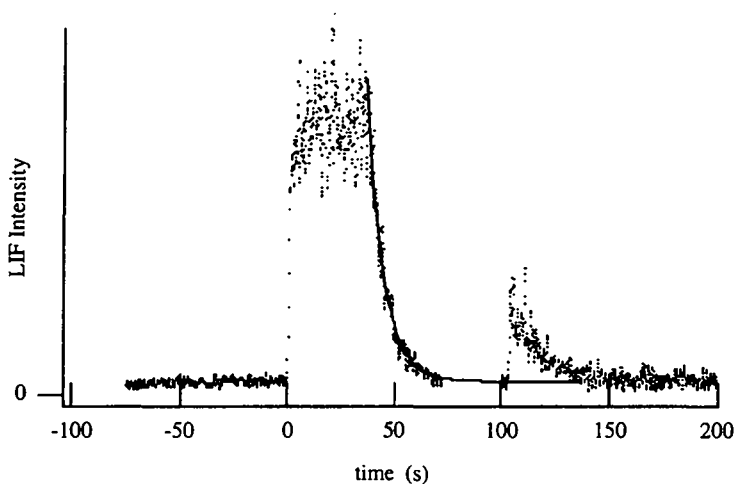**Figure 3.5 b:** Detection of NO by LIF *in situ* probing using the small orifice (1mm i.d.) and 56mg of FW2. NO flow rate: $(3.3\pm0.4)\cdot10^{15}$ #/s.

shut off at t~120 s. At t~170 s the NO_2 LIF signal drops to zero, the sample chamber is again opened and the remaining and/or desorbing NO_2 is detected.

In agreement with MS data the surviving quantity of NO_2 is quite small after 170 s of interaction in a static cell.

A similar experimental sequence was carried out while monitoring the NO fluorescence to the red of the excitation frequency at 226.9 nm. **Figure 3.5 b** shows the absence of NO until t=0 s at which time the prompt rise in the emission signal, representing the product NO from the interaction of the NO_2 with sample 1, appears. After approximately 40 s the sample chamber is closed and the NO signal decays to its original base line value at a rate in agreement with the escape of NO from the reference chamber of the LPR with the small orifice in place. During this time, the NO_2 flow is arrested until the m/e 46 MS signal (not shown) drops to zero. After the reference chamber is fully evacuated, the sample chamber is again opened at approximately t=100 s, and the remaining NO is allowed to escape from the sample chamber.

These results for the NO yield show good agreement within the experimental uncertainty when compared with those obtained using the molecular beam sampling MS data. Thus, we are confident in the method for calculating the NO flow rates from the difference of the corrected MS signal intensities at m/e 46 and m/e 30. Because of the time resolution limitation of our LIF system (10 Hz acquisition), MS detection has been used for all of the subsequent analysis where higher time resolution necessary to observe the prompt changes in signals upon exposure of the reactive surfaces to NO_2 was required.

Table 3.2 presents data on pulsed dose experiments of NO_2 on the three amorphous carbon samples used. From pulsed NO_2 exposure to first-used samples of amorphous carbon at limiting low doses we obtain k_{eff} values of 8.0 ± 2.4 s^{-1} (entry e), 12.0 ± 3.6 s^{-1} (entry m) and 8.5 ± 1.7 s^{-1} (entry n) for samples 1, 2 and 3, respectively, which all have overlapping error bars. These rate constants (k_{eff}) were obtained from a single-exponential fit of the time-dependent mass spectrometer signals starting at 80% of the peak value. This delay was used to account for the finite rise time of the MS signal corresponding to the build-up time of the NO_2 density inside the Knudsen cell. This result is noteworthy in view of the differences among the carbon samples employed, including BET internal surface areas [20] and surface acidity, and production methods. This implies that the initial uptake is independent of the microphysical and microstructural properties of the substrates.

Several entries to **Table 3.2** further reveal a significant decrease of k_{eff} with repetitive exposure to NO_2 even though the sample may have been evacuated for a period exceeding 10 hours at a background pressure of 10^{-4} Torr or may have undergone heat treatment using a 375 W incandescent lamp

irradiating the sample across the glass envelope of the LPR for several tens of minutes. Entries a to c in **Table 3.2** represent a series of consecutive runs of sample 1 each separated by a heat treatment. Decreasing values for k_{eff} reveal aging for sample 1. Entry e of **Table 3.2** describes the result of a pulsed valve experiment performed under a limiting low dose of NO_2 at $1.8 \cdot 10^{14}$ molecules per pulse. The individual values of k_{eff} yield a mean of 8.0 ± 2.4 s^{-1} with a significant standard deviation due to the low MS signal levels at m/e 46 discussed above. Entries f, g, h and i of **Table 3.2** demonstrate the decrease in k_{eff} due to the aging of the sample upon repetitive exposure of NO_2 and due to higher NO_2 doses. Increasing the dose of NO_2 has the same effect as the aging albeit for different reasons within the framework of the model considered here: The aging presumably reduces the available surface sites for NO_2 adsorption due to irreversible chemical conversion into surface oxides such as {C•O} (reaction (8)), whereas a high dose "loads" the sample surface and increases the rate of desorption (reaction (-4) and (-5)) thus decreasing the net uptake rate. This aging due to accumulation of metastable surface products resulting from an oxidation-reduction reaction such as (8) is partially reversible as evidenced by desorption of stable molecules such as CO and CO_2 upon heat treatment or prolonged pumping and concomitant recovery of the sample's ability for NO_2 adsorption.

The heat treatment using an incandescent lamp results in generation of CO and some CO_2 whose precursor presumably is the unspecified "surface oxide" {C•O} presented in reaction (8) [21]. As mentioned above, the same aging behavior for the samples is seen for entries n and o (**Table 3.2**) where the pulsed dose experiment has been performed on two different aliquots of sample 3. Entry m pertains to amorphous carbon sample 2 whose effective uptake kinetics (k_{eff}) seems to be somewhat faster than the one for sample 1 and 3. However, the average k_{eff} are not significantly different given the standard deviations. The results under entries k and l have been discussed above and relate to scaling of k_{eff} to the geometric surface area. Entry d of **Table 3.2** relates to a pulsed valve experiment performed in the small aperture LPR and shows small values for k_{eff} for the reason discussed above (importance of desorption, equation (9)).

Table 3.2: Effective first order uptake rate constants determined from pulsed valve first exposure of carbon samples to NO_2. All k_{eff} are for the large orifice reactor except for series d, which was obtained using the small orifice reactor [a].

series/ sample	mass (mg)/ comments [b]	time sequence	total NO_2 dose in sequence (10^{15}molec.)	NO_2 release (10^{15}mo- lecules)	k_{eff} (s^{-1})	k_{eff} (s^{-1}) averaged
a /FW2	24.6	1	5.71	0.772 [c]	6.9	6.2
		2			6.1	
		3			5.8	
b /FW2	(H.T. @ (7))	4			5.1	4.9
		5			5.0	
	(H.T. @ (10))	6			4.9	
c /FW2	(H.T. @ (14))	14			4.6	4.6
		15			4.7	
		16			4.7	
d /FW2	Small Orifice	17	17.0	1.46 [c]	1.3	1.0
	(overnight	18			1.1	
	pumping)	19			0.9	
		20			0.8	
e /FW2	12 days	1	0.179	0.0234 [c]	6.1	8.0
	(Heat treatment	2			5.6	
	before first	3			10.8	
	exposure.)	4			8.0	
		5			10.1	
f /FW2		6		0.0166 [c]	7.0	6.7
		7			7.4	
		8			5.7	
		9			6.8	
		10			6.7	
g /FW2	(H.T. @ 11)	16		0.0252	6.1	6.5
		17			8.9	
		18			6.2	
		19			4.9	
h /FW2		20	4.56	0.447 [c]	5.9	5.6
		21			5.9	
		22			5.7	
		23			5.7	
		24			5.7	
		25			5.5	

[a] The effective rate constant, $k_{eff} = (k_1+k_2) \cdot \{S\} + k_e$ where $\{S\}_0$ is the number of carbon sites available to uptake of NO_2 at time t=0. The values for k_{eff} are in units of s^{-1}. The quoted rate constants are determined from the best exponential fit to approximately one second of data commencing at 80% of the maximum recorded intensity.

[b] H.T. @ (time sequence): Specifies incandescent lamp heat treatment of the amorphous carbon sample just prior to time sequence mentioned in parenthesis.

[c] Exponential fit to the integral used to obtain value.

Table 3.2 (continued): Effective first order uptake rate constants determined from pulsed valve first exposure of carbon samples to NO_2.

series/ sample	mass (mg)/ comments	time sequence	total NO_2 dose in sequence (10^{15}molec.)	NO_2 release (10^{15}mo-lecules)	k_{eff} (s^{-1})	k_{eff} (s^{-1}) averaged
i /FW2	(H.T., pump overnight.)	1	4.56	0.701	5.9	5.5
		2			5.3	
		3			5.3	
j /FW2	50	1	0.29	0.558 d)	5.1	5.6
		2			5.9	
		3			5.9	
k /FW2	500	1	0.421	0.213	6.2	7.4
		2			9.0	
		3			4.7	
		4			6.4	
		5			11.0	
l /FW2	25 (17 mm dia.)	1	0.321	0.1899 c)	2.8	2.5
		2			2.4	
		3			1.4	
		4			5.1	
		5			1.3	
		6			2.1	
m /Printex 60	100	1	0.179	0.0149 e)	10.2	12.0
		2			8.4	
		3			-.-	
		4			13.0	
		5			16.8	
n /FS 101	100	1	0.233	0.027 f)	8.0	8.5
		2			7.5	
		3			10.4	
		4			6.4	
		5			10.2	
o /FS 101	100	6	1.9	0.16 g)	6.4	5.7
		7			5.1	
		8			6.0	
		9			6.3	
		10			5.6	
		11			4.9	

d) NO molecules released: $0.29 \cdot 10^{15}$ using exponential fit to the integral, $0.23 \cdot 10^{15}$ after 8 s.

e) NO molecules released: $0.041 \cdot 10^{15}$, i.e. 30% mass balance after 4 s.

f) NO molecules released: $0.69 \cdot 10^{15}$, i.e. 41% mass balance after 7 s.

g) NO molecules released: $0.11 \cdot 10^{15}$, i.e. 14% mass balance after 9.5 s.

One last point concerns the mass balance between the amount of NO_2 taken up and the amount of NO generated. Entry j in **Table 3.2** established a good mass balance for amorphous carbon sample 1: this type of carbon apparently has a high turn-over rate for NO_2 conversion reaching 100% even at ambient temperature. Entries m, n and o present a mass balance for samples 2 and 3

with a deficit in NO. The gas phase product NO represents 30 to 40% of the total NO_2 dose applied in the case of sample 2, whereas it is only 14% for sample 3 where the results have been obtained by numerical integration of the absolute concentrations vs. time. The difference between the NO_2 dose applied and the recovered gas phase NO product is bound to the solid sample in some unknown form. In contrast to the uptake kinetics, microstructural and microphysical details of the amorphous carbon structure affect the mass balance markedly in an inverse relationship: the more internal surface the amorphous carbon presents to the active gas once it is adsorbed, the higher is its activity towards conversion of NO_2 to NO. A highly structured amorphous carbon will present many more active internal sites for chemical conversion than does a coarser one. This proposition will be confirmed by the results of the steady-state experiments to be discussed next.

2.4.2 Steady State Experiments

The steady state experiments were performed according to the protocol discussed in the experimental section (c. f. **Figure 3.1**). Due to the fact that all the amorphous carbon samples used showed signs of irreversibility in their uptake behavior upon repetitive exposures and attempted rejuvenation, a limited number of bracketing experiments were performed in order to keep the number of independent experiments to an acceptable level. **Table 3.3** shows the experimental conditions used to bracket the static pressure in the Knudsen cell for both the large and the small aperture LPR corresponding to NO_2 lifetimes of 1.1 and 17.2 s, respectively. The flow rates were varied in the range $2 \cdot 10^{14}$ to $2 \cdot 10^{16}$ molecules s^{-1} and the limiting (extreme) experimental conditions were labeled "L low", "L high", "S low" and "S high" meaning large aperture LPR/low flow rate and so on. The four extreme conditions cover a factor of 15 in residence time and two orders of magnitude in static pressure due to a corresponding variation in flow rate. In numerous experiments it was verified that the uptake kinetics under experimental conditions in between the stated extremes were a continuous function interpolating between the external conditions.

Figure 3.6 displays the data for NO_2 uptake and the NO generation on 50 mg amorphous carbon sample 1 calibrated in molecules per seconds. These data are based on the time-dependent MS signal at m/e 46 (NO_2^+) and m/e 30 (NO^+) and on flow rate measurements of NO_2 and NO. **Figure 3.6** is subdivided into four panels each showing the four limiting experimental conditions discussed above.

Table 3.3: Summary of continuous flow experiments.

aperture, flow rate	sample	flow rate (10^{15}#/s)	R_{ss} [a]	$MIN^R_{NO_2}$ [b]	$SS^R_{NO_2}$ [c]	SS^R_{NO} [d]
small, high	FW2 (50 mg)	9.27	2.7	0.02	0.02	0.75
	PR_60 (100 mg)	14.5	2.9	0.06	0.06	0.10
	FS101 (100 mg)	7.0	2.9	0.26	0.28	0.08
small, low	FW2 (50 mg)	0.14	3.2	0	0	0.9
	PR_60 (100 mg)	0.26	5.5 [e]	0	0	0.06
	FS101 (100 mg)	0.07	3.0	0	0	0
large, high	FW2 (50 mg)	6.4	3.3	0.12	0.12 [f]	>0.84 [f]
	PR_60 (100 mg)	17.7	3.3	0.10	0.17	0.09
	FS101 (100 mg)	5.3	3.3	0.15	0.40	0.10
large, low	FW2 (50 mg)	0.28	3.3	0.09	0.09 [f]	0.67 [f]
	PR_60 (100 mg)	0.18	3.3	0.05	0.09	0.04
	FS101 (100 mg)	0.14	4.2	0.10	0.11	0.16

[a] R_{ss}: ratio of MS intensity (m/e 30 / m/e 46), non reactive conditions.

[b] $MIN^R_{NO_2}$: ratio of minimum NO_2 reactive flow rate to the SS non reactive level.

[c] $SS^R_{NO_2}$: ratio of largest NO_2 reactive flow rate to the SS non reactive level. Values in this column measured at 5 s.

[d] SS^R_{NO} : ratio of largest NO reactive flow rate to the NO_2 non reactive level. Values in this column measured at 5 s.

[e] NO impurity subtracted for determination of mass value.

[f] Value obtained by exponential extrapolation to apparent asymptote.

Figure 3.6 a: Best simulation fit to NO_2 uptake experiment on 50mg of FW2 using the large reactor orifice (3mm i.d.) and a high NO_2 flow of $6.4 \cdot 10^{15}$ #/s.

Figure 3.6 b: Best simulation fit to NO_2 uptake experiment on 50mg of FW2 using the large reactor orifice (3mm i.d.) and a low NO_2 flow of $2.9 \cdot 10^{14}$ #/s.

Figure 3.6 c: Best simulation fit to NO_2 uptake experiment on 50mg of FW2 using the small reactor orifice (1mm i.d.) and a high NO_2 flow of $9.3 \cdot 10^{15}$ #/s.
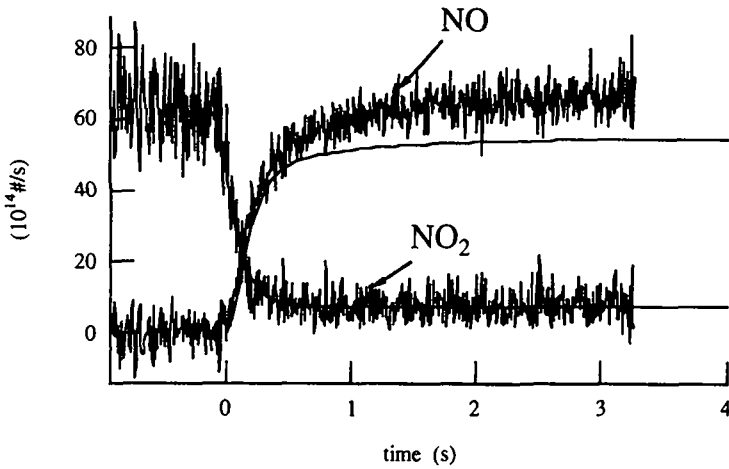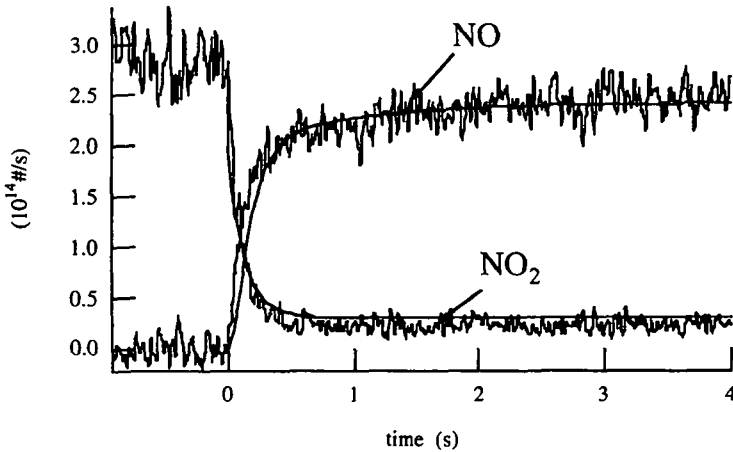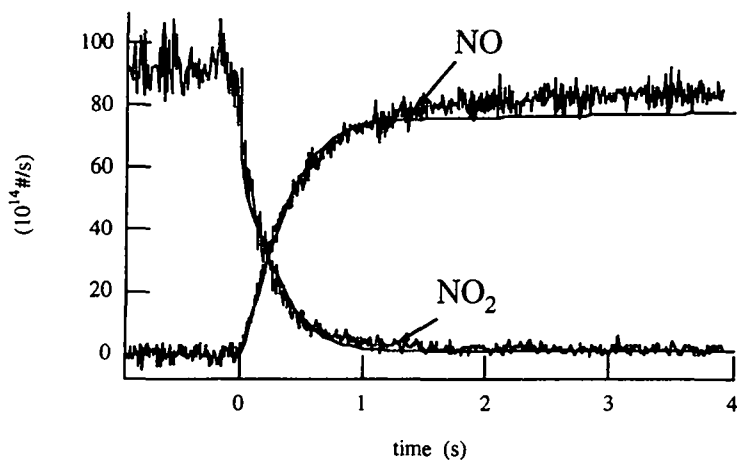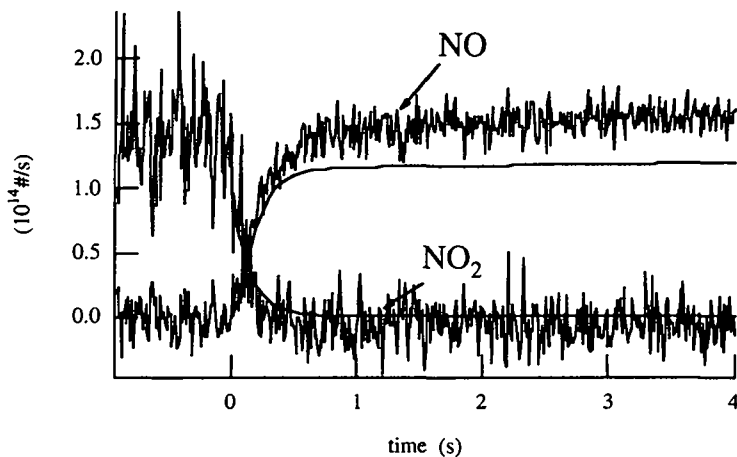

Figure 3.6 d: Best simulation fit to NO_2 uptake experiment on 50mg of FW2 using the small reactor orifice (1mm i.d.) and a low NO_2 flow of $1.4 \cdot 10^{14}$ #/s.

Experiments in which only the disappearance of a gas-phase species in the presence of an active surface is measured address only the *net* uptake of the gas phase species. That is to say that the experimental data do not usually allow the separate determination of k_1 and k_{-1}, or correspondingly k_2 and k_{-2} for the inhibition process, except under conditions where the back reactions can be excluded with some degree of certainty. Furthermore, our data do not allow the separation of $k_1 + k_2$ from $\{S\}$ in the rate expression for adsorption of NO_2 on $\{S\}$ because only the disappearance of NO_2 from the gas phase is observed and no information on a molecular adsorbate such as $\{NO_2 \bullet S\}_p$, $\{L\}$ or $\{NO_2 \bullet I\}$ is gained from the present experiments. Our experimental results thus do not address the detailed microphysico-chemical properties of the substrate. This in turn means that the fitting of the NO_2 uptake kinetics is sensitive only to the ratio $(k_1 \cdot \{S\}/k_{-1})$ and $(k_2 \cdot \{S\}/k_{-2})$ regardless of the absolute magnitude of the individual microscopic rate parameters. On the other hand, the surface chemistry, such as the NO generation from NO_2 uptake, is sensitive to the microstructural and chemical characteristics of the amorphous carbon sample [22]. In other words, our present experimental method will give us an effective kinetic parameter set for the NO_2 uptake together with a fitted result for the kinetics of formation of the reaction product NO. However, an unambiguous separation of the detailed adsorption/desorption kinetics in terms of rate constants and surface densities $\{S\}$ in equations (4) and (5) is not possible for the present data set.

We use the experimental information obtained from the pulsed valve experiments to guide us in the selection of certain rate constants for the chemical kinetic model that simulates the steady state experiments. For example, we used the measured value of $(k_1 + k_2) \cdot \{S\}$ from the pulsed valve experiments for the chemical kinetic model thereby making the tacit assumption that k_{-1} is small in relation to k_3. This assumption is warranted by our qualitative observation that at least for sample 1 and 3 desorption processes of a surface exposed to a high dose of NO_2 take exceedingly long at ambient temperature. We obtained an experimental value of $k_1 \cdot \{S\}$ by subtracting k_e^L and $k_2 \cdot \{S\}$ from the measured value of k_{eff} tabulated in **Table 3.4** and neglecting the remaining terms in equation (9). This approximation was verified through chemical kinetic modeling as the pulsed valve experiments were simulated under limiting low dose conditions in which the desorption rates (-1) and (-2) are presumed to be negligible. Assuming that no build-up of physisorbed NO_2 had occurred, this is equivalent to separating the adsorption from the desorption rate by conducting the pulsed valve experiment under conditions where the desorption rate vanished.

Table 3.4: Summary of model rate constants (transferable constants in parenthesis) corresponding to a surface to volume ratio $A_s/V = 10.8/750 = 1.4 \cdot 10^{-2}$ cm^{-1}.

rate constant	FW 2	Printex 60	FS 101
CR12	0.97	0.80	0.1
{S}	$2 \cdot 10^{16}$	$5 \cdot 10^{16}$	$6 \cdot 10^{16}$
k_{eff}^L (s^{-1})	8.0 ± 2.3	12.0 ± 3.6	8.5 ± 1.8
k_1 s^{-1} (cm$^2 \cdot$s^{-1})	$3.43 \cdot 10^{-16}$ ($37 \cdot 10^{-16}$)	$1.78 \cdot 10^{-16}$ ($19.2 \cdot 10^{-16}$)	$0.13 \cdot 10^{-16}$ ($1.4 \cdot 10^{-16}$)
k_{-1} s^{-1} (cm$^{-1} \cdot$s^{-1})	0.0	30 (0.432)	0.01 (0.14)
k_2 s^{-1} (cm$^2 \cdot$s^{-1})	$0.12 \cdot 10^{-16}$ ($1.3 \cdot 10^{-16}$)	$0.45 \cdot 10^{-16}$ ($4.9 \cdot 10^{-16}$)	$1.14 \cdot 10^{-16}$ ($12.3 \cdot 10^{-16}$)
k_{-2} s^{-1} (cm$^{-1} \cdot$s^{-1})	0.005 ($7.2 \cdot 10^{-5}$)	0.10 (1.4)	0.40 (5.8)
k_3 s^{-1} (cm$^{-1} \cdot$s^{-1})	20 (0.29)	80 (1.2)	15) (0.22)
k_4 s^{-1} (cm$^{-1} \cdot$s^{-1})	0.0	500 (7.2)	100 (1.4)
k_5 s^{-1} (cm$^{-1} \cdot$s^{-1})	100 (1.4)	100 (1.4)	200 (2.8)

Even though the adsorption/desorption process (equation (4) and (5)) is reversible, the rate of desorption of NO2 from the weakly bound state {NO2•S}p and {L} turned out to be negligible upon fitting the data using the chemical kinetic model. This is no big surprise as we forced the chemical kinetic model to suppress the desorption rate as we set $k_{-1} \ll k_3$ (see above). This choice can be rationalized in terms of the large number of internal adsorption sites such as {NO2•I} that preferentially bind NO2 rather than release it into the gas phase. Even though we do not have accurate information as to the exact number of internal adsorption sites that can bind NO2 we assume that their number scales with the BET surface measured for each type of amorphous carbon. Experimentally we thus determine the product $k_1 \cdot$ {S} which is a pseudo first-order rate constant under limiting low dose conditions (surface coverage of 3 to 6%), whereas the microscopic rate constant for adsorption (k_1) is a second order rate constant. We attach some importance to this methodology of combining the results of the pulsed valve experiments with the steady-state results as it leads to effective reduction of the adjustable rate parameters in the chemical kinetic model, albeit under one simplifying assumption of setting a value for k_{-1}.

The numerical simulation of the steady state and pulsed valve results for sample 1 carbon requires a value of $2 \cdot 10^{16}$ sites for the total surface of 10.8 cm^2, corresponding to $1.9 \cdot 10^{15}$ sites/cm^2. It is instructive to see what the corresponding dimension of adsorbed NO_2 would be in comparison with estimated hard-sphere collision diameters obtained from gas-phase experiments in order to get an idea of the packing density of NO_2 adsorbed on amorphous carbon. According to one of the conclusions from our pulsed valve results, which allows us to treat the surface of the exposed carbon as an external surface, we can arrange the weakly bound NO_2 species in a closely packed arrangement on a flat surface and deduce a hard sphere diameter d of 2.50 Å according to the following equation $d = \sqrt{\dfrac{10^{16}}{0.866n}}$ (10), where n is the number of molecules per cm^2 and d is the size parameter in Å corresponding to the molecular diameter of NO_2 that has been approximated as a sphere. There are no values of van der Waals radii for NO_2 in the literature. As a comparison we cite NO with a measured van der Waals radius of 3.2 to 3.5 Å, and N_2O with a radius of 3.8 to 4.6 Å [23]. If one takes a volume filling model based on van der Waals radii for N and O of 1.5 and 1.4 Å, respectively, one would arrive at an equivalent sphere diameter of 4.1 Å. We conclude that the external surface can take up approximately three times $(1.9 \cdot 10^{15}/6.5 \cdot 10^{14})$ as many molecules of NO_2 compared to a completely specular (geometric) surface, which would lead to a saturation coverage of $6.5 \cdot 10^{14}$ molecules/cm^2 at an estimated NO_2 hard-sphere diameter of 4.1 Å based on simulations for experiments employing sample 1. The number for the surface site density of $1.9 \cdot 10^{15}$ sites cm^{-2} resulting from our fits can be compared to a number of $2.3 \cdot 10^{15}$ sites cm^{-2} that was used in a detailed chemical kinetic model to describe soot nucleation and growth [24]. The close agreement between the two numbers is noteworthy in that {S} in our approach resulted from fits to adsorption data, analogous to Frenklach and coworkers who arrived at similar values based on theoretical/geometrical considerations of homogeneous and heterogeneous (soot) flame data.

The kinetic parameters for the simulation of NO_2 uptake experiments on sample 1 amorphous carbon are listed in **Table 3.4** and the fits are displayed in **Figure 3.6** together with the experimental data. Each rate constant is given in "system" units where the rates are expressed in # s^{-1}. These chemical conversion rates apply solely to the present volume and total surface area available in our LPR.

A glance at **Figure 3.6** reveals a good fit to both the uptake kinetics and NO production. **Figure 3.6 d** displays the early-time behavior in some more detail for the high flow rate/small aperture LPR. The precipitous drop of the

NO_2 partial pressure due to the opening of the sample chamber is not clearly visible due to the fact that the plunger is operated manually, and there is clearly an ambiguity of where "time zero" has to be located. Moreover, a fact that the fit between experiment and model has to take into account, is that the uptake parameters control the rate of decay of the MS signal of NO_2 towards steady-state as well as the magnitude of the steady-state signal itself, even though the two phenomena are kinetically distinct in time.

Examination of the different experiments displayed in **Figure 3.6** reveals that including equation (5) is not necessary. However, when the long-term exposure for this sample was investigated, decrease of the adsorption rate, presumably due to poisoning of the surface by {C•O} or some other species, was observed and, though small, k_2 in the mechanism was found to be of significant importance [22]. The most striking feature of the sample 1 amorphous carbon is the fast tracking of the NO generation with the NO_2 uptake. This is the most noticeable feature of sample 1 compared to both sample 2 (Printex 60) and sample 3 (FS 101). All limiting experimental conditions presented in **Figure 3.6** show a one-to-one time correspondence of NO_2 to NO conversion. The mass balance is also conserved within the experimental uncertainty with 100% of the NO_2 showing up as NO product. These observations along with simulations show that there is no major build-up of an additional intermediate on the carbon sample even after integrated doses of 10^{19} molecules of NO_2.

Representative results for the time-dependent uptake of NO_2 on sample 2 (Printex 60) are displayed in **Figure 3.7 a** and **b** together with simulation fits using the parameters given in **Table 3.4**. In contrast to the results for sample 1, the NO yields for sample 2 are greatly diminished relative to the amount of NO_2 adsorbed. According to the kinetic parameters displayed in **Table 3.4**, the sample transfers the NO_2 into the intermediate state {NO_2•I} associated with internal surface sites (reaction (6)). This transfer reaction is crucial to the ability of the amorphous carbon to continue the adsorption of NO_2 from the gas phase while processing adsorbed NO_2 on its internal surface. Reaction (6) is followed by a rapid transfer of the intermediate {NO_2•I} to a terminal repository {NO_2•R} (reaction (7)). Since the number of internal surface sites (related to the BET surface) compared to the projected, geometrical, surface is so large, we do not explicitly define the internal sites in the rate law for reaction (6), its justification being that no significant change in their total number can occur for the absolute flows of NO_2 used in our studies. The rate law for reaction (6) is therefore given by unimolecular decay of the weakly bound species {NO_2•S}$_p$.

From **Table 3.4**, the branching ratio $k_5/(k_4+k_5)$ is found to be 1/6. Inspection of **Figure 3.7** shows that this corresponds roughly to the yield of NO in comparison with the total uptake of NO_2. With the aid of the model, we can estimate the density of surface species; simulations reveal that, due to the significant population of the {L} state, the branching $k_5/(k_4+k_5)$ overestimates the yield of product NO on the time scale of a few seconds after the start of the NO_2 uptake experiment. This time corresponds roughly to the population of {L}. At longer times, the ability of the sample to adsorb NO_2 decreases to a point that corresponds to 10-20% of the rate of initial uptake. Poisoning or saturation effects at long reaction times could be introduced into our model by explicitly including the number of internal adsorption sites in equations (6) through (8) thus leading to saturation of $\{NO_2 \bullet I\}$, $\{NO_2 \bullet R\}$ and $\{C \bullet O\}$.

In comparing the time response of the MS signal at m/e 46 for the large (**Figure 3.7 a**) and small aperture reactor (**Figure 3.7 b**) upon opening of the sample chamber, we notice a slower approach to steady state in the small compared to the large aperture LPR. This behavior is quite general and can be understood in terms of the differing values for k_e representing different time scales on which the rate of chemical reaction which is comparable to the effusion rate is measured. Thus, the homogeneous gas phase in the large orifice LPR relaxes ten times faster to a new steady state compared to the same process in the small orifice LPR. The reason lies in the fact that at the same flow rate the gas density is approximately ten times larger in the small orifice LPR compared to the one in the large orifice LPR so that partial pressure changes in the small orifice LPR take longer because more molecules are involved.

Typical data for the third type of amorphous carbon, sample 3, are displayed in **Figure 3.8 a** and **b**. As for all the previous figures each one represents a new sample and a first-ever exposure to NO_2. The kinetic behavior is similar to the one for sample 2 with respect to initial uptake and NO yield, even though the kinetic parameters displayed in **Table 3.4** are significantly different. The onset of saturation for the large orifice LPR (**Figure 3.8 a**) at a few seconds into the uptake experiment is reproducible and considered to be one of the more noticeable features of sample 3. Comparing **Figure 3.8 a** with **Figure 3.7 a** we notice that the NO yield relative to the NO_2 adsorbed is similar for sample 3 and sample 2 in the case of the large orifice LPR and high flow rate. This holds even though the rate parameters in the branching of the intermediate species $\{NO_2 \bullet I\}$ in reactions (7) and (8) are significantly different. From the

Figure 3.7 a: Best simulation fit to NO_2 uptake experiment on 100mg of PRINTEX 60 using the large reactor orifice (3mm i.d.) and a high NO_2 flow of $1.8 \cdot 10^{16}$ #/s.

Figure 3.7 b: Best simulation fit to NO_2 uptake experiment on 100mg of PRINTEX 60 using the small reactor orifice (1mm i.d.) and a high NO_2 flow of $1.5 \cdot 10^{16}$ #/s.
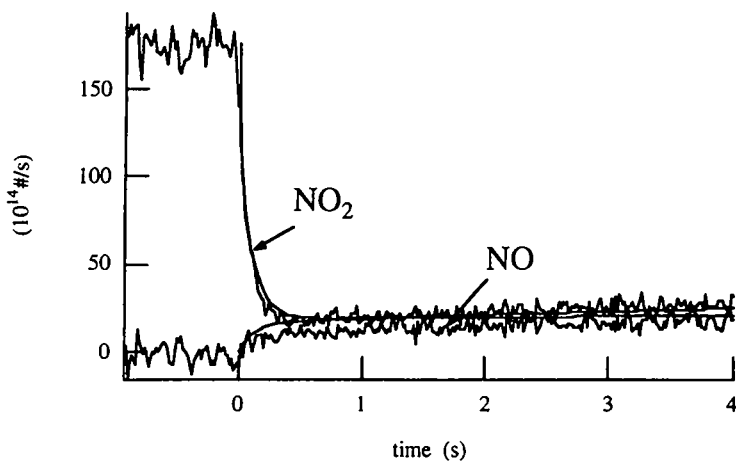
Figure 3.8 a: Best simulation fit to NO$_2$ uptake experiment on 100mg of FS 101 using the large reactor orifice (3mm i.d.) and a high NO$_2$ flow of $5.3 \cdot 10^{15}$ #/s.
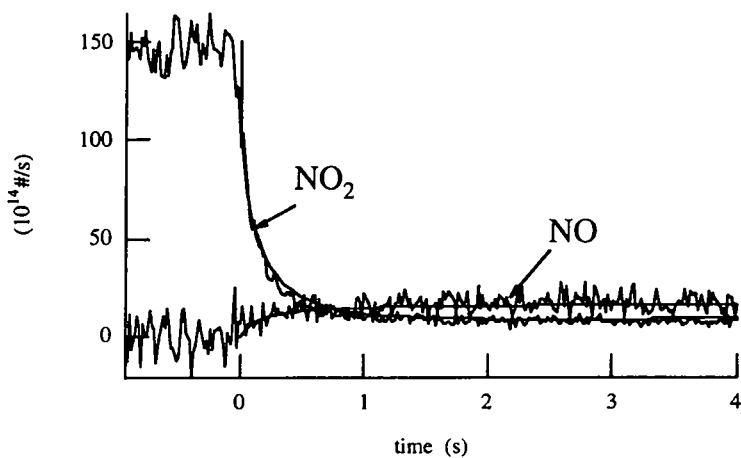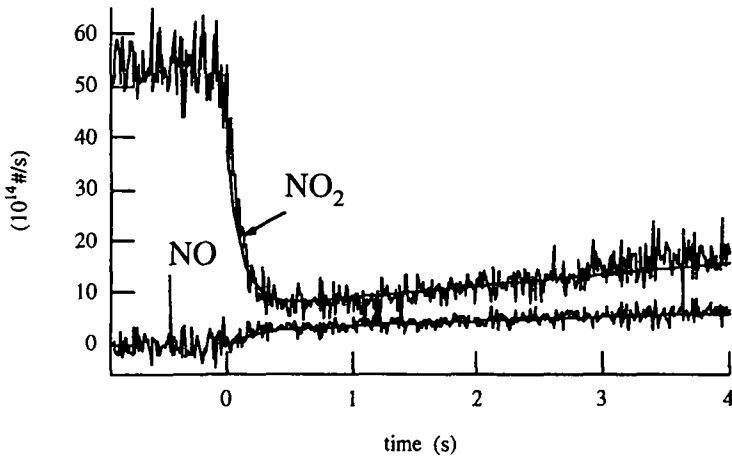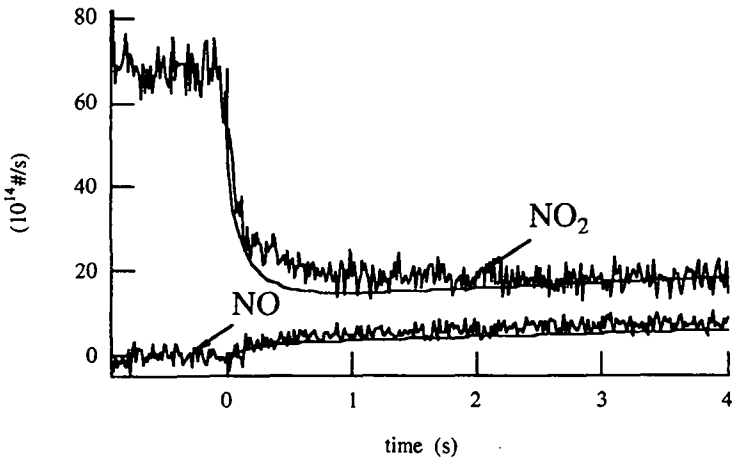

Figure 3.8 b: Best simulation fit to NO$_2$ uptake experiment on 100mg of FS 101 using the small reactor orifice (1mm i.d.) and a high NO$_2$ flow of $7.0 \cdot 10^{15}$ #/s.

discussion of the NO yield in sample 2 we recall that the branching ratio $k_5/(k_4+k_5)=1/6$ roughly reflected the yield of NO relative to NO_2 adsorbed. Why then does the yield of NO for sample 3 not correspond to the branching ratio of 2/3? In the following paragraph we make an attempt at explaining this apparent paradox in semi-quantitative terms using a situation where saturation phenomena are absent on the time scale of interest (large orifice LPR).

The surface coverage of $\{NO_2 \bullet S\}_p$ is controlled by two competing processes: k_{-1} leads to desorption of NO_2 back to the gas phase, whereas k_3 transfers physisorbed NO_2 into the intermediate state $\{NO_2 \bullet I\}$ that branches into NO + $\{C \bullet O\}$. In comparing the values for sample 2 and 3 in **Table 3.4** one notes that the branching ratio for transfer, $k_3/(k_3+k_{-1})$ is 1 for sample 3 compared to 2/3 for sample 2. The net relative efficiency for NO production should therefore be $2/3 \cdot 1/6=1/9$ for sample 2 as opposed to $1 \cdot 2/3=6/9$ for sample 3. On this basis one would expect a NO yield larger by a factor of 6 for sample 3 compared to sample 2, which obviously is not the case. The answer to this discrepancy lies in looking at the ratio of the absolute magnitude of k_3 and not just the relative branching ratios: k_3 for sample 2 is roughly six times as large as k_3 for sample 3 which makes the absolute rates of NO formation in both samples comparable. This reasoning is valid due to the fact that the initial NO_2 adsorption rate for both samples is equal within experimental error, a result that was discussed above in conjunction with the pulsed valve results (k^L_{eff} in **Table 3.4** and $(k_1+k_2) \bullet (\{S\})$ in equation (9)).

In comparing the kinetic parameters for sample 2 and 3 there is another important difference that becomes apparent when one considers the relative importance of the reactive vs. non-reactive adsorption step, k_1 vs. k_2. **Table 3.4** displays the branching ratio CR12= $k_1/(k_1+k_2)$ corresponding to the fractional reactive uptake of NO_2 by amorphous carbon as opposed to the temporary non-reactive uptake. Sample 3 is characterized by a large non-reactive uptake rate leading to an important surface coverage of NO_2 blocking the reactive uptake that takes NO_2 through the various reactive surface states ultimately leading to NO. On sample 2, on the other hand, non-reactive uptake of NO_2 is less important than on sample 3, but it leads nevertheless to a sizable surface coverage on the order of 20% of the external surface. The surface coverage at steady-state of the reactive physisorbed NO_2, $\{NO_2 \bullet S\}_p$, is much smaller than $\{L\}$ due to the fact that k_3 is by far larger than k_{-1} for all samples thus preventing the build-up of a sizable population of reactive precursors for the formation of NO (see discussion above).

The rate parameters displayed in **Table 3.4** reveal important differences in the kinetic behavior of the three samples which span the extremes of

commercially available amorphous carbon inasmuch as microphysical parameters are concerned. While clearly the microstructural details are not the only, nor possibly most, important properties of the sample studied, it is quite remarkable that a simple reaction mechanism as proposed describes the main features of the kinetic behavior of the NO_2 uptake on all three amorphous carbon samples, albeit for short reaction times. It is not clear to what extent the detailed structure of carbon will affect the kinetic results dealing with NO_2 as a surface probe. The elucidation of the carbon structure on the molecular level is an ongoing effort. As an example one can cite the successful modeling of soot growth from hydrocarbon fuels resulting in graphite-like carbon structures [23] as opposed to experimental results according to which at least some aromatic layers are held together by covalent bonds [25].

Table 3.5 a: Summary of results. Initial uptake coefficients.

	$(k_1 + k_2) \cdot \{S\}$ (s^{-1})	γ a)	% error
FW 2	7.1 ± 2.3	$(5.1 \pm 1.7) \cdot 10^{-2}$	32
Printex 60	11.1 ± 3.6	$(8.3 \pm 2.7) \cdot 10^{-2}$	32
FS 101	7.6 ± 1.8	$(5.7 \pm 1.3) \cdot 10^{-2}$	22

a) $<\gamma> = (6.4 \pm 2.0) \cdot 10^{-2}$.

Table 3.5 a presents a concise summary of the results. The initial uptake coefficient of NO_2, averaged over all three amorphous carbon samples at ambient temperature and determined from pulsed valve experiments, is $(6.4 \pm 2.0) \cdot 10^{-2}$ with the gas-wall frequency $\omega = (c A_s/4V) = 134$ s^{-1}, where c is the mean molecular velocity for NO_2 at 300K, V is the volume of the total LPR (750 cm^3) and A_s is the external surface over which the sample is spread out. **Table 3.5 b** presents the fitted external surface $\{S\}$ for the three amorphous carbon samples together with the estimate for a formal monolayer coverage of NO_2 on a flat surface as discussed above. The value for $\{S\}$ estimated by Frenklach in connection with soot modeling is straddled by our fitted results for the three samples [23].

Table 3.5 b: Summary of results. Surface sites.

	{S} [cm^2]	d [Å]	r^2 a)	BET [m^{2}g^{-1}]	pH b)
FW 2	1.85·10^{15}	2.50	2.8	460	2.5
Printex 60	4.60·10^{15}	1.60	6.8	115	9.5
FS 101	5.60·10^{15}	1.44	8.4	20	7.0
model external surface	0.65·10^{15}	4.20	1.0	1	-

a) $r^2 = (4.2/d)^2$ is proportional to saturable (apparent) surface that yield the best
   fit to the steady state experiments.
b) Surface pH according to product specification by DEGUSSA [18].

2.4.3 Concurrent H$_2$O/NO$_2$ Experiments

When an amorphous carbon sample that has been previously exposed to
NO$_2$ is heated in the LPR a significant quantity of H$_2$O and CO as well as a
small amount of CO$_2$ are released. The volumetric pumping speed is equal to
k_e·V and corresponds in our experiments to one l s^{-1} (large orifice) which is small
by common vacuum standards. We examined the NO$_2$ uptake under
concomitant H$_2$O dosing in order to search for a synergistic effect of NO$_2$ and
water vapor as has been found for the hydrolysis of N$_2$O$_5$ on activated carbon
[26], [27]. No uptake of H$_2$O on any of the three types of amorphous carbon
samples was found, even when the uptake experiment was performed after
prolonged pumping of the carbon samples. Furthermore, the steady state rate
constants for the reactive uptake of NO$_2$ by amorphous carbon was unaffected by
the presence of water vapor in most cases. When an amorphous carbon sample 2
was heated prior to an uptake experiment and subsequently exposed to a
concomitant flow of NO$_2$ and H$_2$O after cooling down to ambient temperature,
we observed a steady state rate constant for reactive uptake that was enhanced
by only a factor of 1.5. In contrast to activated carbon which can take up large
amounts of H$_2$O vapor, the interaction of water vapor with amorphous carbon
seems to be negligible on the time scale of our experiments (seconds), a result
that was also confirmed in field studies on water uptake of aerosols on a much
longer time scale [28]. Therefore we do not expect any chemistry involving NO$_2$
and H$_2$O according to equation (1), resulting in the formation of HONO and

HNO_3 which were never observed as monitored at m/e 47 and 63. These results are consistent with the hydrophobic nature of the reduced carbonaceous compounds used in our study.

A reference experiment involving the uptake of water vapor was performed in which 38 mg of Aerosil was exposed to flow rates of approximately $2 \cdot 10^{15}$ molecules s^{-1}. This sample was chosen because it presented a comparable internal surface area in relation to the amorphous carbon and was expected to be non-reactive with respect to NO_2. It contains pure SiO_2 and showed no signs of H_2O adsorption in both the large and the small orifice LPR. A second reference experiment was undertaken in which 196 mg of Aerosil was simultaneously exposed to a flow of H_2O ($1.7 \cdot 10^{15}$ molecules s^{-1}) and NO_2 with no signs of uptake of either H_2O or NO_2.

2.4.4 Additional Reaction Products

A final remark concerns the behavior of sample 1 that was exposed to a dose of NO_2 and subsequently heated under vacuum in the absence of any flow of NO_2. When the incandescent heat lamp was turned on a significant MS signal at m/e 62 (NO_3^+) was detected in addition to CO and CO_2 discussed above, and disappeared when the lamp was turned off. This signal either corresponds to NO_3 free radical or N_2O_5 which is significantly dissociated into $NO_3 + NO_2$ at the background pressure of less than 10^{-4} Torr. We are unable to attribute this reaction to either heat or visible light as we cannot separate the two in the present experiments. Apparently, the surface oxide {C•O} not only transforms the amorphous carbon into its volatile oxides CO and CO_2 but also oxidizes adsorbed NO_2 to its highest oxidation state N(V) according to equation (11):

$$\{C \bullet O\} + NO_2(\text{ads.}) \rightarrow NO_3(N_2O_5) \tag{11}$$

The species NO_2(ads.) may correspond to any surface species described in the mechanism equations (4) to (8) with the exception of $\{NO_2 \bullet S\}_p$ as the model predict too short a lifetime for this species. We will address this mechanism in a more quantitative manner in future experiments.

2.5 Conclusions

The investigation of the uptake kinetics of NO_2 on three types of amorphous carbon of widely differing microphysical properties revealed the following major conclusions:

All three samples reveal a fast uptake of NO_2 that shows varying degrees of saturation depending on the detailed nature of the samples thus necessitating time-resolved monitoring techniques. The initial NO_2 uptake rate appears to be *independent* of the microphysical properties of the amorphous carbon (e.g., internal (BET) surface, surface acidity) within the uncertainties of our measurements although a slight dependence of this property on the effective surface area is suggested by the results of the chemical kinetic modeling. We have observed an inverse scaling of the effective surface area {S} for NO_2 uptake on the measured internal surface area of the amorphous carbon (BET surface area).

The reaction mechanism for the uptake and heterogeneous chemical reaction of NO_2 is complex and involves competing adsorption as well as sequential Langmuir-Hinshelwood type surface reactions that are not directly measured in this experiment.

The only major reaction product observed is NO resulting from redox type chemistry on the surface of the amorphous carbon. Chemical kinetic modeling of the rate of formation of NO revealed significant differences among the three types of amorphous carbon. No interaction of water vapor with NO_2 in the presence of amorphous carbon was observed under the low pressure conditions of the present study.

In order to assess the importance of the here presented heterogeneous reactions in atmospheric chemistry, they are compared to corresponding gas phase reactions. The adsorption of NO_2 to carbon aerosol particles may thus be regarded as a sink for NO_2 in the atmosphere. Assuming an elemental carbon concentration of 8 µg/m^3 for an urban atmosphere [29] with a mean particle diameter of 100 nm and a NO_2 concentration of 80 ppb found in polluted atmospheres [3], the heterogeneous loss rate, i.e. the rate of adsorption to carbon particles, is $\dfrac{d[NO_2]}{dt} = -B(100nm) \cdot n(d = 100nm) \cdot [NO_2] = 3.1 \cdot 10^9 \, \#/cm^3 \cdot s$ where B(100 nm) is the attachment coefficient for monodisperse particles of 100nm diameter and n(d=100 nm) is the particle number concentration of the size. The attachment coefficient has been described by Porstendörfer et al. [30] and may be simplified for $\gamma << 1$ to $B(d_p) = \frac{1}{4} \cdot \pi \cdot \bar{c} \cdot d_p^2 \cdot \gamma$, where the mean molecular velocity of NO_2 was taken as $\bar{c} = 3.74 \cdot 10^4$ cm·s^{-1}, the particle diameter

d_p=100 nm and the sticking coefficient as calculated in Table 3.5 a) as γ=6.4·10⁻². The particle number concentration n(d=100 nm) is calculated as the total carbon mass (8 µg/m³) divided by the mass of a sphere of amorphous carbon of 100 nm diameter assuming a density of amorphous carbon of 2g/cm³ [31]. In this way we assume that the amorphous carbon occurs in a single sized distribution of 100 nm diameter.

A major sink for NO_2 during daytime is the photolysis to O(3p). With a rate constant at 60° Zenith angle of k_p=6.5·10⁻³ s⁻¹ [32] this results in a rate of photolysis of $\dfrac{d[NO_2]}{dt} = k_p \cdot [NO_2] = 1.2 \cdot 10^{10} \, \#/cm^3 \cdot s$ which is of the same order of magnitude as the heterogeneous removal on carbon aerosol particles. However, it must be kept in mind that the calculated heterogeneous loss rate has to be considered as an initial rate. In addition, the particle size distribution is rather particular. Aerosol particles exposed over longer time periods may exhibit a significantly lower rate due to saturating surface coverage of the particles by NO_2.

The present results may also be compared to recent in situ experiments performed by Kalberer et al. [33]. These authors studied the interaction of NO_2 at very low gas phase concentrations (of the order of 1ppb) with monodisperse carbon aerosols under normal atmospheric conditions (about 25% rel. humidity). They determined a sticking coefficient for FW2 of γ=(2.4±1.4)·10⁻⁴ which is two orders of magnitude smaller than the value of the present study: γ=(5.1±1.7)·10⁻². This difference may be attributed on one side to the fact that in the present experiments on bulk carbon the interaction time of the gas molecules with the solid material may have been underestimated [34], [35], and on the other side to the fact that Kalberer et al. used packed and subsequently resuspended FW2 and graphite. These two aspect will be checked in a forthcoming study in which the interaction of NO_2 with pellets of amorphous carbon and graphite will be investigated.

2.6 References

[1] L. A. Barrie, Atmospheric Environment 1986, 20(4), 643;

[2] A. D. A. Hansen and T. Novakov, J. Atmos. Chem. 1989, 9, 347; A. D. A. Hansen, B. A. Bodhaine, E. G. Dutton and R. C. Schnell, Geophys. Res. Lett. 1988, 15, 1193.

[3] B.J. Finlayson-Pitts and J.M. Pitts Jr., Atmospheric Chemistry: Fundamentals and Experimental Techniques, John Wiley & Sons, New York, 1986.

[4] J. B. Heywood, 1988, Internal Engine Combustion Fundamentals, McGraw Hill Book Co., New York; J. B. Heywood, Prog. Energy. Comb. Sci. 1976, 1, 135.

[5] P. Degobert, Automobile et Pollution, Editions Technip, Paris 1992, p.252.

[6] M. Lenner et al., Atmospheric Environment 1983, 17, 1395; M. Lenner, Atmospheric Environment 1987, 21, 37.

[7] J. C. Hilliard and R. W. Wheeler, SAE paper 790691, 1979.

[8] R. P. Turco, Atmospheric Effects of Stratospheric Aircraft: A First Program Report, NASA Ref. Publ. 1272, 63 (1992).

[9] R. Pueschel, D. F. Blake, K. G. Snetsinger, A. D. A. Hansen, S. Verma and K. Kato, Geophys. Res. Lett. 1992, 19, 1659.

[10] C. Liousse, H. Cachier and S. G. Jennings, Atmospheric Environment 1993, 27A, 1203.

[11] F. Arnold, J. Scheid, Th. Stilp, H. Schlager and M. E. Reinhardt, Geophys. Res. Lett. 1992, 12 (24), 2421.

[12] R. C. Miake-Lye, High-Speed Civil Transport Aircraft Emissions in 'The Atmospheric Effects of Stratospheric Aircraft: A First Report', NASA Ref. Publ. 1272, 13 (1992).

[13] D. M. Smith, W. F. Welch, S. M. Graham, A. R. Chughtai, B. C. Wicke and K. A. Grady, Appl. Spectrosc. 1988, 42 (4), 674.

[14] M. S. Akhter, A. R. Chughtai and D. M. Smith, J. Phys. Chem. 1984, 88, 5334.

[15] S. E. Schwartz and W. H. White, Adv. Environ. Sci. Eng. 1981, 4,1; S. E. Schwartz and W. H. White, Adv. Environ. Sci. Eng. 1983, 6, 1; J. N. Cape, R. L. Storeton-West, S. F. Devine, R. N. Beatty and A. Murdoch, Atmospheric Environment 1993, 27A, 2613.

[16] J. N. Pitts, E. Sanhueza, R. Atkinson, W. P. L. Carter, A. M. Winer, G. W. Harris and Ch. N. Plum, Int. J. Chem. Kin. 1984, 16, 919; A. Febo, F. De Santis, C. Perrino and A. Liberti, Risoe National Lab., Report Risoe-M-2630, 1988, Tropospheric NO_x Chem.-Multiphase Aspects 61-7.

[17] R. Svensson, E. Ljungstrom and O. Lindquist, Atmospheric Environment 1987, 21, 1529; M. E. Jenkin, R. A. Cox and D: J. Williams, Atmospheric Environment 1988, 22, 487.

[18] Technical Documentation "Pigment Blacks", DEGUSSA, Anorganische Chemieprodukte, Postfach 110533, D-6000 Frankfurt 11, Germany.

[19] B. Heikes and A. M. Thompson, J. Geophys. Res. 1983, 10, 10883.

[20] A. W. Adamson, Physical Chemistry of Surfaces (third ed.), John Wiley & Sons, 1976.

[21] R. C. Bansal, J.-B. Donnet and F. Stoeckli, Active Carbon, ch. 2, Marcel Dekker Inc. 1988.

[22] M. S. Smith, A. R. Chughtai and D. M. Smith, " The Structure of Hexane Soot I: Spectroscopic Studies.", Applied Spectroscopy, 1985, 39, 143.

[23] J. O. Hirschfelder, Ch. F. Curtis and R. B. Bird, Molecular Theory of Gases and Liquids, John Wiley & Sons 1964.

[24] M. Frenklach and H. Wang, Twenty-Third Symposium (International) on Combustion, The Combustion Institute, 1991, 1559; P. Markatou, H. Wang and M. Frenklach, Comb. and Flame 1993, 93, 467.

[25] C. A. Sergides, J. A. Jassim, A. R. Chughtai and D. M. Smith, Appl. Spectroscopy 1987, 41, 482.

[26] L. Brouwer, M. J. Rossi and D. M. Golden, J. Phys. Chem. 1986, 90, 4599.

[27] A. R. Chughtai, W. F. Welch, Jr., M. S. Akhter and D. M. Smith, "A Spectroscopic Study of Gaseous Products of Soot-Oxides of Nitrogen/Water Reactions.", Applied Spectroscopy, 1990, 44, 294

[28] I. B. Svenningson, H.-C. Hansson, A. Wiedensohler, J. A. Ogren, K. J. Noone and A. Hallberg, Tellus 1992, 44B, 446.

[29] A. Petzold; R. Niessner, Mikrochim. Acta, 1995, 117, 215.

[30] J. Porstendörfer; G. Röbig; A. Ahmed, J. Aerosol Sci., 1979, 10, 21.

[31] Handbook of Chemistry and Physics, 68th edition, CRC Press, Boca Raton, Florida, 1987.

[32] D. D. Parrish; P. C. Murphy; D. L. Albritton and F. C. Fehsenfeld, Atmos. Environ., 1983, 17, 1365.

[33] M. Kalberer; K. Tabor; M. Ammann, Y. Parrat; E. Weingartner; D. Piguet; E. Rössler; D.T. Jost; A. Türler; H. W. Gäggeler and U. Baltensperger, J. Phys. Chem, 1996, 100 (accepted).

[34] L. F. Keyser; S. B. Moore; M.-T. Leu, J. Phys. Chem., 1991, 95, 5496.

[35] F. F. Fenter; F. Caloz and M. J. Rossi, J. Phys. Chem., 1996, 100, 1008.

Chapter Four - Uptake Experiments of NO_2 on Acetylene Soot and Subsequent HONO Formation

In the experiments on commercial samples of amorphous carbon it was relatively difficult to vary the sample mass. In fact, the commercial carbon was in the form of a fluffy powder consisting of more or less coarse particles. It was therefore difficult to disperse a small sample of 50mg of PRINTEX 60 evenly on a sample dish of 37mm diameter. For this reason, we looked for a new type of sample which we were able to disperse evenly on the whole sample dish. It turned out that the simplest way to achieve this was to directly deposit the soot homogeneously on the sample dish during combustion of acetylene using a burner. The results for NO_2 uptake and NO formation found using the acetylene samples were in quantitative agreement with the preceding experiments [1]. In addition, we discovered an interesting new feature which is the generation of gas phase HONO concomitant with the NO_2-amorphous carbon interaction.

The present Chapter is not an exhaustive study of the HONO formation as a product of the NO_2-carbon interaction. Rather it is a summary of the experiments conducted so far and a stimulating outlook for further investigation. As a consequence, no quantitative results are presented.

4.1 Introduction

Nitrous acid is an important atmospheric trace species whose chemistry remains largely uncharacterized [2], [3]. In the troposphere, and in particular near cities, HONO has been found to accumulate during the nighttime to reach levels as high as 8 ppb just before sunrise [2], [4], [5], [6]. The source of gaseous nitrous acid under these conditions is uncertain; the heterogeneous hydrolysis of nitrogen oxides such as NO_2 and N_2O_3 (from the association reaction of NO with NO_2) have been suggested as possible mechanisms [2], [7]. Because HONO is easily photolysed in sunlight, it may be responsible for a "pulse" of hydroxyl radicals at sunrise that sets off the diurnal oxidative chain reactions [8], [9]. In addition, nitrous acid is injected by aircraft into the atmosphere with other pollutants such as SO_2, NO_2, NO and HNO_3 as well as particulates such as sulfuric acid, carbonaceous aerosols and water-ice particles [10], [11]. The chemistry of wakes and plumes is complex; indeed, an understanding of homogeneous reactions, nucleation processes and heterogeneous reactivities is

required to assess the impact of aircraft emissions on the physical and chemical properties of the atmosphere [11].

In the condensed phase, nitrous acid is known to be an efficient oxidizer [12] and might react with other trace species once it is adsorbed onto or dissolved into atmospheric aerosols. Recent laboratory studies showed that HONO plays a crucial role in the formation of nitrosyl sulfuric acid (NSA) which on its behalf may be important in the activation of HCl into ClNO [13], [14].

4.1.1 Knudsen Cell Parameters, Sample Preparation and Characterization

The following experiments were carried out using a teflonated glass reactor of $1890cm^3$ total volume at ambient temperature. The sample dishes (50mm i.d.) of $19.6cm^2$ result in a sample collision frequency ω of $92s^{-1}$ for NO_2, $91s^{-1}$ for HONO and of $121s^{-1}$ for H_2O. The diameters of the escape apertures are 1, 4, 9 and 14 mm corresponding to k_e for NO_2 of 0.058, 0.9, 2.4 and $5.3s^{-1}$, respectively. Due to an improvement in the cell design, the volume of the sample compartment has been reduced to less than 1% of the total volume and therefore, no correction for the PV term had to be performed anymore.

The samples were produced by flame deposition of soot originating from an acetylene burner about an hour before measurement. A small flame serving to ignite the main burner was used without addition of oxygen resulting in a rich flame. Plane glass dishes of 5 cm diameter were used as sample support. They were weighed just before and directly after the deposition using an analytical balance (METTLER AE 240). This balance provides the sample weight with an accuracy of tenths of milligrams at a Tara of approximately 14g.

Soot from acetylene combustion is formed in the gas phase, leading to particles with mean diameters of about 20 to 30nm which adhere to each other to form branched chains [15].

In order to check the behavior of the carbon samples with respect to water vapor, H_2O uptake experiments were performed on activated samples. It is known that the reaction of ozone with carbon soot will add surface functionalities [16] on which subsequent adsorption of polar molecules (e.g. water) can take place.

In order to activate the carbon samples, they were exposed during three periods of one minute to an oxygen flow of 100 l per hour containing 5 % ozone. A simple test indicates the change of the sample behavior towards water: if a water

drop is placed on an untreated sample it will not infiltrate, showing hydrophobicity. After treatment the water drop will be able to wash particles off.

The specific surface of the samples was measured with the BET method yielding a value of $303m^2g^{-1}$. Compared to the commercial samples used in the preceding study, this value lies in the upper part of the range between 20 and $460m^2g^{-1}$ corresponding to FW2. Furthermore, a characteristic sample was observed under the electron microscope at an amplification of 50'000. The observed structure reveals that the particles are too small to be identified with this technique. Using atomic force microscopy on the other hand revealed that the samples were too soft to be used untreated. The deposition of a gold film on the samples and subsequent removal of the soot may permit in the future to visualize the sample structure by its "negative".

The gaseous nitric acid sample used in the complementary HNO_3 uptake study was prepared by distillation of a 65% solution in water according to Fenter [14]. The purity of the gas sample was routinely checked by measuring the ratio of the m/e30 to m/e46 signals. This allows the purity to be assessed before an experiment to eliminate possible secondary chemistry involving NO_2 (a potential degradation product) and to ensure that the m/e46 fragment is due uniquely to the presence of HNO_3 in the effusive beam. HNO_3 can be unambiguously monitored at m/e63, but the m/e46 signal is about a factor of 20 more intense, which allows experiments to be conducted with smaller flows of HNO_3 (for the same signal to noise ratio).

4.1.2 HONO Flow Calibration

In order to calibrate the HONO flow, HCl uptake experiments on $NaNO_2$ as shown in **Figure 4.1** have been performed. In the presented experiment a sample of 1.7g of $NaNO_2$ was exposed to an HCl flow of $1.3 \cdot 10^{16}$#/s. The uptake is large but 10 seconds after the start of exposure at t=180s, the sample begins to saturate. Using the small orifice (1mm i.d.), the saturation appears to takes place on a time scale corresponding to k_e=0.6s^{-1}. The HONO flow is calculated assuming 100% conversion of HCl into HONO at initial uptake.

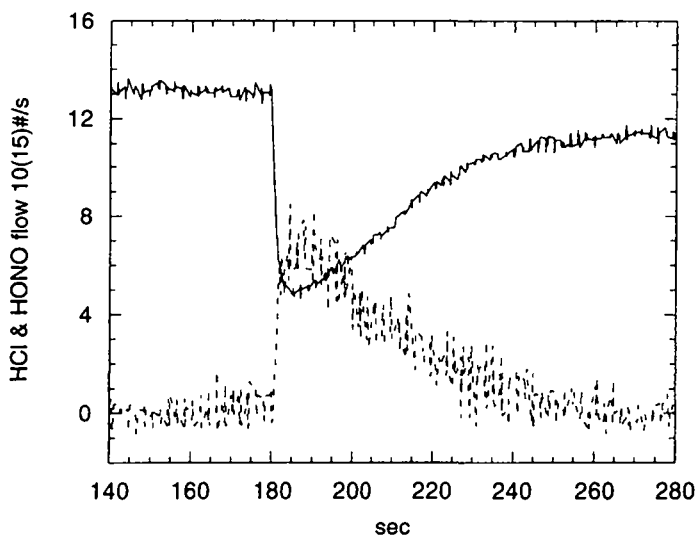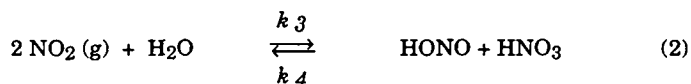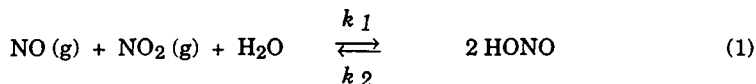**Figure 4.1:** HCl uptake on 1.7g of $NaNO_2$ for HONO calibration using the 1mm orifice. HCl flow equals $1.3 \cdot 10^{15}$#/s (solid line) while the HONO flow (dashed line) is estimated on a 100% conversion basis. The sample compartment was opened at t=180s. Experiment 3 of 7 February 1995.

4.1.3 Possible Reaction Schemes of the Heterogeneous HONO Formation

At the present stage we can only speculate about possible reaction schemes which will yield HONO under our experimental conditions. A recent compilation of kinetic data for the system nitrogen oxides in water was presented by Pires [17]. According to Schwartz and White [18], [19] the formation of HONO in an aqueous solution can proceed through the following reaction schemes:

$$NO\ (g)\ +\ NO_2\ (g)\ +\ H_2O \quad \overset{k_1}{\underset{k_2}{\rightleftharpoons}} \quad 2\ HONO \tag{1}$$

$$2\ NO_2\ (g)\ +\ H_2O \quad \overset{k_3}{\underset{k_4}{\rightleftharpoons}} \quad HONO + HNO_3 \tag{2}$$

The presence of gaseous NO and NO_2 in our system is ascertained in measurements by Thielmann [1]. However, it is less clear in which form water is present in or on the soot particles. The soot was prepared by combustion of acetylene at atmospheric pressure (ambient air) and direct deposition onto glass dishes. Water can either be incorporated into the soot particles as a combustion product or it can condense on the sample during the time period between sample preparation and putting the sample under vacuum.

4.2 Results

Figure 4.2 shows a typical experiment where HONO formation is observed on a fresh sample of acetylene soot using the large orifice reactor. At t=20s an NO_2 flow of $1.6\cdot10^{16}$#/s is installed. Upon opening of the sample compartment at t=80s, a peak rate of HONO formation is observed with a maximum flow of $4\cdot10^{15}$#/s. This flow decreases rapidly and tends asymptotically towards approximately $0.5\cdot10^{15}$#/s. From the experiments on commercial samples we know that black carbon contains water which can be removed simply by lamp heating. Knowing moreover that the HONO formation must be related to the presence of water, we used an incandescent lamp to enhance the water desorption from the sample. When the heat lamp is turned on at t=180s, we observe the HONO flow to increase instantaneously to $2.2\cdot10^{15}$#/s. From t=200s on the NO_2 flow is steadily increased from $1.6\cdot10^{16}$#/s to $5.5\cdot10^{16}$#/s. The subsequent formation of HONO increases proportionally to reach a flow of almost $6\cdot10^{15}$#/s. Shortly there after, at t=260s, the lamp is turned off and the flow decreases again rapidly to a level that is about three times as high as the one before heating. As soon as the NO_2 flow is turned off at t=320s the HONO formation ceases.
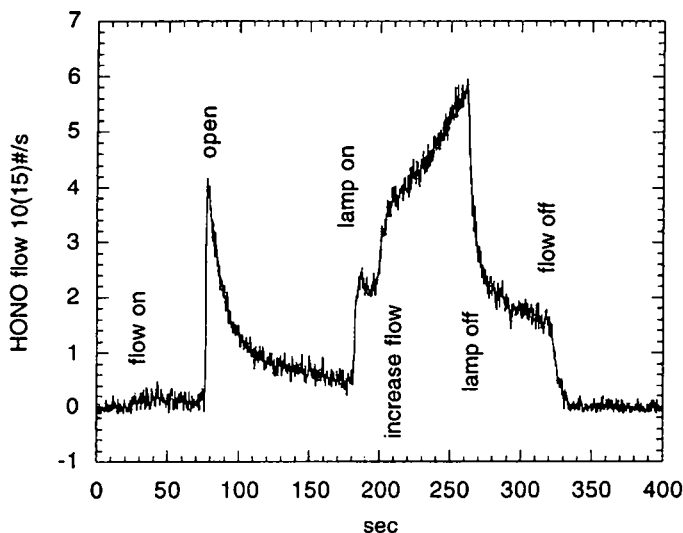

Figure 4.2: HONO formation monitored at m/e47 on fresh acetylene soot (4.1mg) using the 9mm orifice. Initial NO_2 flow of $1.6\cdot10^{16}$#/s is increased steadily from t=200s on. Experiment 8 of 6 February 1995.

Figure 4.3 a and b show the correlation of HONO formation and water desorption from the carbon sample under two different conditions. Two consecutive experiments were carried out on the same sample. In the first experiment we followed m/e18 in order to observe the water desorption from the sample and in the second experiment m/e47 corresponding to HONO formation was followed at a concurrent NO_2-flow of $6.9 \cdot 10^{16}$#/s. Note that the water flow is presented on a scale ten times larger than the HONO flow.
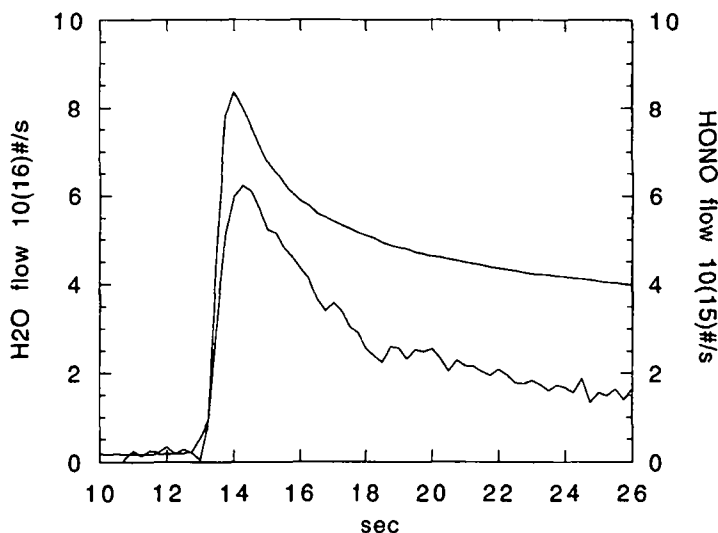

Figure 4.3 a: Correlation of HONO formation and water desorption upon opening of sample compartment. Upper trace corresponds to water desorption (left hand ordinate) using 15mm orifice, and lower trace shows HONO formation (right hand ordinate) using 4mm orifice. NO_2 flow of $6.9 \cdot 10^{16}$#/s on fresh acetylene soot sample (3.1mg). Experiment 4&5 of 7 September 1995.

Figure 4.3 a corresponding to the first part of each experiment shows the two traces upon opening of the sample compartment. In both traces we observe a transient peak which decays rapidly and tends asymptotically towards $1.5 \cdot 10^{15}$#/s HONO flow and $4.0 \cdot 10^{16}$#/s water flow respectively. In the case of water, the opening of the sample compartment corresponds to pumping off the water from the sample. In the HONO case, this opening corresponds to starting the NO_2 interaction with the sample.

Figure 4.3 b presents the same traces but at a later time (sample compartment still open and NO_2-flow in the reactive case) when the heat lamp is

turned on at t=5s and t=7s, respectively. A relative time scale with a delay of 2s is chosen for the sake of presentation. In both experiments the observed traces increase instantaneously and drop subsequently to a relatively stable level. In particular, the water signal increases from about $1.55 \cdot 10^{16}$#/s to $1.75 \cdot 10^{16}$#/s upon heating while the HONO signal increases almost by a factor of 6 from $0.4 \cdot 10^{15}$#/s to $2.3 \cdot 10^{15}$#/s.
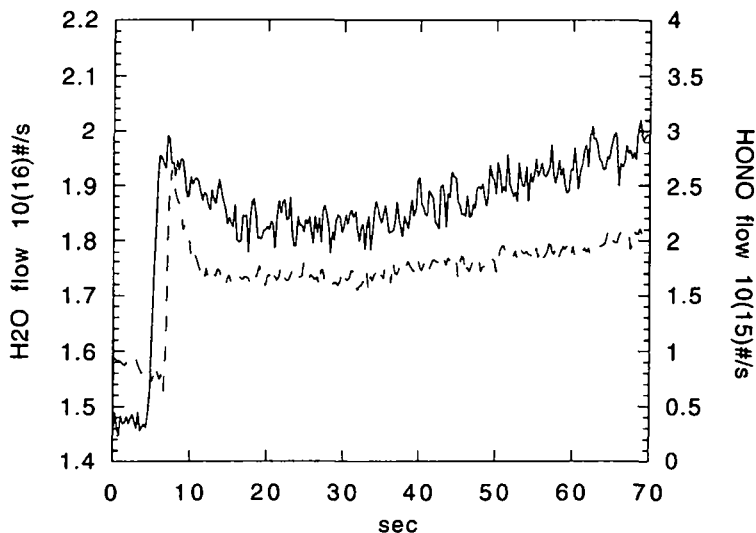

Figure 4.3 b: Correlation of HONO formation and water desorption when heat lamp is turned on. Lower trace corresponds to water desorption (left hand ordinate) using 15mm orifice and upper trace to HONO formation (right hand ordinate) using 4mm orifice. The heat lamp is turned on at t=5s (HONO) and t=7s (H_2O) respectively. NO_2 flow of $6.9 \cdot 10^{16}$#/s on fresh acetylene soot sample (3.1mg). Experiment 4&5 of 7 September 1995.

In order to check the behaviour of carbon samples with respect to the uptake of water vapor, experiments were performed on activated (ozonized) samples. **Figure 4.3** shows an NO_2 uptake experiment on a ozonized carbon sample where we checked the influence of an external water flow of $7.6 \cdot 10^{15}$#/s. While exposed to an NO_2 flow of $1.5 \cdot 10^{16}$#/s, the sample was heated by irradiation from t=180s on. As on the non ozonized sample, the HONO formation increases upon heating. At t=420s and at t=480s respectively, the water flow was turned on and off, but no change in signal is observed. Contrary to our expectation, the HONO

signal increases after the water flow is turned off which may suggest that the external water flow is inhibiting HONO formation under certain circumstances.

Prior to the displayed experiment, 4 standard NO_2 uptake experiment had been performed on the same ozonized sample. Therefore, we can assume that some of the water had been pumped off so that the sample is dryer than a new sample. For this reason the HONO formation is less pronounced than in the experiments using a fresh sample.

Note that although the ozonized sample was hydrophilic, no interaction with water could be observed under our experimental conditions, that is in the water pressure range of a few mTorr.
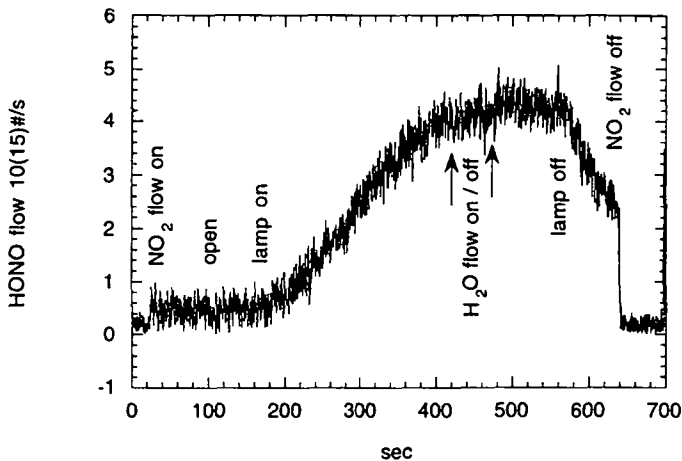

Figure 4.4: Influence of an external water flow using the 15mm orifice. At t=420s when the effect of the heat lamp reaches saturation with respect to HONO formation, an external water flow of $7.6 \cdot 10^{15}$#/s is established but no increase of HONO formation is observed. NO_2 flow of $1.5 \cdot 10^{16}$#/s on ozonized soot sample (8.4mg). Prior to this experiment 4 standard NO_2 uptake experiments had been performed on the same sample. Experiment 6 of 31 January 1995.

Figure 4.5 shows the formation of HONO on an aged sample which was regenerated by exposure to ozone. We refer to an aged sample as a sample on which various NO_2 uptake experiments have been performed and the water has been pumped off prior to regeneration. Although an ozonized sample did not show any interaction with water under our experimental conditions, we might expect that a sample previously treated by exposure to ozone and kept at ambient pressure during a few hours, could readsorb water and thus be

recharged. While heating the sample since t=50s, the NO_2 flow was increased from t=380s on till saturation with respect to HONO formation (m/e47) was reached at about t=400s. Shortly thereafter, the HONO rate of formation of $12.5 \cdot 10^{15}$#/s starts to decrease while maintaining the large flow of NO_2. At t=440s the lamp was turned off and consequently the HONO formation drops by a factor of 5. At t=710s the heat lamp was turned on again in order to check if the HONO formation could be stimulated. However, we observe only a small increase of the HONO flow which is not increased further by admission of an external water flow, as expected. At t=910s the reactor orifice was changed from 9mm to 1mm diameter which at steady state conditions corresponds to a higher partial pressure of the species present. As a consequence of this change in pressure regime, the HONO formation is slightly increased again.

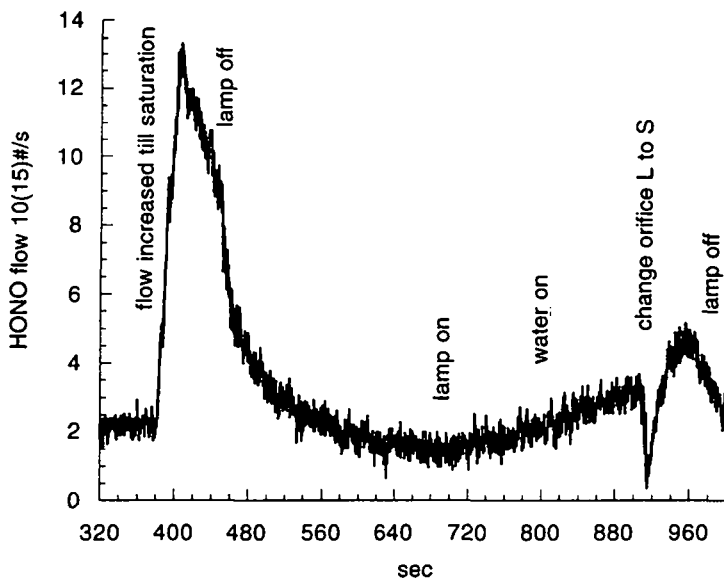**Figure 4.5:** HONO formation on aged sample (5.4mg) regenerated by ozone. Initial NO_2 flow of $4.8 \cdot 10^{14}$#/s and water flow of $7.2 \cdot 10^{16}$#/s. Orifice was changed from 9mm (L) to 1mm (S) at t=910s. Experiment 9 of 31 January 1995.

4.2.1 Uptake of Nitric Acid on Carbon

Experiments were performed to assess the affinity of nitric acid to carbon in order to check the role that nitric acid might play in the mechanism leading to HONO formation. The upper part of **Figure 4.6 a** corresponding to the left hand ordinate shows a HNO_3 uptake experiment on acetylene soot. The two masses at m/e30 (lower trace) and m/e46 (upper trace) are detected alternatively during 5 seconds each. Due to this instrumental artifact, the traces appear digitized and are subject to transient peaks. The established HNO_3 flow is initially set at $12.5 \cdot 10^{15}$#/s but decreases slightly between t=400 and 800s because of the difficulty of establishing a constant source of HNO_3 [14]. The sample compartment is opened at t=430s. We immediately observe an uptake of HNO_3 at almost 100%. While the sample becomes saturated, the uptake decreases to
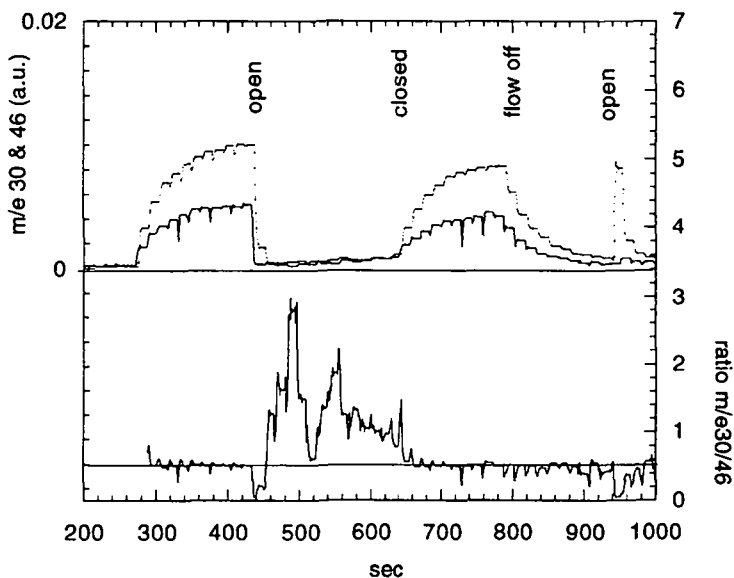
Figure 4.6 a: Upper part (left hand ordinate): HNO_3 uptake on 4.2mg acetylene soot with initial flow of $12.5 \cdot 10^{15}$#/s. m/e30 (lower trace, straight line) and m/e46 (upper trace, dashed line) are detected alternatively during 5 seconds each. Escape orifice is switched from 1mm to 15mm diameter before reopening the sample compartment at t=940s. Lower part (right hand ordinate): ratio of m/e30 to m/e46 for the same experiment. For pure HNO_3 flow this ratio equals 0.5 (line). Higher values correspond to additional gas phase NO and NO_2. Experiment 4 of 24 February 1995.

approximately 90% at t=640s when the compartment is closed. At t=790s the
HNO3 flow is turned off. In order to have a higher pumping speed while
observing the desorption, the orifice plate was switched from the 1mm to the
15mm diameter orifice before reopening of the sample compartment at t=940s.
The desorbing gas has a dominant contribution at m/e46 but can not be
attributed unambiguously to HNO3 due to the sampling artifact (see discussion
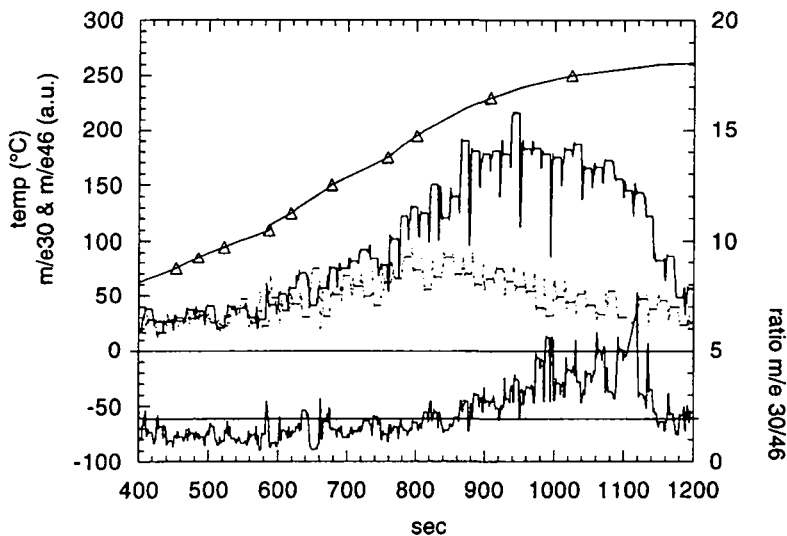of the lower part of the same Figure).

Figure 4.6 b: Upper part (left hand ordinate): heat ramp on carbon
sample (4.2mg) after adsorption of $2.2 \cdot 10^{18}$ molecules of HNO3.
Detecting gas phase products: m/e30 (upper trace, straight line) and
m/e46 (lower trace, dashed line) are detected alternatively during 5
seconds each. The line with triangles (left hand ordinate) corresponds
to the temperature of the heat support In the displayed time period the
sample is heated from 60 to 260°C. Lower part (right hand ordinate):
ratio of m/e30 to m/e46 for the same experiment. For pure NO2 flow
this ratio is about 2 (line). Higher values correspond to NO production.
Experiment 6 of 24 February 1995.

The lower part of **Figure 4.6 a** corresponding to the right hand ordinate shows
the ratio of m/e30 to m/e46 for the same experiment. When the HNO3 flow is in
the process of stabilizing this ratio takes on a value of 0.5 corresponding to a
HNO3 sample with less than 1% NO2 impurities measured by LIF [20]. As soon
as the sample compartment is opened we observe an increase of the ratio due to
gas phase products. Knowing that NO2 has a mass spectrometric signature
corresponding to ratio m/e30 to m/e46 of about 2 (see Figure 3.1), we can assume

mainly NO_2 is formed at first. As the ratio decreases at a later stage, the gas phase must correspond to a mixture of HNO_3, NO_2 and NO.

Upon reopening of the sample compartment at t=940s a ratio approaching 0 is observed corresponding to a very large transient of the signal at m/e46. As the desorption is fast compared to the sampling period of 2s per mass, this transient may be due to a sampling artifact.

The upper part of **Figure 4.6 b** corresponding to the left hand ordinate shows an experiment where the sample previously exposed to HNO_3 is heated to 260°C using a newly designed heat support [21]. As in the preceding Figure the two masses at m/e30 (lower trace) and m/e46 (upper trace) are detected alternatively during 5 seconds each. In addition, the temperature ramp applied to the sample is displayed on the same ordinate. In the desorption process presented in this Figure, it is the signal at m/e30 that assumes a higher amplitude than the one at m/e46 which may be clearly seen beginning at t=800s. At about t=600s corresponding to a temperature of 120°C the signals start to increase from their background levels until they reach their respective maxima at t=800s (m/e46) and t=1000s (m/e30).

The lower part of **Figure 4.6 b** corresponding to the right hand ordinate shows the ratio of m/e30 to m/e46 for the same experiment. Before heating this ratio has a value of about 1 corresponding to background level of the detected signals. Even when the signals start to evolve at t=600s the ratio remains below 2 which may be interpreted as concurrent NO_2-HNO_3 desorption. Between t=850s and t=1100s the ratio increases to about 4±1 indicating increased NO formation.

4.3 Discussion

The present uptake experiments of NO_2 on acetylene soot are accompanied by the formation of NO and HONO. Contrary to the detection of NO_3/N_2O_5 as trace products of the NO_2 interaction with the commercial samples (see Chapter 3), NO and HONO are the only gas phase products and they seem to be generated in very different ways. As seen in the preceding Chapter, the NO formation decreases while the sample becomes saturated by uptake of NO_2. This process is described by sample aging. In the present case, however, the HONO formation does not seem to depend on the sample aging due to uptake of NO_2, but it is strongly dependent on the amount of water desorbing from the sample.

Moreover, it is dependent on the NO_2 partial pressure, i.e. the flowrate of NO_2 or the orifice size.

Although the HONO formation is strongly correlated to the water signal as seen in Figure 4.3, the experiment in Figure 4.4 shows that it is not enhanced by an external water flow. This means that it is not gas phase water that is involved in the HONO formation but water that is located in the pores or elsewhere on the carbon surface and which has been called "tightly bound" H_2O in the literature. HONO formation is therefore a heterogeneous process which takes place at the carbon-water interface [22].

Heating a sample that was previously exposed to NO_2 does not show HONO formation which means that a sample containing traces of adsorbed NO_2 and water can not produce any HONO upon evaporation of water. A concurrent NO_2 flow is needed. Moreover, it may be shown that no HONO is formed upon heating a sample without exposure to NO_2. Therefore, we exclude the possibility that HONO is generated during combustion/sample preparation.

The experiment presented in Figure 4.5 shows that a previously used and heated sample can be recharged with water from ambient air. However, in the mTorr range of H_2O vapor corresponding to the molecular flow regime in our apparatus, water uptake experiments on ozonized samples have not shown any affinity for water vapor. The total HONO production in this experiment is estimated to be approximately $2 \cdot 10^{18}$ molecules which is more than the amount of HONO formed in experiment displayed in Figure 4.3 ($4 \cdot 10^{17}$ molecules), which, however, was a relatively dry sample due to the preceding water desorption experiment. No systematic experiments have been performed so far which would allow one to determine the quantity of HONO that can be formed on a fresh sample. The presented experiment shows, however, that this quantity is limited due perhaps to a finite reservoir of water in the carbon sample.

4.3.1 Which is the Pathway to HONO Formation?

From the experiments conducted on commercial samples (see preceding chapter), we know that the more the sample becomes saturated by uptake of NO_2 and the more surface sites are consumed, the smaller is the production of gas phase NO. Moreover, we know from the mass balance that a considerable amount of NO or NO_2 remains somewhere on the surface of some of the commercial samples. As HONO production of similar amount can be observed on a fresh as well as on a saturated sample on which the gas phase formation of NO is very different, we conclude that the availability of gas phase NO is not the

limiting factor for HONO production. Therefore, if NO is involved as suggested by reaction (1), it must be located either on the carbon surface, in water droplets or on a NO precursor (see mechanism for NO_2 adsorption on carbon presented in Chapter 3.3). As the Henry constant of NO with respect to liquid water is small [23], it is most likely that the potentially reactive NO is located at the water-carbon interface or that the formation only proceeds through reaction (2) which involves HNO_3.

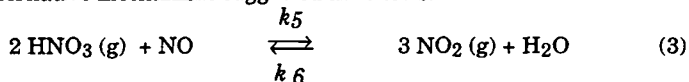During HONO formation, the presence of other trace gases like N_2O_5 and HNO_3 was checked, but no significant contribution to the respective masses at m/e62 and 63 could ever be detected. This suggests that the HONO formation mechanism cannot involve N_2O_5 or HNO_3 as far as the gas phase is concerned. The fact that no gaseous HNO_3 was detected can be explained by the strong affinity of nitric acid on carbon as summarized below.

The HNO_3 uptake experiments presented in Figure 4.6 a shows that nitric acid is very sticky on carbon corresponding to a γ approaching unity. Moreover, this uptake is accompanied by conversion of HNO_3 into NO_2 which can either be explained by HNO_3 decomposition into water and oxygen according to:

$$HNO_3 \longrightarrow NO_2 + 1/2\ H_2O + 1/4\ O_2$$
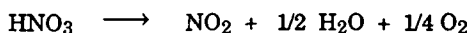
or by the alternative mechanism suggested as follows:

$$2\ HNO_3\ (g) + NO \underset{k_6}{\overset{k_5}{\rightleftharpoons}} 3\ NO_2\ (g) + H_2O \qquad (3)$$

In such a case, the NO-precursor would be present due to a preceding NO_2 uptake experiment.

In a heat ramp experiment not presented here in detail in which m/e47and m/e63 were followed, neither desorption of nitric acid nor HONO formation could be observed. This means that HNO_3 either remains strongly adsorbed on carbon or is rapidly converted into gas phase products as shown by Figure 4.6 b.

4.4 Conclusion

The observed HONO formation is strongly dependent on the instantaneous water desorption from the sample as well as on the NO_2 partial pressure in the reactor. On the other hand, it is not enhanced by an external water flow which did not show any interaction with the carbon sample. However, as no correlation

between HONO formation and NO partial pressure has been observed so far, we suggest a reaction mechanism that only involves NO_2 and H_2O but no NO:

$$2 \, NO_2 \, (g) + H_2O \quad <=> \quad HONO + HNO_3$$
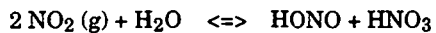
Furthermore, we have observed that HNO_3 is very sticky on carbon, and upon heating, it is either converted into NO_2 or does not desorb.

4.5 References

[1] Thielmann, A.; report in the frame of a diploma thesis, 1995.

[2] Calvert, J.G.; Yarwood, G.; Dunker,A.M., Res. Chem. Intermed. 1994, 20, 463

[3] Platt, U., Nato ASI Series, Chemistry of Multiphase Atmospheric Systems, Springer Verlag, 1986.

[4] Platt, U.; Perner,D.; Harris,G.W.; Winer,A.M.; Pitts, J.N. Jr., Nature 1980, 285, 312.

[5] Perner, D.; Platt,U., Geophys. Res. Lett. 1979, 6, 917.

[6] Harrison, R.M.; Kitto,A.-M. N., Atmos. Environment 1994, 28, 1089.

[7] Jenkin, M.E.; Cox, R.A.; Williams, D.J., Atmos. Environment 1988, 22, 487

[8] Harris, G.W.; Carter, W.P.L.; Winer, A.M.; Pitts, J.N., Environ. Sci. Technology 1982, 16, 414.

[9] Salawitch, R.J. et al., Geophys. Res. Lett. 1994, 21, 2251.

[10] Arnold, F.; Scheid, J.; Stilp,Th., Geophys. Res. Lett., 1992,12, 2421.

[11] AERONOX, The Impact of NOx Emissions from Aircraft Upon the Atmosphere at Flight Altitudes 8-15km, editor: U. Schumann, EC-DLR Publication on Research related to Aeronautics and Environment,1995.

[12] Rodrigues Pires, M.J.; van den Bergh, H.; Rossi, M.J., submitted to J. Atm. Chem.

[13] Zhang, R.; Leu, M.-T.; Keyser, L.F., 1996, 100, 339.

[14] Fenter, F.F.; Caloz, F.; Rossi, M.J., J. Phys. Chem. 1994, 98, 9801

[15] Goldberg, E. D.: Black Carbon in the Environment, New York 1985; John Wiley & Sons

[16] Smith, D. M. and Chughtai, A. R.: Reaction Kinetics of Ozone at Low
      Concentrations with n-Hexane Soot, submitted to Journal of Geophysical
      Research.

[17] Rodrigues Pires, M.J.; van den Bergh, H.,; Rossi, M.J., submitted to Int. J.
      Chem. Kin.

[18] Schwartz, S.E., White, W.H. Kinetics of Reactive Dissolution of Nitrogen
      Oxides into Aqueous Solution, Wiley Interscience, New York, 1983, 12, 1.

[19] Schwartz, S.E., White, W.H. Solubility Equilibria of Nitrogen Oxides
      and Oxyacids in Dilute Aqueous Solutions, Gordon and Breach Sci.
      Pub., 1981, 4, 1.

[20] Fenter, F.F.; Caloz, F. and Rossi, M.J., Atmos. Environ., 1995, 29, 3365.

[21] Fenter, F.F.; Caloz, F.; Tabor, K.; Gutzwiller, L.S. and Rossi, M.J., in
      preparation.

[22] Mertes, S. and Wahner, A., J. Phys. Chem., 1995, 99, 14000.

[23] J.N. Armor, J. Chem . Eng. Data, 1974, 19, 28.

Chapter Five - Kinetics of Condensation and Evaporation of Water on Ice Surfaces between 160 and 220K

5.1 Introduction

The kinetics of condensation and evaporation of H_2O vapor on both liquid water and solid ice has been studied for many years [1], [2], [3]. Interest in this topic is fostered by its significance in understanding how processes such as cloud formation and growth occur in the atmosphere [4]. The condensation and evaporation coefficients of H_2O on ice have met with increasing interest since recent atmospheric studies have revealed the role of heterogeneous chemistry on ice particles [5], [6], [7], [8], [9]. In particular, the ozone hole over Antarctica in the austral spring is intimately linked to the presence of ice particles known as polar stratospheric clouds [10], [11]. Furthermore, the condensation of water vapor also plays an important role in the chemistry occurring in aircraft contrails, especially at high cruise altitude (8 to 15km) [12]. That ice crystals in contrails would grow was recognized by Appleman [13] and others in early contrail studies. The growth of contrails leading to large ice crystals and ice water content orders of magnitude greater than that due to the water supplied by the aircraft exhaust presents an additional element in the current argument over whether air traffic increases or decreases the abundance of water at subtropopause levels. At these altitudes, fairly large ice crystals will fall thousands of meters before evaporating. Given sufficient probability for conditions of such growth, the overall effect of subtropopause jet traffic may in fact be to lower the water abundance in this region of the atmosphere through the precipitation of existing moisture to much lower levels [12], [14]. The ice surface also plays a role in the icing of materials on earth, and its interplay with crystalline point defects may be involved in the generation and interparticle transfer of charge that ultimately leads to electrical displays in storms [15]. In glaciology, the transformation of snow into ice plays a pivotal role. In this process ice crystals grow by sublimation while the air spaces between them are eliminated. Air is thus incorporated into the crystal lattice and forms clathrates [16].

The possible influence of trace chemicals on the growth of ice crystals has been studied theoretically by Crutzen and coworkers [17] in the temperature range from -40 to 0°C. Their concept is such that the solute forms a transition layer on the ice surface. This layer alters the equilibrium vapor pressure and thus affects the evaporation of ice particles.

The growth of liquid water aerosols has been reviewed by Mozurkewich [18]. From a theoretical point of view he concludes that the temperature dependent growth rate of water aerosol particles may be understood in terms of two separate accommodation mechanisms, namely mass and energy accommodation described by the condensation and thermal accommodation coefficient, respectively. The present Chapter is only concerned with H_2O mass accommodation .

Detailed modeling of the heterogeneous chemistry in the stratosphere is dependent on the knowledge of accurate condensation and evaporation coefficients. Unfortunately, experimentally derived values of the condensation coefficient on ice range from approximately $\gamma = 0.01$ to $\gamma = 1.0$. This considerable range of values can be attributed to the numerous factors such as differing experimental techniques, experimental parameters and theoretical assumptions that have been employed in the various studies. The temperature of H_2O vapor and of the ice surface may also be very important, although no single study has established the dependence of the condensation coefficient on these parameters.

A detailed review of the existing literature has been given by George [19] and Marti [20]. Early examinations of liquid water and solid ice surfaces focused on the evaporation of H_2O molecules and assumed that the condensation coefficient was equivalent to the evaporation coefficient. However, this assumption of equality between condensation and evaporation coefficients has often been questioned. A number of investigators have also measured the interfacial heat transfer resistance of condensing H_2O vapor at the liquid water surface. All these experiments have been performed at surface temperatures where H_2O evaporation could not be neglected. Therefore, the determination of the condensation coefficient again required the assumption that condensation and evaporation coefficients were equivalent. Techniques were developed more recently to measure condensation coefficients directly. Values for γ from these direct measurements vary from $\gamma = 0.026$ to $\gamma = 1.0$. A number of studies have utilized gravimetric methods to determine growth rates at an ice surface at known H_2O vapor pressure. Additional experiments have pictographically measured the growth rates of ice crystals and water droplets [21], [22]. Other techniques based on vapor pressure variation in a closed system, on a fast flow reactor, on optical interference and Fourier Transform Infrared absorption spectroscopy have also been used to measure γ [23]. George and coworkers measured the condensation coefficient which decreased with increasing temperature consistent with a precursor mediated adsorption mechanism [24]. Moreover, these authors observed adsorption and desorption rates of 10-1000 H_2O monolayers (ML) per second over the stratospheric temperature range from

180 to 210K at equilibrium conditions. The ice surface has been found to be very dynamic and rapid solvation by impinging H_2O molecules may occur on a millisecond time scale. As a result, heterogeneous atmospheric reactions may involve several monolayers of the interface rather than imply a static ice surface where just the first layer of H_2O molecules partake in the interfacial reaction.

In this Chapter, we report on the condensation and evaporation rate constants of H_2O, using a simple condensation-evaporation mechanism for interpreting the steady-state flow experiments. In addition, the steady-state conditions were perturbed by an injected burst of H_2O molecules, and the relaxation of the H_2O partial pressure in the Knudsen reactor was followed using real-time mass spectrometry capable to follow exponential decays up to $60s^{-1}$.

5.1.1 Knudsen Cell Parameters, Sample Preparation and Experimental Protocol

The present investigation has been carried out using two different designs of Knudsen cells, each one characterized by its volume, and two different low temperature supports characterized by their sample surface. The four different combinations of Knudsen reactors together with their corresponding k_e are displayed in **Table 5.1**. Most of the experiments were carried out using Knudsen cell #2 together with LTS #1. The latest experiments however were performed using the Teflon coated Knudsen cell #3, using both LTS #1 and #2.

Experiments on two different types of ice samples were carried out. The first type of ice sample referred to as bulk consisted of about 3 ml of deionized water that was poured into the sample dish after which the LTS was mounted on the Knudsen reactor. The sample was then subject to at least one freeze-pump-thaw cycle at the background pressure of the Knudsen reactor. For the preparation of the second type of sample, a flow of at least 10^{18} water molecules s^{-1} was condensed onto the sample dish at a temperature just above the one necessary for growth of porous ice (135 to 160K) during which the Knudsen cell was isolated from the high vacuum system. In anticipation of the experimental results, no significant dependence of the kinetics on the sample type could be observed.

Table 5.1: Experimental Parameters for Combinations of various Knudsen Cell Reactors (Cell) with different Low Temperature Supports (LTS) and an Optical Attachment (opt. at.).

reactor combination	k_e for L (s^{-1})	k_e for S (s^{-1})	Vo-lume (cm^3)	Area (cm^2)	surf. to volume ratio	normal. factor [a]	ω (s^{-1}) at 340K
1 Cell #2 LTS #1	7.5	1.0	1180	11.3	0.0096	1	152
2 Cell #2 LTS #1 + opt. at.	7.0	0.8	1280	11.3	0.0088	0.92	140
3 Cell #3 LTS #1	3.8	0.51	1830	11.3	0.0062	0.64	97
4 Cell #3 LTS #2 Tefl coat.	8.55	0.85	1830	15.2	0.0083	0.87	132

[a] with respect to reactor combination 1.

The steady-state experiment for this system are carried out with the sample compartment "open" allowing the water molecules to evaporate from the ice and effuse through the orifice. The water flow emanating from the ice surface is measured using two different orifices at various sample temperatures in the range $160K \leq T \leq 220K$. After measurement of the H_2O signal for two orifices of the Knudsen reactor the sample compartment was closed in order to perform a background measurement of water vapor leaving the Knudsen reactor. This is especially important at low temperatures where the net rate of H_2O outflow due to evaporation is approaching the background flow. A variation of this mode of operation is to add an external flow of H_2O vapor into the cell in addition to evaporation; this mode is called a "source term experiment" which has been performed on a regular basis in order to complement evaporation experiments.

5.2 Results and Discussion of the Steady-State Experiments

In the steady-state experiments, the steady-state flows out of the reactor were measured as a function of temperature for at least two orifice sizes, large (L) and small (S). The primary goal of taking pairs of data points corresponding to two orifice sizes is to separate the two kinetic parameters k_c and R_{ev} represented in Scheme I. The interpretation of the experiments follows a simple two-state scheme in which the gas phase species G (=H_2O in the vapor phase) interacts with its condensed bulk state B (H_2O ice):

$$\text{MS-detection} \quad \overset{k_e}{\longleftarrow} \quad G \quad \overset{k_c}{\underset{R_{ev}}{\rightleftharpoons}} \quad B$$
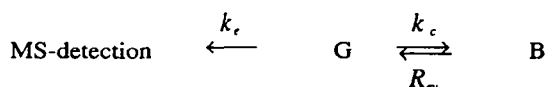
Scheme 1

k_e and k_c are unimolecular rate constants for effusion and condensation, respectively, and R_{ev} is the rate of evaporation of H_2O vapor originating from the sample. For such a mechanism, the gas-phase concentration in the LPR is given by the balance of the source term (rate of evaporation R_{ev}) and the loss terms (rate of effusion through the reactor orifice and the rate of condensation). Detailed balancing leads to the following equation, where [G] is the H_2O vapor phase concentration:

$$d[G]/dt = -k_e\ [G]\ -k_c\ [G]\ +R_{ev} \tag{1}$$

After multiplication by the volume, equation (1) can be written for steady state conditions as:

$$dG/dt = -F^0\ -k_c\ G + F_{ev} = 0 \tag{2}$$

where $G = [G]\ V = G_{ss}$ is the total number of gas phase molecules in the reactor at steady state conditions, and $F^0 = k_e\ [G]\ V$ is the flow of water vapor leaving the Knudsen reactor in molecules s^{-1} which is proportional to the observed MS signal at m/e 18. Equation 2 for steady state conditions leads to:

$$F_{ev} = F^0(1+\frac{k_c}{k_e}) \quad (3) \quad \text{and} \quad G_{eq} = G_{ss}(1+\frac{k_e}{k_c}) \tag{4}$$

Using two independent data sets corresponding to experiments in the large (L) and small (S) aperture Knudsen reactor allows for the determination of the unknown constants k_c and F_{ev} .

$$k_c = \frac{k_e^L \, k_e^S (r^{1/s} - 1)}{k_e^L - k_e^S \, r^{1/s}} \qquad (5) \quad \text{and} \qquad F_{ev} = F^L \frac{k_e^L - k_e^S}{k_e^L - k_e^S \, r^{1/s}} \qquad (6)$$

where $\quad r^{1/s} = \dfrac{F^L}{F^S} \quad$ is the ratio of the effusive flows of the large and small orifice reactor (F^L, F^S), respectively. The equilibrium vapor pressure can now be calculated as: $\quad \dfrac{G_{eq}}{V} = [G]_{eq} = \dfrac{F_{ev}}{Vk_c} = \dfrac{R_{ev}}{k_c} \quad$ according to Scheme 1.

We note that $\quad r^{1/s} = \dfrac{k_e^L}{k_e^S} * \dfrac{k_e^S + k_c}{k_e^L + k_c} \qquad$ and therefore $\qquad 1 \le r^{1/s} \le \dfrac{k_e^L}{k_e^S} \qquad (7)$

In equation (7), the left hand limiting case is obtained for a value of k_c much smaller than k_e^S , whereas the right hand limit is attained when k_c is much larger than k_e^L. As k_c measured over the whole temperature range was an order of magnitude higher than k_e^L, the experimental situation approached the latter case.

The symbols in **Figure 5.1** show the calculated vapor pressures measured in two different experiments. In the range 165 to 220K our measurements are in good agreement with the reference data of Jancso et al. [28]. In that study, however, the vapor pressure was measured only down to 195K and vapor pressures for lower temperature were given by extrapolation. Mauersberger and coworkers [20] have measured the vapor pressure down to 173K and found slightly lower values in this temperature range which agree better with Wexler's predictions [29]. As the primary goal of this work is to measure the adsorption and desorption kinetics, the satisfactory agreement between our vapor pressure and the one from Jancso gives us confidence in our experimental technique. The low temperature limit of our experiment is approximately 165K where the signal to noise ratio limits our ability to determine a reliable value for $r^{L/S}$. The present detection limit for H_2O effusing out of the Knudsen reactor is about 10^{14} molecules per second (#/s), and the situation is unchanged even when one performs experiments using an external flow of water. The upper limit of the investigated temperature range is given by the Knudsen condition with the constraint that the mean free path of water vapor must be at least a factor of 3

larger than the small orifice diameter (3 mm for reactor combination 1). Moreover, the calculated equilibrium vapor pressure did not depend on the sample preparation (bulk sample versus condensation from the vapor phase).
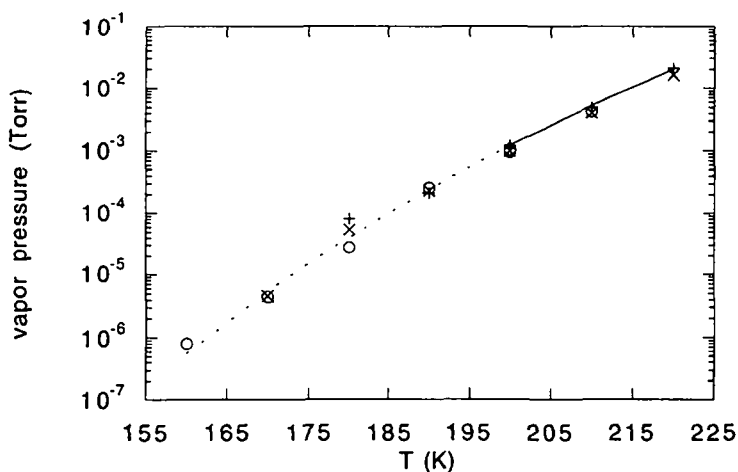

Figure 5.1: Vapor pressures measured in three different experiments (o, +, x). The measured reference data of Jancso et al. **[23]** are plotted as a solid line, the extrapolation is displayed as a dashed line.

Figures 5.2 and 5.3 are Arrhenius plots of k_c and F_{ev} calculated according to equations 5 and 6. The different symbols correspond to various experiments and to two types of sample (condensed and bulk sample). Figure 5.2 reveals a negative temperature dependence where k_c decreased by a factor of 5 when going from 180 to 220K. It corresponds to a negative activation energy of -3.1±1.5 kcal/mol in the interval of 180 to 220K implying the incidence of a complex condensation mechanism as opposed to the simple model given in Scheme 1. The range between 180 and 160K does not seem to show a clear temperature dependence suggesting a near independence of k_c with temperature. We suggest a negative activation energy of -1.6 ± 1.5 kcal/mol for this interval. In fact, the determination of k_c becomes more difficult at lower temperatures because $r^{L/S}$ tends towards $\dfrac{k_e^L}{k_e^S}$ which leads to a vanishing denominator resulting from the difference of two large numbers in equation 5. This may be the reason for near T-independent values of k_c . For F_{ev} this behaviour is less pronounced

because F_{ev} scales linearly with one of the measured steady state flows, assuming that the ratio $r^{L/S}$ is practically constant and approaching $\dfrac{k_e^L}{k_e^S}$.
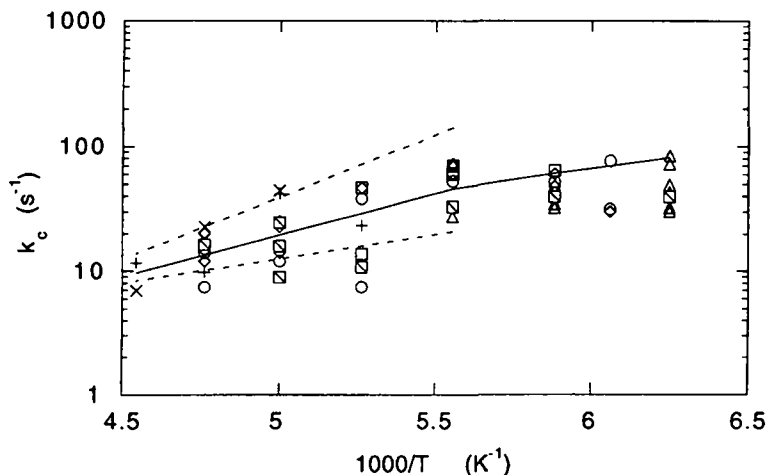

Figure 5.2: Arrhenius plot of k_c. The different symbols correspond to various experiments and two types of sample (condensed and bulk sample). The data are normalized to ω=152 s^{-1} (reactor combination 1, Table 5.1). The solid line corresponds to a negative activation energy of -3.1±1.5 kcal/mol and to -1.6±1.5 kcal/mol in the range 180 to 220K and 160 to 180K, respectively.

In the investigated temperature range of 160 to 220K, the rate of evaporation F_{ev} varies by 2 to 3 orders of magnitude, i.e. from about $1 \cdot 10^{16}$ to $200 \cdot 10^{16}$ molecules evaporating from the total sample surface (11.3 cm^2) per second. One monolayer of water in bulk ice corresponds to approximately 10^{16} molecules taking into account the total sample surface. The number of H_2O molecules in one monolayer of ice may be calculated in the following way: a cube of 1 cm^3 of ice contains approximately 1 g of water or $1/18 \cdot 6.03 \cdot 10^{23}$ H_2O molecules corresponding to a surface density of $[1/18 \cdot 6.03 \cdot 10^{23}]^{2/3}$ #/cm^2; by multiplying this density with the geometrical surface area of the sample (11.3 cm^2) we obtain a total number of $1.1 \cdot 10^{16}$ molecules forming a nominal monolayer of H_2O on the ice surface. In this derivation the variation of the density of ice as a function of temperature has been assumed to be negligible with respect to other experimental uncertainties. This means that the surface becomes increasingly dynamic at higher temperatures, and at 180K already 10

monolayers of H_2O evaporate per second. The activation energy for F_{ev} in the range 180 to 220K is 7.0±2.0 kcal/mol and in the range 160 to 180K, an activation energy of 10.0±2.0 kcal/mol is consistent with the data.
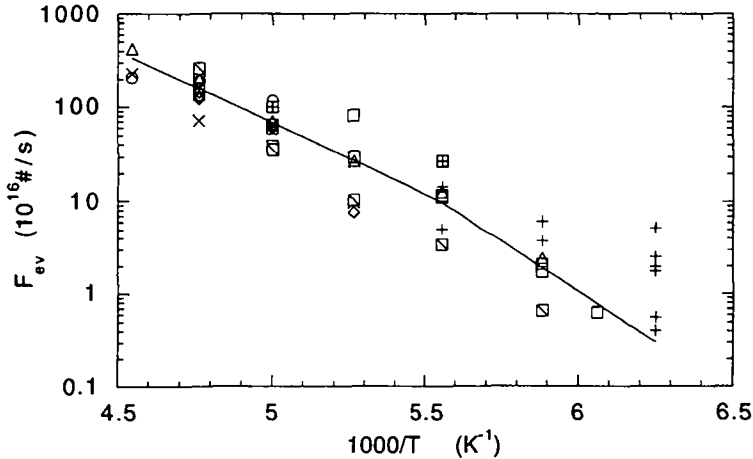

Figure 5.3: Arrhenius plot of F_{ev}. The different symbols correspond to various experiments and two types of sample (condensed and bulk sample). The activation energy of F_{ev} is 7.0±2.0 kcal/mol and 10.0±2.0 kcal/mol in the range of 180 to 220K and 160 to 180K, respectively. The data are normalized to $\omega=152$ s^{-1} and the sample surface of 11.3cm^2 (reactor combination 1, Table 5.1). One monolayer corresponds to $1.1 \cdot 10^{16}$ molecules.

The difference in activation energies of k_c and F_{ev} results in a heat of sublimation of 10.1±3.0 kcal/mol in the range 180 to 220K and 11.6±3.5 kcal/mol in the range 160 to 180K. Both values are within the error limits of the literature value of 12.2 kcal/mol [2]. Despite the fairly large experimental uncertainties in the kinetic parameters from one experiment to the next, no systematic dependence on the type of sample could be detected. The experiments involving an external flow of water vapor yielded identical results to the experiments where only the flow of H_2O originating from the ice sample was monitored.

5.3 Results and Discussion of the Pulsed Valve Experiments

The primary goal of the pulsed valve experiments was to check the numerical value of k_c using a real-time kinetic method. In Chapter 2.4 we present the capabilities of our signal acquisition system at recovering a transient MS signal that is modulated at 150 Hz in order to yield a reliable MS amplitude as a function of time. Experiments were also performed in which an unchopped MS signal was recorded as a function of time. Typical raw data from such experiments are presented in **Figure 5.4**. The signals were recorded using the coupled MS/lock-in detection at m/e 18 and 28, respectively. As the decay rates of the pulses can be as fast as 50 s^{-1} or even exceed this value, the highest digital sampling frequency of 500 Hz in the signal acquisition was needed. For the reference experiments, however, a sampling frequency of 100 Hz was used because the decay rate is equal to k_e, which was 8.55 s^{-1} at most. In the following examples the pulsed valve was opened for 10ms at t=0.2 seconds and the experiments were carried out using the 3 mm orifice. The injected dose can be
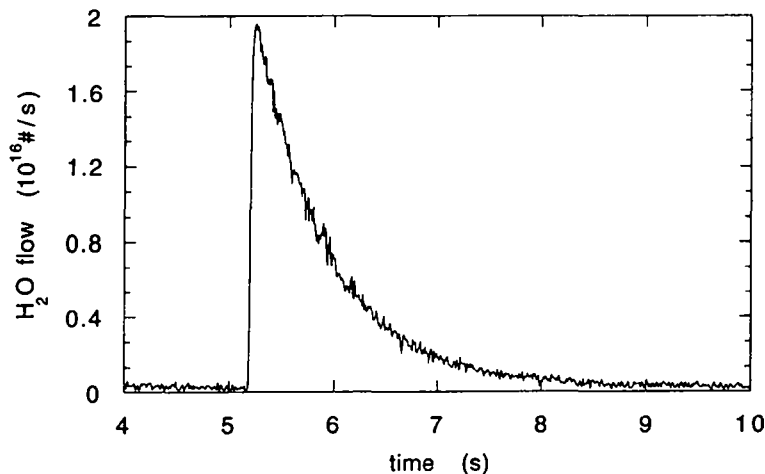
Figure 5.4 a: Time dependent MS data of a pulsed valve reference experiment in which a pulse of water molecules is injected into the cell with the sample compartment closed using a sampling frequency of 100 Hz. The decay is of single-exponential type with a decay constant $k_{dec}=k_e=1.0$ s^{-1} using the 3 mm orifice. The integral under the curve equals the dose of injected molecules corresponding to $1.4 \cdot 10^{16}$ molecules or approximately 1.3 monolayers. The pulsed valve was opened for 10 ms at t=0.2 s.

varied either by changing the pulse length (typically 1 to 10 ms) or by establishing a variable backing pressure in the inlet line (1 to 10 Torr).

Figure 5.4 a shows a reference experiment in which a pulse of H_2O molecules is injected into the cell keeping the sample compartment closed. The decay corresponds to a single-exponential decay with a decay constant equal to k_e. The integral under the curve corresponds to a dose of $1.4 \cdot 10^{16}$ molecules which is equivalent to approximately 1.3 nominal monolayers.

We note that at a sampling frequency of 100 Hz the peak is very sharp and the signal to noise ratio is excellent exceeding 50. It drops to 20 during the pulse due to the transient rise in background pressure as the gas burst is pumped off.
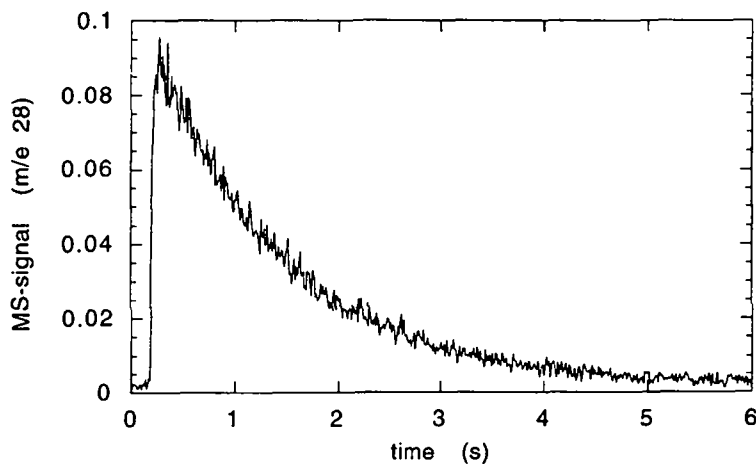
Figure 5.4 b: Time dependent MS data of a pulsed valve reference experiment where a condensed ice sample at 180K is probed by a pulse of $6.2 \cdot 10^{16}$ molecules of N_2 at 100 Hz sampling frequency. The decay constant corresponds to $k_{dec} = k_e = 0.8 \ s^{-1}$ using the 3 mm orifice.

Figure 5.4 b shows a second type of reference experiment where a condensed ice sample at 180K is probed by a pulse of $6.2 \cdot 10^{16}$ molecules of N_2. As the measured decay constant corresponds to k_e for N_2 we conclude that this inert gas does not interact with the ice surface, as expected. Due to small air leaks the signal to noise ratio is worse than in Figure 5.4 a in spite of the higher dose. This is due to the increased difficulty of discriminating of chopped signal against the background level at m/e 28.

Figure 5.4 c shows a typical reactive experiment where a pulse corresponding to a dose of $1.4 \cdot 10^{16}$ water molecules interacts with an ice sample at 180K prepared by vapor condensation at 160K. The steady-state level corresponds to the effusive beam of water molecules leaving the reactor and originating from the ice sample. The steady-state in the cell is perturbed by the water molecules injected across the pulsed valve. Taking into account the different time scales of Figures 5.4 a, 5.4 b and 5.4 c, the decay is clearly faster by an order of magnitude. The upper graph (right hand ordinate) corresponds to the natural log of the raw signal displayed in the lower graph after subtraction of the steady-state level. As can be seen, the decay is of a single exponential type given by $k_{dec} = k_{eff} + k_e$ corresponding to the two competitive loss processes of interest. Note that k_{eff} is numerically equal to k_c within the experimental uncertainty in the framework of the validity of the simple mechanism of Scheme 1.
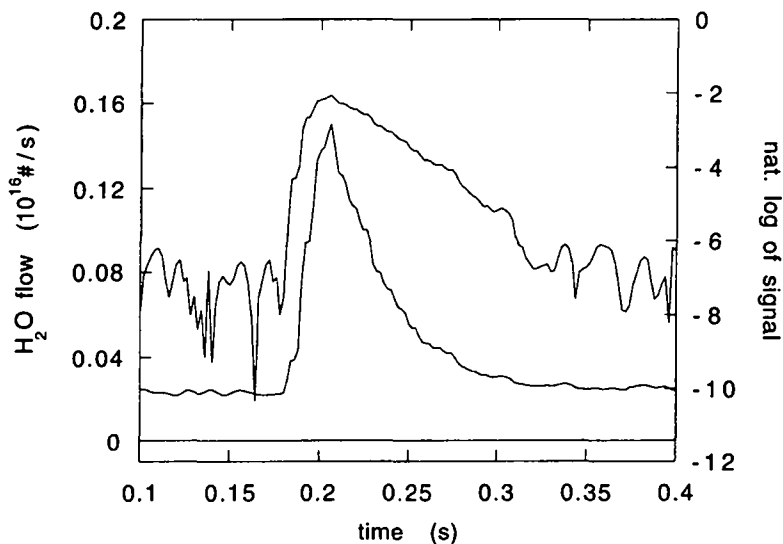
Figure 5.4 c: Time dependent MS data of a reactive pulsed valve experiment where a pulse corresponding to a dose of $1.5 \cdot 10^{16}$ water molecules interacts with an ice sample at 180K prepared by vapor condensation at 160K at 500 Hz sampling frequency. The upper graph (right hand ordinate) corresponds to the natural log of the signal (displayed in the lower graph) after subtraction of the steady-state level. The decay is of a single exponential type given by $k_{dec}=32 \text{ s}^{-1}$ determined in the interval between 0.2 and 0.3 s.

In what follows we present a brief justification of the assertion relating k_{eff} and k_c made above. The time dependent gas phase concentration after perturbation may be written as $[G](t) = [G]_{SS} + \Delta[G](t)$, where $[G]_{SS}$ is the gas phase concentration at steady-state, and $\Delta[G](t)$ corresponds to the time dependent relaxation where the initial amplitude $\Delta[G](t=0)$ is proportional to the injected dose. Using the mechanism of Scheme 1, the variation in concentration may be expressed as follows:

$$d[G](t)/dt = d/dt[[G]_{SS} + \Delta[G](t)] = -k_e\{ [G]_{SS} + \Delta[G](t) \} - k_c\{ [G]_{SS} + \Delta[G](t)\} + R_{ev}$$

By collecting the steady-state terms on the right-hand side and applying the steady-state assumption for the time derivative of $[G]_{SS}$ on the left-hand side, we obtain:

$$d[G]t)/dt = d/dt[\Delta[G](t)] = \underbrace{-(k_e + k_c)[G]_{SS} + R_{ev}}_{=0} - (k_e + k_c)\ \Delta[G](t)$$

leading to:
$$d/dt[\Delta[G](t)] = -(k_e + k_c) \cdot \Delta[G](t) ,$$

which yields the single-exponential solution after integration:

$$\Delta[G](t) = \Delta[G](t=0)\ \exp\{ -(k_e + k_c)\ t \}$$

The three **Figures 5.5 a, b and c** display the dose dependence of k_{eff} at 160, 180 and 200K, using the large aperture reactor for several series of nominally identical experiments. The values of k_{eff} measured in one of the four reactors characterized by different volumes and sample surfaces were normalized to reactor combination 1. Table 5.1 shows the surface to volume ratio and the corresponding sample collision frequency ω for each one of the four reactors. Consequently, the displayed k_{eff} were scaled to ω of reactor combination 1.

The injected dose of the experiments displayed in Figure 5.5. was varied over more than two orders of magnitude changing the pulse length as well as the backing pressure. The lower limit of the dose at each temperature is given by the ratio of the steady-state background flow out of the reactor and the peak pulse. It is obvious that at a large steady-state flowrate of 10^{16} molecules s^{-1} it is difficult
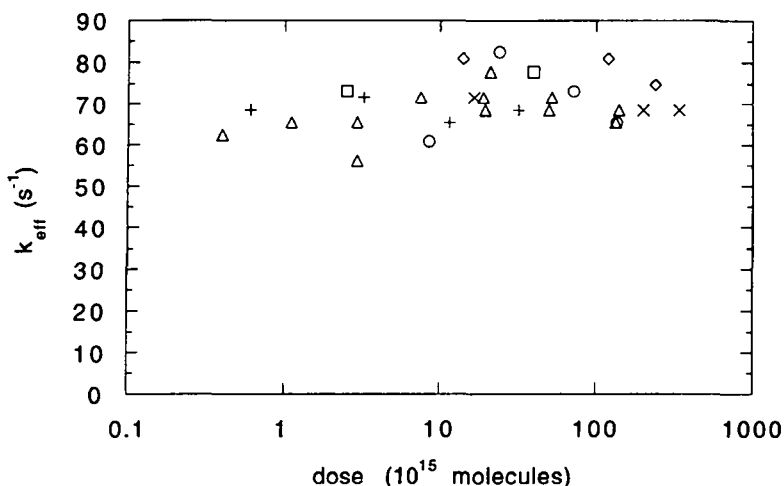
Figure 5.5 a: Dose dependence of k_{eff} measured by pulsed valve experiments at 160K in the 9mm orifice reactor. The various symbols correspond to experiments performed on different days. All displayed data were obtained using the Knudsen reactor of 1830 cm^3 volume and were subsequently scaled to reactor combination 1.

to detect the exponential decay of a pulse of 10^{15} molecules. This is the reason why the lower limit of the dose is shifted to higher values with increasing temperature, thus increasing steady state water vapor pressure. The different symbols in the plots correspond to different sets of measurements. The scatter of the points may be due to various effects such as slight variations in sample preparation, heating of the cell, slight changes in the operating characteristics of the LTS, day-to-day background variation, unstable backing pressure and perhaps contamination of the sample.

At 160K (**Figure 5.5 a**) the dose dependence is hardly noticeable: k_{eff} only varies by about 30% from 63 to 82 s^{-1} over three orders of magnitude in dose. At this temperature the surface is kinetically stable, and each new burst of molecules injected into the reactor immediately condenses. All the displayed data were obtained with the Knudsen reactor of 1830 cm^3 volume and were consequently scaled to reactor combination 1. Therefore, the high values of k_{eff}=82 s^{-1} were not directly observed.

At 180K the dose dependence is more pronounced and k_{eff} varies by a factor of 4 over 2 orders of magnitude in dose (**Figure 5.5 b**). Most experiments were

carried out at this temperature. In order to better describe the dose dependence, the displayed results were obtained over a period of 18 months.

Figure 5.5 b: Dose dependence of k_{eff} measured by pulsed valve experiments at 180K in the large orifice reactor. The various symbols correspond to experiments performed on different days. The displayed results were obtained over a period of 18 months using four different reactor combinations.

Figure 5.5 c: Dose dependence of k_{eff} measured by pulsed valve experiments at 200K in the large orifice reactor. The various symbols correspond to experiments performed on different days.

Figure 5.5 c shows the variation of k_{eff} with increasing dose at 200K where the dose dependence seems to be largest, varying a factor of 5 over less than 2 orders of magnitude in dose.

Figure 5.5 d displays the dose dependence of k_{eff} at 180K using the small aperture reactor. The presented values of k_{eff} are also normalized to reactor combination 1. A comparison with the experiments at the same temperature using the large orifice reactor (Figure 5.5 b) shows that the observed dose dependence does not depend on the orifice size of the reactor. In fact, the values of k_{eff} vary by a factor of 4 over 2 orders of magnitude in dose as in the experiments performed using the large aperture reactor.
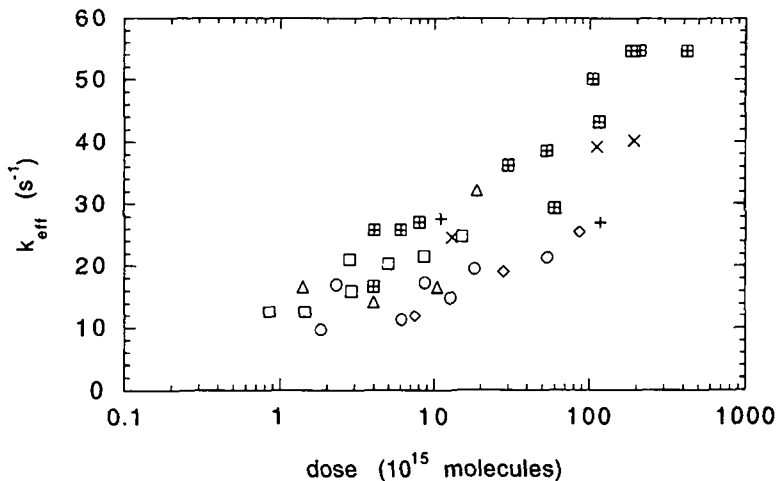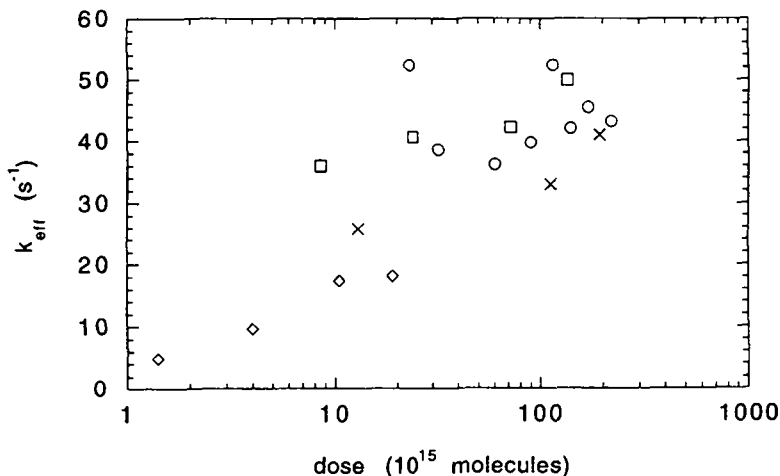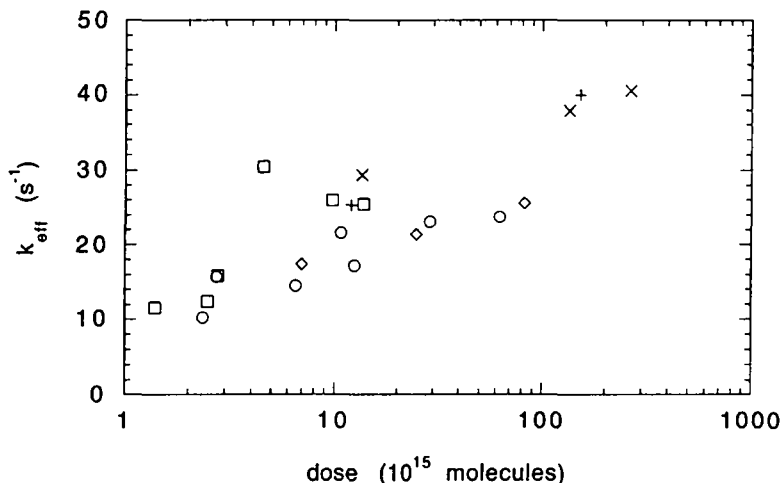

Figure 5.5 d: Dose dependence of k_{eff} measured by pulsed valve experiments at 180K in the small orifice reactor. The various symbols correspond to experiments performed on different days.

The positive dose dependence of k_{eff} may also serve to shed light on the questions, whether or not there is surface heating due to condensation of H_2O vapor on ice under our experimental conditions. In fact, if such an effect were occurring, we would observe a decrease of the effective rate of condensation with increasing dose due to the fact that the condensation rate constant slows down with increasing temperature. This may be seen in the temperature dependence of k_c (Figure 5.2) and of $(k_l + k_s)_{eq}^l$ (Table 5.3 a) discussed below.

Moreover, lock-in test experiments were performed in order to investigate the upper limit of the frequency at which the instrument was still able to follow the

decaying MS signal. These simulations used a programmable function generator and showed that for the ratio of pulse amplitude to steady-state level of the MS-signal at m/e 18 that are typical of our experiments, values of k_{dec} up to 100 s^{-1} could be reproduced with an acceptable error. Chapter 2.4 presents additional details.

The fact that no values of k_{dec} larger than 60s^{-1} were experimentally observed may therefore be attributed to the use of that particular Knudsen reactor. Monte Carlo simulations are currently undertaken in order to confirm or reject this hypothesis [30].

5.4 Chemical Kinetic Modeling

We interpreted the present experimental results using a chemical kinetic model in terms of elementary gas and surface processes. The simple 2-state model of Scheme 1 is obviously not adequate to explain the negative temperature dependence of k_c on the one hand, and the dose dependence of k_{eff} on the other hand. Moreover, in relation to the observed negative activation energy of k_c, the H_2O vapor/ice system must be represented as a complex reaction mechanism consisting of different elementary rate constants all having either no or a positive activation energy. The primary goal of the modeling is therefore to find the simplest mechanism which is capable of explaining the dose dependence of k_{eff} as well as the negative temperature dependence of k_c.

The basic idea in modeling the dose dependence of k_{eff} is to admit two competing adsorption steps, the faster of which becomes dominant at higher partial pressure. These two competing steps may be modeled by introducing two different adsorption sites on the surface, one of which is increasing its population at the expense of the other as a function of partial pressure. We call these two different sites S (surface) and P (precursor), where P is a site on which the adsorption of H_2O vapor is faster.

The first condensation step involves the interaction of G representing gas phase H_2O, S a surface site, I an intermediate surface species and B a bulk molecule of ice:

$$G + S \quad \overset{k_1}{\underset{k_2}{\rightleftharpoons}} \quad I + B \tag{8}$$
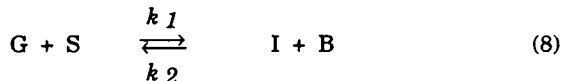
In the following surface transformation I becomes a precursor P at the same time that a surface site S is regenerated. In fact, the surface site S, corresponding to the first adsorption channel given by k_1, becomes available for further adsorption only after supplying an adsorption site to the second adsorption channel (given by P and k_5). This is an important feature enabling a dose dependence that will be effective for at least 50 ms and not less than 10ms as tested in a precursor mediated mechanism:

$$I + B \quad \overset{k_3}{\underset{k_4}{\rightleftharpoons}} \quad P + S \tag{9}$$
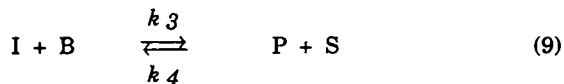
Reactions 9 also correspond to the decoupling of P from the surface sites I and S, which together form the geometric interface between bulk and gas phase.

The second adsorption channel, which is autocatalytic with respect to P, becomes more important at higher pressure than the first one in order to enable the positive dose dependence:

$$G + P \quad \underset{k_6}{\overset{k_5}{\rightleftharpoons}} \quad B + P \qquad (10)$$
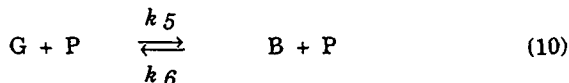
In this mechanism the population of the precursor P on which the autocatalytic adsorption k_5 takes place may exceed a formal monolayer. This is due to the decoupling of S and P and affords more flexibility with respect to modeling of the dose dependence than a previously tested precursor mediated mechanism. However, as will be seen later, the population of P actually never exceeds one monolayer. On the other hand, the sum of the number of surface species S and I may never exceed a monolayer due to the model constraint, that adsorption is taking place on free surface sites S according to the Langmuir kinetic adsorption model. It corresponds to the total available surface sites on the geometrical sample surface resulting in the relation (11) $I(t) + S(t) = S_0$ at any time t, where $S_0 = 1.1 \cdot 10^{16}$ molecules.

Moreover, all reactions are reversible in order to enable the experimentally observed ice evaporation. In fact, only if all elementary reactions are reversible will the perturbation represented by the H_2O pulse relax to an experimentally observed steady state.

A distinctive feature of the above mechanism is the fact that the present model does not correspond to the precursor mechanism proposed by George and coworkers [19]. In their mechanism an incident molecule is trapped on the surface in a weakly bound state before it desorbs either back into the gas phase or is incorporated into bulk ice according to reaction (12):

$$H_2O \ (g) \ <=> \ H_2O \ (ads) \ <=> \ H_2O \ (s) \qquad (12)$$
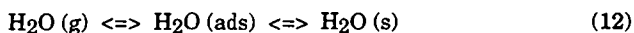
In the present mechanism (reactions (8) to (10)), however, we have two competing channels, each one transforming a gas phase molecule into bulk ice. The interaction of the two different adsorption sites is not direct but goes via a surface transformation involving an intermediate species I, reaction (9).

5.4.1 Solution Strategy for the Model Simulation

The detailed strategy together with the FORTRAN routine is given in the Appendix. In summary, we are seeking a set of the six fit parameters k_1 to k_6 which approaches best the six experimental observables G_{ss}^L , G_{ss}^S , k_{eff}^L (low and high dose) and k_{eff}^S (low and high dose). As we are conducting perturbation experiments, we may write a steady state condition for each species intervening in the mechanism, that is for G, P, S and I. Writing these four equations (=steady state conditions) for one orifice shows that only three of them are linearly independent due to the restrictive condition in our mechanism which is the conservation of S and I (see equation (11)). In addition to the six fit parameters there are also the variables expressing the steady state concentration at the orifice under consideration, i.e. G_{ss}^i, S_{ss}^i, P_{ss}^i and I_{ss}^i where i stands for the escape orifice (large or small). As we are modeling experiments performed using two different orifices, we dispose of a total of six linearly independent steady state conditions and two sets of four steady state concentrations each. Of this total of eight steady state concentrations, the two gas phase concentrations are determined from experiment while I_{ss}^i and S_{ss}^i are correlated by equation (11). We consider the remaining four independent steady state concentrations as four variables which correspond to four degrees of freedom in addition to the six fit parameters. This total of ten unknowns are related to each other by the six linearly independent steady state conditions, and consequently four of them are undetermined corresponding to four degrees of freedom. We chose them as being k_1, k_3, k_5 and P_{ss}^L. It turns out however, that these four fit parameters do not afford sufficient flexibility in order to find an overall good fit. The idea is therefore to admit an error of 30% on the two gas phase steady state concentrations due to their natural day to day variation. By this procedure, we practically increase by one the number of degrees of freedom to obtain the five fit parameters k_1, k_3, k_5, P_{ss}^L and S_{ss}^L.

**5.4.1 Description of the Model in terms of Bond Valences**

The present mechanism also elucidates how a "free" gas phase molecule is stepwise incorporated into tetrahedrally coordinated bulk ice [30]. This can best be described introducing the concept of bond valences. We call a bond valence the capability of a water molecule to engage in hydrogen bonding with another water molecule. This concept is similar to the one used by Devlin et al. [31] who interpret experimental spectra invoking two- or three-coordinated molecules with a "dangling", that is unsaturated, coordination at the hydrogen, two- or three-coordinated molecules with a "dangling" coordination at the oxygen and four coordinated molecules forming the characteristic structure of ice with its distorted tetrahedra. As a molecule in bulk ice has four neighbors that are bound by hydrogen bonds, we know that each water molecule can bind up to four other molecules in a distorted diamond lattice. In other words, we can assign four bond valences or four sites of unsaturation to a "free" gas phase molecule G, three bond valences to the intermediate I, two to P and one bond valence to each surface site S. In **Scheme 2** the bond valences are represented by dots. The bulk species B obviously has no free bond valence as it is completely saturated, that is four-coordinated. In this way we can interpret reaction (8) as forming a bond between G and S, each one contributing one valence and thus becoming I and B, respectively, with the total count of bond valences decreased by two. The transformation from I into P and S corresponding to reaction (9) can be viewed in detail as follows:

(A) $2\ B \rightarrow 2\ S$ breaking up of a hydrogen bond between two bulk molecules forming two surface sites with a single free valence and thereby "activating" the surface or increasing the total count of free valences by two.

(B) $I + S \rightleftharpoons P + B$ subsequent formation of a bond between I and S leading to the reduction of the total count of free valences by two.

(C) $I + B \rightleftharpoons P + S$ This is the sum of (A) and (B).

The net process may occur either in a stepwise, or concerted (synchronous) manner according to (C) (see Scheme 2). Note that although I has three bond

valences, it does not interact with the gas phase. As it is a singly-coordinated species, it has more degrees of freedom. Consequently, its valences may not be clearly localized and the gas phase molecules may have a lower probability of interaction with I at the pressure of our system.

The autocatalytic reaction (10) can be interpreted as the simultaneous formation of two hydrogen bonds so that a gas phase molecule is converted into a new P via consumption of a former P. In such a way clusters of B can be formed with H_2O in a P state sitting on top.

$$(8)$$

$$(9)$$

$$(10)$$
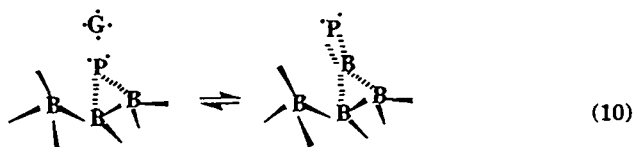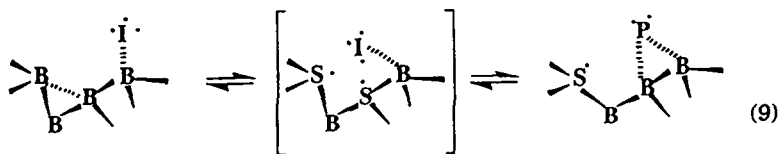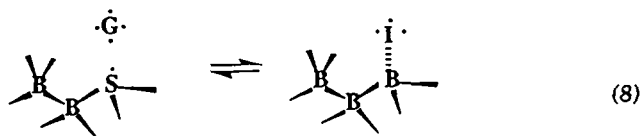
Scheme 2

5.5 Modeling Results and Discussion

Figures 5.6 a to f display typical fits to six pulsed experiments which present agreement of the fitted with the experimental k_{dec}. As it is outside of the scope of this work to model the rise of the pulse, the model decay was shifted to match the experimental data. Within our detection limit the experimental decays are always of single-exponential type. The model decay, however, does not strictly follow a simple exponential decay, as expected from a complex two channel adsorption mechanism such as the one described in equations (8) to (10). In fact, the rate law for H_2O adsorption is not unimolecular any longer because of the pressure dependence. For the case of a pulsed experiment at high dose, the decay corresponds to a single exponential decay only over approximately one order of magnitude in the MS signal. For this reason, the values for k_{dec} given in
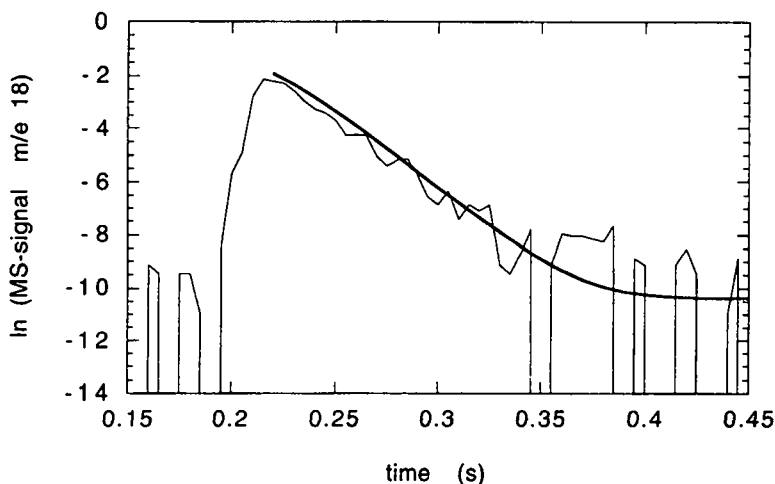
Figure 5.6 a: Display of a typical pulsed experiment at 160K, where a dose of $1.2 \ 10^{17}$ water molecules was injected, and a model fit. The experimental trace (thin line) as well as the model trace (thick line), both taken relative to their respective steady state levels, are of single exponential type over at least two orders of magnitude corresponding to $k_{dec}=56 \ s^{-1}$ in both cases. The experimental trace was obtained using the 1830 cm^3 reactor with an orifice of 8 mm diameter and a sample surface of 11.3 cm^2 (reactor combination 3, Table 5.1).

Table 5.2 and discussed below were all taken over a time interval in which the decay was still of single exponential type. For completeness sake we have to mention that the model traces presented in Figures 5.6 a to f correspond to a

Figure 5.6 b: Display of a typical pulsed experiment at 160K (thin line) using the small escape aperture (reactor combination 3), where a dose of $0.4 \cdot 10^{15}$ water molecules was injected, and a model fit (thick line). The decay of single exponential type corresponds to k_{dec}=55.6 s^{-1} for the experiment and k_{dec}=62 s^{-1} for the model.

Figure 5.6 c: Display of a typical pulsed experiment at 180K (thin line) using the large escape aperture (reactor combination 2), where a dose of $19.3 \cdot 10^{16}$ water molecules was injected, and a model fit (thick line). The decay of single exponential type corresponds to k_{dec}=47.7 s^{-1} for the experiment and k_{dec}=47 s^{-1} for the model.
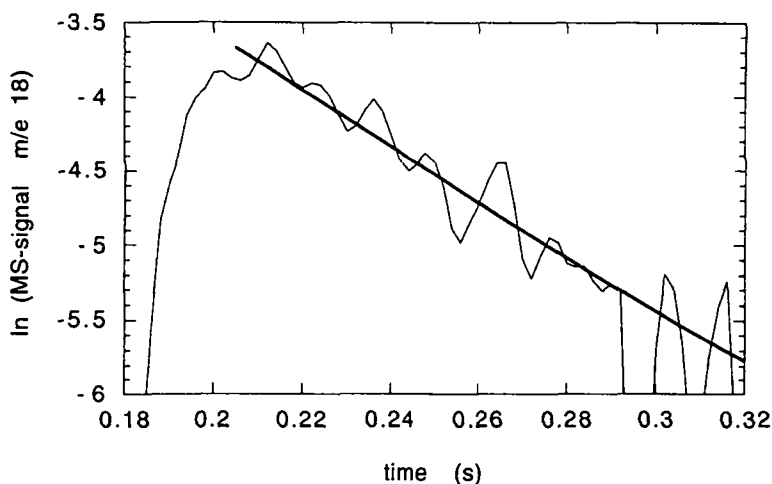
Figure 5.6 d: Display of a typical pulsed experiment at 180K (thin line) using the small escape aperture (reactor combination 1), where a dose of $2.8 \cdot 10^{15}$ water molecules was injected, and a model fit (thick line). The decay of single exponential type corresponds to $k_{dec}=16.9$ s^{-1} for the experiment and $k_{dec}=19$ s^{-1} for the model.
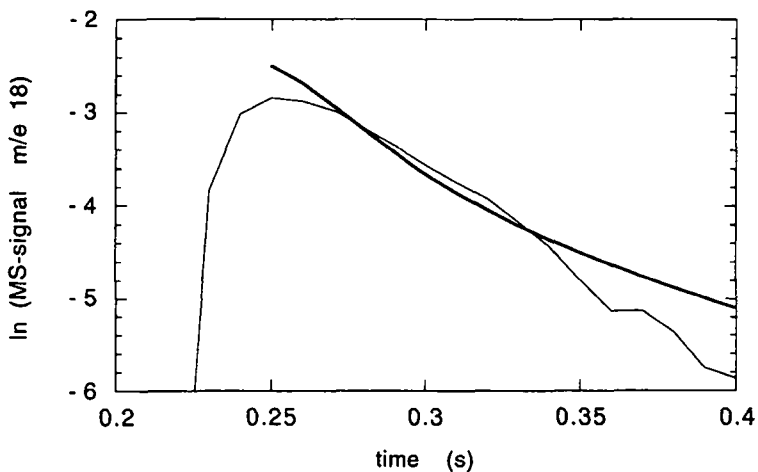
Figure 5.6 e: Display of a typical pulsed experiment at 200K (thin line) using the small escape aperture (reactor combination 3), where a dose of $12.2 \cdot 10^{16}$ water molecules was injected, and a model fit (thick line). The decay of single exponential type corresponds to $k_{dec}=35.4$ s^{-1} for the experiment and $k_{dec}=39$ s^{-1} for the model.

simulation of the respective reactor as given in Table 5.1 implying that we used
the appropriate values of k_e, k_1 and k_5, the last two rate constants being scaled
with respect to the respective sample collision frequency ω. Changing these three
rate constants is equivalent to changing the volume, the sample surface area and
the orifice of a reactor. In such a case, the steady state concentrations of all the
four species are affected as well. The steady state concentrations serving
hereafter as new initial conditions for the modeling of a pulsed valve experiment
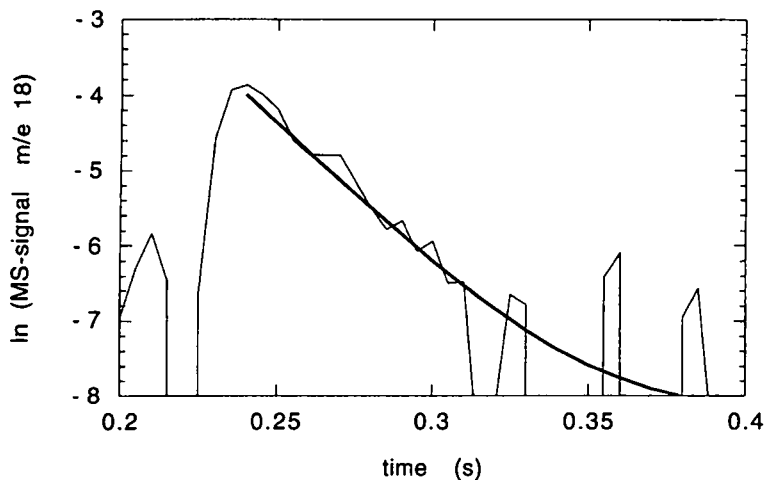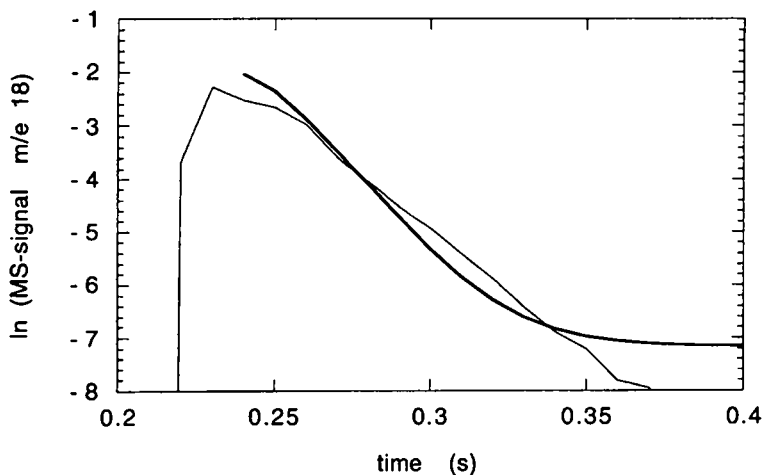were determined in a simulation on a long time scale.
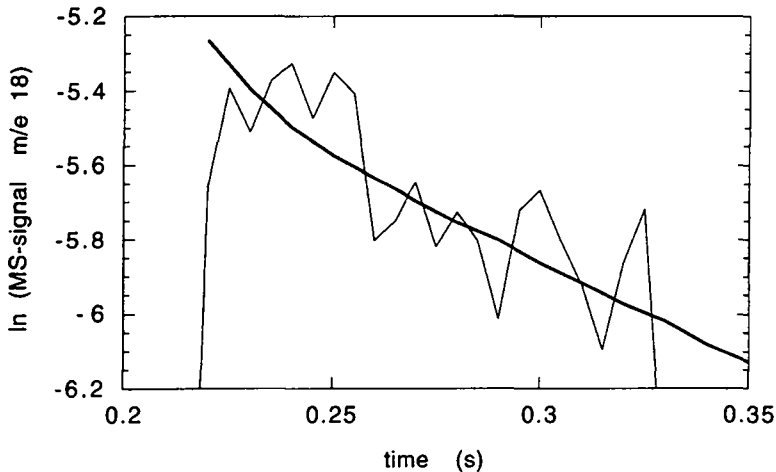
Figure 5.6 f: Display of a typical pulsed experiment at 200K (thin
line) using the large escape aperture (reactor combination 3), where a
dose of $1.4 \cdot 10^{15}$ water molecules was injected, and a model fit (thick
line). The decay of single exponential type corresponds to $k_{dec}=12.5$ s^{-1}
for the experiment and $k_{dec}=17$ s^{-1} for the model.

Table 5.2 shows representative results of selected pulsed condensation/
evaporation experiments at 160, 180 and 200 K. At each temperature we selected
a set of 4 experiments, resulting from the combination of large (L) and small (S)
orifice with high and low doses. Each of these four experiments is characterized
by a steady-state level G_{ss} preceding and following the H_2O pulse whose lifetime
is given by a decay constant k_{dec} .

Furthermore, Table 5.2 displays the 6 rate constants (k_1 to k_6) and the
resulting steady-state concentrations of the 4 species namely G_{ss}, P_{ss}, S_{ss}, I_{ss},

Table 5.2: Observations (k_{dec}, G_{ss}, dose) and Model parameters (transferable rate constants in parenthesis) in the system H_2O vapor/ice for three temperatures, two orifices (L, S) and high/low doses of the H_2O pulse. ($A_s/V=11.3/1180=9.6\cdot10^{-3}cm^{-1}$).

Temp Orifice / Dose	Dose 10^{16}#	k_{dec} a) (s^{-1}) experiment	k_{dec} (s^{-1}) model fit	G_{ss} 10^{16}# experiment	G_{ss} 10^{16}# model fit	P_{ss} $1.1\cdot10^{16}$	S_{ss} $1.1\cdot10^{16}$	I_{ss} $1.1\cdot10^{16}$	k_1 [10^{-16}]	k_2 b)	k_3 b)	k_4 [10^{-16}]	k_5 [10^{-16}]	k_6 b)
160 K L low	0.04	69.9	63	0.019	0.019	0.35	0.5	0.5	5 s^{-1}	0.1 s^{-1}	500 s^{-1}	1429 s^{-1}	150 s^{-1}	3.3 s^{-1}
160 K L high	12	88.5	78	0.019	0.019	0.35	0.5	0.5	(56.5 $cm^2\cdot s^{-1}$)	(9.6·10^{-4} $cm^{-1}\cdot s^{-1}$)	(4.79 $cm^{-1}\cdot s^{-1}$)	(1.5·10^{5} $cm\cdot s^{-1}$)	(1695 $cm^2\cdot s^{-1}$)	(0.032 $cm^{-1}\cdot s^{-1}$)
160 K S low	0.04	55.6	62	0.02	0.021	0.39	0.47	0.53						
160 K S high	14	71.1	80	0.02	0.021	0.39	0.47	0.53						
180 K L low	0.085	20.1	20	0.147	0.12	0.05	0.2	0.8	30 s^{-1}	0.9 s^{-1}	500 s^{-1}	4·10^4 s^{-1}	150 s^{-1}	36 s^{-1}
180 K L high	19.3	47.7	47	0.147	0.12	0.05	0.2	0.8	(339 $cm^2\cdot s^{-1}$)	(8.6·10^{-3} $cm^{-1}\cdot s^{-1}$)	(4.79 $cm^{-1}\cdot s^{-1}$)	(4.2·10^{6} $cm\cdot s^{-1}$)	(1695 $cm^2\cdot s^{-1}$)	(0.345 $cm^{-1}\cdot s^{-1}$)
180 K S low	0.28	16.9	19	0.16	0.22	0.093	0.12	0.88						
180 K S high	13.5	38.7	39	0.16	0.22	0.093	0.12	0.88						
200 K L low	0.14	12.5	17	1.69	1.3	0.05	0.2	0.8	50 s^{-1}	16 s^{-1}	500 s^{-1}	4·10^4 s^{-1}	150 s^{-1}	390 s^{-1}
200 K L high	22	50.7	50	1.69	1.3	0.05	0.2	0.8						
200 K S low	0.4	17.3	18	2.1	2.4	0.093	0.12	0.88	(565 $cm^2\cdot s^{-1}$)	(0.153 $cm^{-1}\cdot s^{-1}$)	(4.79 $cm^{-1}\cdot s^{-1}$)	(4.2·10^{6} $cm\cdot s^{-1}$)	(1695 $cm^2\cdot s^{-1}$)	(3.74 $cm^{-1}\cdot s^{-1}$)
200 K S high	12.2	35.4	39	2.1	2.4	0.093	0.12	0.88						

a) For typical error limits see Figure 5.5.

b) Pseudo first order rate constant including B: $k_2 = \tilde{k}_2 \cdot B$, $k_3 = \tilde{k}_3 \cdot B$ and $k_6 = \tilde{k}_6 \cdot B$ where the constant with superscript ~ is the second order rate constant.

expressed as fractions of $S_0=1.1\cdot10^{16}$ molecules corresponding to a nominal monolayer of the total available geometric surface area of the ice sample. The rate constants result from the simulation of signals in the large and the small orifice reactor at the three investigated temperatures. At 160K, where the dose dependence is less pronounced and the experimental values of k_{dec} are higher than at 180 and 200K, we find higher steady-state concentrations P_{SS} and S_{SS} for P and S corresponding to longer surface residence times, as expected.

A somewhat surprising feature is that the steady-state concentrations of P and S, namely P_{SS} and S_{SS}, at 180 and 200K are identical. One would normally expect that the lifetime of P would decrease with increasing temperature, thus favoring evaporation. This goes to show, however, that the surface populations are foremost sensitive to k_{eff}, because we have almost the same experimentally determined k_{eff} as a function of injected dose at 180 and 200K.

Note that k_2, k_3 and k_6 are pseudo first-order rate constants because they include B (bulk ice) which is constant, whereas k_1, k_4 and k_5 are second order rate constants. In order to compare the six rate constants k_1 to k_6, we have to consider reaction rates or pseudo first order rate constants since the rate laws are not all first order.

Table 5.3 a: Modeled equilibrium populations of surface species governing the system H_2O/ice at three temperatures. The rate constants refer to Knudsen Cell combination 1 (Table 5.1).

Temp	P_{eq}	S_{eq}	I_{eq}	R_3^{eq} a)	R_4^{eq} b)	$(k_1+k_5)_{eq}^I$	γ_{eq} c)	γ_{eq} d)	R_{ev}^{eq} e)
	$1.1\cdot10^{16}$#	$1.1\cdot10^{16}$#	$1.1\cdot10^{16}$#	10^{16}#/s	10^{16}#/s	1/s	model	expt.	10^{16}#/s
160 K	0.4	0.47	0.53	292	325	62.4	0.41	0.41±0.03	1.5
180 K	0.1	0.11	0.89	490	532	18.3	0.12	0.13±0.03	4.8
200 K	0.1	0.11	0.89	490	532	20.5	0.14	0.11±0.03	58.5

a) $R_3^{eq} = k_3 \cdot I_{eq}$

b) $R_4^{eq} = k_4 \cdot S_{eq} \cdot P_{eq}$

c) $\gamma = \dfrac{(k_1+k_5)^I}{\omega}$, where $\omega=152s^{-1}$ and $(k_1+k_5)^I = k_1 \cdot S_{eq} + k_5 \cdot P_{eq}$.

d) calculated using the values of k_{eff} for the low dose and the small orifice reactor.

e) $R_{ev}^{eq} = k_2 \cdot I_{eq} + k_6 \cdot P_{eq}$

Table 5.3 a and b summarize the results of the simulation for both the rate of evaporation as well as the rate of condensation. We distinguish two different cases at each temperature (160, 180 and 200K): **Table 5.3 a** presents the equilibrium situation where k_e has been set to 0 such that the model simulates an experiment within a closed system. **Table 5.3 b** on the other hand shows the high dose pulse simulation for the large and the small orifice reactors for which the peak values of each species-concentration has been determined.

The most important result in Table 5.3 a is that γ at equilibrium is higher by a factor of 3 at 160K ($\gamma = 0.41$) compared to 200K ($\gamma = 0.14$) which thus corresponds to the negative temperature dependence of k_c displayed in Figure 5.2. At higher transient pressures (see Table 5.3 b)) γ is higher assuming values between 0.3 and 0.6 which depend on the temperature to a lesser degree. In general, values for γ in the range of 0.1 to 1 are in agreement with the values cited most in the literature. We thus propose that the uptake coefficient $\gamma = \dfrac{(k_1 + k_5)^I}{\omega}$ is pressure dependent, a result that may in part help to explain the large scatter of γ values found in the literature [19]. However, we do not propose a rational explanation for the individual values of the uptake or accommodation coefficients obtained in the various experiments, as this task clearly lies outside the scope of this work.

Table 5.3 b: Modeled peak values of surface species upon pulsed dosing of H_2O vapor in the presence of ice at three temperatures and using two orifices (L, S). The rate constants refer to Knudsen Cell combination 1 (Table 5.1).

Orifice / Temp	P_{max} $1.1 \cdot 10^{16} \#$	S_{min} $1.1 \cdot 10^{16} \#$	I_{max} $1.1 \cdot 10^{16} \#$	R_3^{max} $10^{16} \#/s$	R_4^{max} $10^{16} \#/s$	$(k_1 + k_5)^I_{max}$ $1/s$	γ_{max} model	γ_{max} expt.	R_{ev}^{max} $10^{16} \#/s$
L / 160 K	0.56	0.38	0.62	341	368	85	0.56	0.58±0.03	2.1
S / 160 K	0.63	0.36	0.64	341	392	96	0.63	0.47±0.03	2.3
L / 180 K	0.46	0.03	0.97	534	668	70	0.46	0.32±0.03	19.1
S / 180 K	0.40	0.03	0.97	534	581	61	0.40	0.26±0.03	16.8
L / 200 K	0.35	0.03	0.97	534	508	54	0.36	0.36±0.03	167
S / 200 K	0.30	0.04	0.96	528	581	47	0.31	0.23±0.03	145

Table 5.3 presents the pressure dependence of the surface population of the catalytic precursor P which is another consequence of the dose dependence of k_{eff}. We see that at 180 and 200K the concentrations of P are higher by at least a factor of 3 in the peak case compared to the equilibrium case. This difference is less pronounced in the small orifice case, which seems to be in contradiction to the expected pressure dependence. However, referring to Table 5.2 we note that the injected dose in the case of the small orifice reactor is almost a factor of 2 smaller than the one corresponding to the large orifice reactor which explains this apparent discrepancy. For the same reason, γ_{max} is slightly smaller in the case of the small orifice reactor than in the one of the large orifice reactor.

      Table 5.4 presents the activation energies for the rate constants k_1, k_2, k_5 and k_6, the equilibrium rates of conversion/evaporation R_3, R_4 and the pseudo first order rate constants $(k_1+k_5)^I$ and $(k_2+k_6)^I$ as determined in Table 5.3 a. As expected, the rate constants k_1, k_2, R_3, R_4, k_5 and k_6 have activation energies larger than or equal to 0. In particular, we find an activation energy of 3.6 kcal/mol for the rate constant k_1 which is a rather high value for an adsorption process.

Table 5.4: Temperature dependence of the rate constants obtained in the model.

Temperature	k_1	k_2	R_3	R_4	k_5	k_6	$(k_1+k_5)^I$	$(k_2+k_6)^I$
	1/s	1/s	10^{16}#/s	10^{16}#/s	1/s	1/s	1/s	1/s
160 K	5	0.1	292	325	150	3.3	62.4	1.5
180 K	30	0.9	490	532	150	36	18.3	4.8
200 K	50	16	490	532	150	390	20.5	58.5
activation energy (kcal/mol)	3.6	8	0.85	0.8	0	7.6	-1.8	5.7

However, if we calculate the activation energy of the net pseudo first-order rate of condensation given by $(k_1+k_5)^I$, we find a negative value of -1.8 kcal/mol over the temperature range where model data are available (160 to 200K). This result is in agreement with the negative activation energy found experimentally for k_c using the simple two state mechanism of Scheme 1. In the temperature range between 180 and 220K the value of -3.1±1.5 kcal/mol obtained by experiment is slightly larger than the one determined in the model. This disagreement becomes less important if we calculate an activation energy for k_c over the whole temperature range where experimental data are available (160 to 200K). In this

case one finds an activation energy of -2.5 ± 1.5 kcal/mol. Moreover, our model is not based on the same precursor mediated mechanism as the one proposed by George and coworkers [19].

In addition, we see that the activation energies corresponding to the process of evaporation k_2 and k_6 are almost equal (8.0 and 7.6 kcal/mol, respectively). The activation energy for the net evaporation given by $(k_2+k_6)^I$ in the temperature range 180 to 200K is 8.6 kcal/mol which is in fair agreement with the one found experimentally for R_{ev} above 180K, namely 7.0 ± 2.0 kcal/mol, following the simple mechanism of Scheme 1. The model thus predicts a heat of sublimation of 10.4 ± 2.0 kcal/mol identical to the one found experimentally and is therefore consistent with the thermodynamics of the H_2O system.

The rates of transformation of the surface species R_3 and R_4 have zero and a very small activation energy of 0.8 kcal/mol, respectively. As the absolute values of these rates are high compared to the other ones in the model, we conclude that the surface is very dynamic over the whole investigated temperature range as far as lateral mobility of H_2O is concerned.

In this discussion of the activation energies obtained in the model we must not forget that the activation energies depend on the experimental input data to the model. In the face of an uncertainty of 30% in the steady state values used in the model, it is not surprising that we obtain rather large uncertainties in the rate parameters of the involved reactions. Moreover, it is very difficult to measure reliable steady state values for water vapor in the presence of ice at 160K, because we attain the detection limit of the mass spectrometer at 10^{14} #/s.

5.6 Conclusions

Using the two-aperture flow reactor in steady state experiments we were able to measure the water vapor pressure down to 170K which was found to be in agreement with literature data [28]. The data obtained in two different Knudsen reactors allows us to interpret the data using a simple mechanism given in terms of the rate constant for adsorption of H_2O vapor on ice, k_c , and F_{ev}, the rate of evaporation of H_2O. The values of F_{ev} show that the surface is very dynamic: at 200K 70±10 monolayers per second evaporate and condense at equilibrium. For k_c a negative activation energy was obtained pointing towards a precursor mediated adsorption mechanism as suggested by George and coworkers [19].

In addition, we report the first real time kinetic measurements of water condensation on ice at stratospherically relevant temperatures. By means of pulsed valve experiments, where a burst of injected water molecules perturbs the steady-state pressure in the reactor, the hypothesis of precursor mediated condensation is tested and rejected. At temperatures above 160K, the pulsed valve experiments exhibit a positive dose dependence, i.e. the net condensation rate constant increases with increasing dose. This pressure dependence of the condensation rate constant may be explained by an autocatalytic mechanism. In this mechanism two condensation channels compete with each other. The two channels involve two different surface species one of which leads to autocatalytic condensation. Using such a mechanism we are able to show the equivalence of k_c obtained in steady state and k_{eff} in pulsed valve experiments. Moreover, both the positive pressure dependence of k_{eff} and the negative activation energy of k_c are easily interpreted. We thus propose a different mechanism for condensation/evaporation of water on ice which does not invoke a weakly physisorbed precursor state before it is incorporated into the bulk as postulated by George and coworkers [19].

The experimentally observed dose dependence of the condensation rate constant may also help to explain the considerable range of γ found in the literature varying between 0.01 and 1.

As a corollary we retain the conclusion that the present experiments are able to differentiate between at least three kinetically distinguishable species governing the condensation and evaporation of H_2O vapor onto ice despite the fact that we exclusively monitor the gas phase H_2O density.

The importance of the present findings with respect to atmospheric chemistry has to be checked and assessed in global model calculations. So far, we

may only speculate on the potential impact of these results. As far as the chemistry of aircraft plumes is concerned, it is known that the amount of water vapor at flight altitudes north of 40° N has increased by at least 1% due to air traffic [33], each kg of kerosene producing 1.24 kg of water [34]. Because of the long residence time, thin air and low temperatures, a high global warming effect results. In fact, one water vapor molecule at flight altitudes is up to 200 times more effective in this respect than a CO_2 molecule [35]. An even stronger greenhouse warming is caused by air-traffic water in the form of ice crystals, ocurring at altitudes between 8 and 13 km at temperatures below -40°C. Only part of the water is visible as contrails. The ice crystals react in the manner of cyrrus clouds - especially the "thin" ones which are transparent to sunlight but keep back infrared radiation from the earth [36]. We therefore suggest that the present results may be more important in the context of aircraft contrails than in the one of cloud growth, where especially the change of water partial pressure is significant.

5.7 References and Notes

[1] Koros, R. M.; Deckers, J. M.; Andres, R. P.; Boudart, M. Chem. Eng. 1966, 21, 941.

[2] Davy, J.G.; Somorjai, G.A. J. Chem. Phys. 1971, 55, 3624.

[3] Leu, M.-T. Geophys. Res. Let. 1988, 15, 17.

[4] Pruppacher, H. R. Microphysics of Clouds and Precipitation; D. Reidel Pub. Co.: Dordrecht, Holland, 1978.

[5] Solomon, S., Rev. Geophys. 1988, 26, 131.

[6] Molina, M.J; Tso, T.-L.; Molina, L.T.; Wang, C.-Y., Science 1987, 238, 1253.

[7] Tolbert, M.A; Rossi, M.J.; Malhotra, R; Golden, D.M., Science 1987, 238, 1258.

[8] R. P. Turco, Atmospheric Effects of Stratospheric Aircraft: A First Program Report, NASA Ref. Publ. 1992, 63, 1272.

[9] Toon, O. B. and Tolbert, M.A., Nature 1996, 375, 218.

[10] Goodman, J.; Toon, O. B.; Pueschel, R. F.; Snetsinger, K. G.; Verma, S. .J. Geophys. Res. 1989, 94, 16449.

[11] The Chemistry of the Atmosphere: Its impact on global change. editor: J. Calvert; Blackwell Scientific Publications, Oxford, England, 1994

[12] Taleb, D.; Mirabel, P. AERONOX, The Impact of NOx Emissions from Aircraft Upon the Atmosphere at Flight Altitudes 8-15km, editor: U. Schumann, EC-DLR Publication on Research related to Aeronautics and Environment, 1995, p.233

[13] Appleman, H.; Bull. Amer. Meteor. Soc.,1953, 31, 14.

[14] Knollenberg, R.G.; Journal of the Atmospheric Sciences,1972, 29, 1367.

[15] Gross, G.W. J. Geophys. Res. 1982, 87, 7170.

[16] Paterson, W.S.B. The Physics of Glaciers, Pergamon Press Ltd. Oxford, England, 1980.

[17] Chen, J.-P.; Crutzen, P.J. J. Geophys. Res. 1994, 99, 18847.

[18] Mozurkewich, M. Aerosol Science and Technology 1986, 5, 223.

[19] D.R. Haynes; N.J. Tro and S.M. George, J. Phys. Chem. 1992, 96, 8502.

[20] Marti, J.; Mauersberger, K. Geophys. Res. Lett. 1993,20, 363.

[21] Sei, T.; Gonda, T. J. Cryst. Growth 1989, 94, 697

[22] Hu, J.; Xiao, X.-D.; Ogletree, D.F.; Salmeron, M. Science, 1995, 268, 267.

[23] Tolbert, M.A; Middlebrook, A.M.,J. Geophys. Res. 1990, 95, 22423.

[24] Weinberg, W.H. Kinetics of Interface Reactions; Grunze, M., Kreuzer, H.J., Eds.;Springer Verlag: New York, 1987; p 94

[25] K. Tabor; L. Gutzwiller and M. J. Rossi, J. Phys. Chem. 1994, 98, 6172.

[26] Fenter, F.F.; Caloz, F. and Rossi, M.J. J. Phys. Chem. 1994, 98, 9801.

[27] Wise, H.; Ablow, C.M. J. Chem. Phys., 1958, 29, 634.

[28] Jancso, G.; Pupezin, J.; Van Hook, W.A. J. Chem. Phys. 1970, 74, 2984.

[29] Wexler, A. Journal of Research of the National Bureau of Standards-A. 1977, 81A, 520.

[30] Fenter, F.F.; Caloz, F.; Tabor, K.; Gutzwiller, L.S. and Rossi, M.J., in preparation

[31] Eisenberg, D.; Kauzmann, W. The Structure and Properties of Water, Oxford University Press:)New York and Oxford, 1969.

[32] Devlin, J.P.; Buch, V. J. Phys. Chem. 1995, 99, 16534.

[33] Fransen, W. & Peper, J. Atmospheric Effects of High-Flying Subsonic Air Traffic and Operational Measures to Mitigate these Effects. Report by the Netherlands Directorate General of Civil Aviation and the Royal Netherlands Meteorological Institute, Den Haag, The Netherlands, 1994.

[34] Egli, R. Climatic Effect of Air Traffic. Environmental Conservation, 1995, 22, 196.

[35] Grassl, H. Possible climatic effects of contrails and additional water vapor. p 124 in Air Traffic and the Environment (Ed. U. Schumann). Springer Verlag, Berlin & Heidelberg, Gemmany, 1990.

[36] Liou, K.N., Ou, S.C. and Koenig, G. An investigation of the climatic effect of contrail cirrus. Pp. 154 69 in Air Traffic and the Environment (Ed. U. Schumann). Springer Verlag, Berlin & Heidelberg, Germany, 1990.

Chapter Six - Uptake Experiments of HCl on Ice

6.1 Introduction

In the past different theoretical assumptions have been made in order to explain the occurrence of the ozone hole over Antarctica. Today it is known with certainty that the presence of both, particular meteorological conditions of the Arctic winter as well the chemical composition of the atmosphere are responsible for the catalytic ozone depletion. In fact, a vortex forms in wintertime over the Antarctic continent, and to a lesser extent also over the Arctic region, which separates the airmasses from the ones of the midlatitudes. This isolation together with a significant cooling of the airmasses to below 190K allows for the formation of polar stratospheric clouds (PSC's). Under these conditions, the Antarctic atmosphere may be represented as a chemical reactor during the polar night.

There are two types of PSC: type I consists of nitric acid trihydrate (NAT) crystals, which form several degrees above the frost point of water; type II consist of water-ice crystals. It appears, however, that this is only a very rough and perhaps inaccurate classification. In fact, Toon&Tolbert [1] have recently reanalyzed infrared spectra of type I PSC's obtained over Antarctica in September 1987 using recently measured optical constants of the various compounds that may be present in PSC's. They find that these PSC's had a more complex composition, perhaps that of a ternary solution of water, nitric acid and sulfuric acid. Because cloud formation is sensitive regarding their chemical composition, this finding is important for the understanding of the locations and conditions under which PSC's may form. In addition, the extent of ozone loss depends on the ability of PSC's to remove NO_x permanently through sedimentation (denoxification). The sedimentation rates depend on PSC particle size with in turn is controlled by the composition and formation mechanism [2].

The following reaction is one of the most important heterogeneous reactions occurring on the surfaces of PSC's and transforming two abundant reservoirs of chlorine (HCl and $ClONO_2$) into Cl_2. Cl_2 is then photolyzed to yield atomic chlorine which catalyzes the ozone depletion mechanism.

$$HCl + ClONO_2 \longrightarrow Cl_2\,(g) + HNO_3\,(s) \qquad (1)$$

$$Cl_2 + h\nu \longrightarrow 2\,Cl \qquad (2)$$

Laboratory studies of reaction (1) have indicated that it proceeds with very high efficiency in the presence of ice [3], [4], [5], [6]. Other important reactions occurring on ice surfaces that lead to the release of active chlorine are those between HCl and HOCl [7], [8] and between N_2O_5 and HCl [9], [10]

$$HCl + HOCl \quad \longrightarrow \quad Cl_2\,(g) \; + \; H_2O\,(s) \qquad (3)$$

$$HCl + N_2O_5 \quad \longrightarrow \quad ClNO_2\,(g) \; + \; HNO_3\,(s) \qquad (4)$$

In order for the heterogeneous processes such as 1 and 3 to occur efficiently, at least one of the reactants needs to have a high affinity for the ice-like surface represented by PSC's. In this way, sequential collisions of the two gas phase reactants with the surface can lead to chemical reaction; a plausible mechanism can not involve simultaneous collision on the same active site. It is clear that HCl vapor has a high affinity for liquid water. Hydrogen chloride converts into hydrochloric acid, a process that is exothermic by about 18kcal/mol when the gas is dissolved in H_2O. However, studies of the liquid-solid partitioning of HCl in aqueous solutions have shown that only very small amounts of HCl are incorporated into the bulk ice phase; the reported partition coefficients range from 10^{-2} to 10^{-7} [11], [12], [13], [14], [15]. Although, it had once been suggested by Molina and coworkers that the ice surface takes up significantly larger amounts of HCl [16], [17], the measurements of Wolff et al. [18] indicate that HCl concentrates at grain boundaries as a consequence of the fact that the solubility of HCl in ice is small.

Several groups [8], [19] have reported that HCl leads to a large uptake of HCl by the ice surface at partial pressures around 10^{-5} Torr and above, but at pressures below about 10^{-6} Torr much smaller amounts are adsorbed, corresponding roughly to monolayer coverage or less. Experiments carried out by Molina and coworkers [17] have shown that the HCl partial pressure at the solid-liquid coexistence line, as represented in Figure 6.11, is what determines the nature of the uptake process. In fact, surface melting occurs if the partial pressure of HCl is above the coexistence line. They observe that a partial pressure of $5 \cdot 10^{-5}$ Torr leads to monolayer uptake at 250K. According to their findings, however, this same partial pressure leads to surface melting at 210K with subsequent higher uptake of HCl.

Furthermore, studies have appeared on the solubility and diffusion rate of HCl in ice [18], [20] and on the intrinsic surface properties of ice with respect to

HCl adsorption [21], [22], [23]. Moreover, Hynes used molecular dynamics simulations to study the ionization of HCl on an ice surface at 190K and calculated a change in free energy ranging from -5.8 to -6.7kcal/mol for the first step of the stepwise ionization mechanism [24].

So far however, nobody has attempted to measure the real time kinetics of HCl on ice which may elucidate the mechanistic role that structural phenomena such as grain boundaries and defects play. Using our method we are able to probe the dynamics of the ice surface in real time and thus assess the influence of surface structure and potential grain boundaries on the residence time of an HCl molecule on the surface of an ice particle.

6.1.1 Knudsen Cell Parameters and Sample Preparation

The following experiments were carried out using a teflonated glass reactor of $1890cm^3$ volume at ambient temperature. Together with a low temperature support having a cold surface of $15.2\ cm^2$, it yields a sample collision frequency ω of $90\ s^{-1}$. The diameters of the escape apertures are 4, 8 and 15 mm corresponding to k_e of 0.65, 2.0 and 5.6 s^{-1} (for HCl).

The ice sample was prepared according to the same protocol as in the preceding chapter, that is by applying freeze-pump-thaw cycles to bulk samples of about 5ml water ice. Using a slightly different technique samples were condensed rapidly at about 160K. The experiments were performed while an external flow of water was established in order to compensate for net evaporation so that the ice was in equilibrium with its gas phase. Within experimental uncertainties no difference in the kinetic parameters was observed as a function of sample type or water vapor equilibration. Moreover, no decrease of the water signal has been observed while the sample accumulates HCl, as expected according to Raoult's law.

The HCl gas sample was produced by the reaction between sulfuric acid and natrium chloride. Under vacuum, H_2SO_4 was dripped onto NaCl while the evolving HCl gas (containing water impurities) was trapped in a recipient cooled using liquid nitrogen.

6.2 Results

6.2.1 Steady State Experiments

Figure 6.1 shows four uptake experiments of HCl on water ice at 200K using the 4mm escape aperture. The upper two traces correspond to a high HCl flow of $1.9 \cdot 10^{15}$#/s and the lower two traces to a low flow of approximately $3.0 \cdot 10^{14}$#/s. At each flow, two uptake experiments on bulk ice were carried out, the first one on a fresh sample and the second one on that same sample after a melting/mixing cycle (annealing) to about 280K. Especially at the higher flowrate we observe that the first uptake is slower than the second one. Moreover, it immediately reaches a steady state level while the second one presents a delay before tending towards a steady state level. The mean value of the initial sticking coefficient γ_0 (taken for each pair of experiments at a low and a high flowrate) equals $0.81\pm0.04 \cdot 10^{-2}$ in the case of the fresh sample and $3.95\pm0.20 \cdot 10^{-2}$ in the case of the annealed sample.

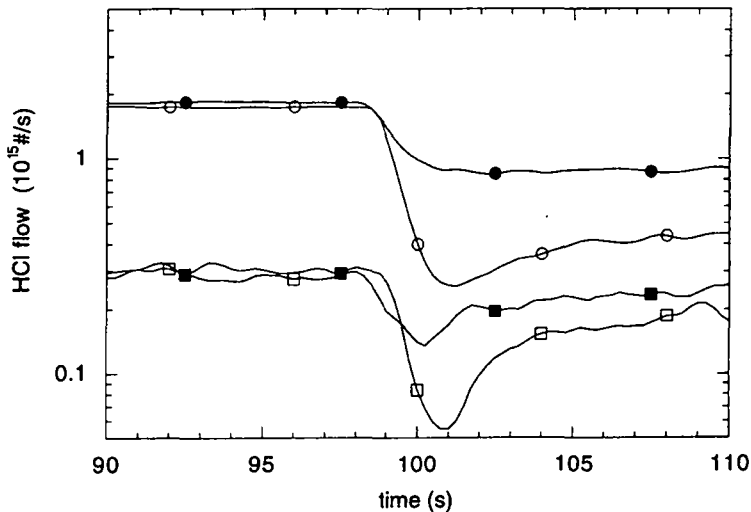**Figure 6.1:** Uptake experiments of HCl on fresh and regenerated water ice at 200K using a high ($1.9 \cdot 10^{15}$#/s) and a low ($3.0 \cdot 10^{14}$#/s) HCl flow. Traces labeled with full circles and squares correspond to uptake on a fresh sample, while the traces with open circles and squares correspond to uptake on samples annealed to about 280K.
Orifice: 4mm. Experiments 1&2 of 26 and 27 September 1995.

Apparently, γ_0 depends on the state of the surface but not on the HCl flow, that is its partial pressure. The pressure independence of γ_0 above 180K has been confirmed by five more experiments on fresh ice. The fact that γ_0 varies by a factor of five depending on the state of the sample surface shows that it is important to keep track of the accumulated dose of HCl on the ice surface. The accumulated dose prior to regeneration in the case of the high flow corresponds to 10^{17} molecules while in the second case (low flow) this dose amounts to $2 \cdot 10^{15}$ molecules. Taking the accumulated dose corresponding to the first case (10^{17} molecules) and assuming a bulk sample of approximately 5ml of water ($=0.275 mol = 1.7 \cdot 10^{23}$ molecules of H_2O) yields a fraction as low as 10^{-6} HCl per H_2O on a molecular basis. This number, as low as it may seem has a significant effect on the uptake characteristics of HCl on ice. Such an effect can only be explained by assuming that the previously accumulated HCl molecules do not homogeneously mix with the bulk molecules but probably remain at the boundary (respectively at the surface) of the ice sample.
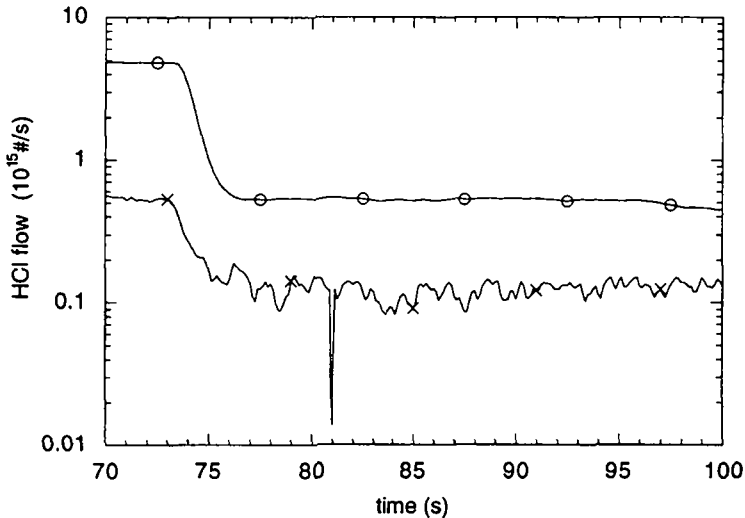

Figure 6.2: uptake experiments of HCl on fresh water ice at 180K using a high and a low HCl flow of $5.3 \cdot 10^{15}$#/s (open circles) and $5.6 \cdot 10^{14}$#/s (crosses) respectively. Experiments 1 of 28 September and 12 October 1995.

Figure 6.2 shows two uptake experiments of HCl on fresh ice samples at 180K. The upper trace corresponds to a high HCl flow of $5.3 \cdot 10^{15}$#/s and the lower one to a low flow of about $5.6 \cdot 10^{14}$#/s. At this temperature, the sticking coefficient γ appears to be dependent on the flow rate as opposed to the experiments performed at 200K (Figure 6.1). In fact, γ_0 varies by more than a factor of two from $2.4 \pm 0.2 \cdot 10^{-2}$ at a low flow to $6.1 \pm 0.2 \cdot 10^{-2}$ at a ten times higher flow. Moreover, the few experiments performed on annealed samples at 180K point towards the fact that the uptake at this temperature does not depend as much on the state of the bulk sample as at 200K. The positive pressure dependence in this case may be explained by surface melting induced by pressures of HCl exceeding the ones given by the coexistence line.

Figure 6.3 shows three reference experiments where the empty low temperature support was exposed to a constant flow of HCl. The uptake coefficients were measured at 200, 210 and 220K using flowrates of approximately $3 \cdot 10^{15}$#/s. Although saturating rapidly, the uptake on the copper dish is significant corresponding to $\gamma = 5.9 \cdot 10^{-3}$ at 200K, $\gamma = 3.0 \cdot 10^{-3}$ at 210K and $\gamma = 1.6 \cdot 10^{-3}$ at 220K.

Figure 6.3: Uptake experiments of HCl on unwaxed sample support containing no ice sample (reference experiments) at 200K (open circles), 210K (open triangles) and 220K (open squares). Escape aperture: 4mm. Experiments 1, 2&3 of 13 September 1995.

Clearly, the uptake decreases with increasing temperature and is practically irreversible, that is, upon reopening of the sample compartment at zero flow of HCl into the reactor, only a small quantity of HCl desorbs.

Figure 6.4 shows three reference experiments where the waxed low temperature support (using halocarbon wax) was exposed to a constant flow of HCl. The uptake coefficients were measured at 200, 210 and 220K using flowrates of approximately $1.8 \cdot 10^{15}$#/s. In this case, the uptake starts to saturate immediately and the signal increases to reach its initial level within a duration proportional to the uptake coefficient. These are of the same order of magnitude albeit significantly smaller than in the case of the bare copper dish corresponding to $\gamma = 3.2 \cdot 10^{-3}$ at 200K, $\gamma = 1.4 \cdot 10^{-3}$ at 210K and $\gamma = 4.0 \cdot 10^{-4}$ at 220K.

Hydrochloric acid has a vapor pressure of 760 Torr at 188.3K [26]. It is therefore surprising that we observe such a considerable uptake on an expectedly inert surface at a partial pressure of HCl in the mTorr range. One possible explanation may be that background water condenses on the low temperature support thus making possible the interaction with HCl.
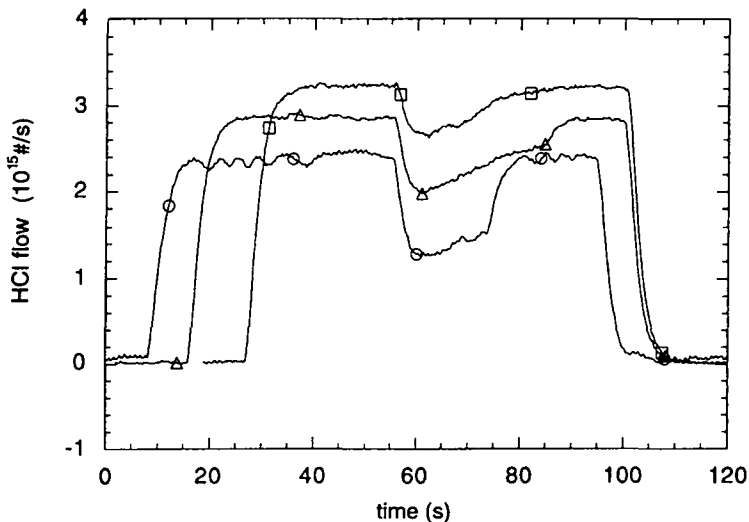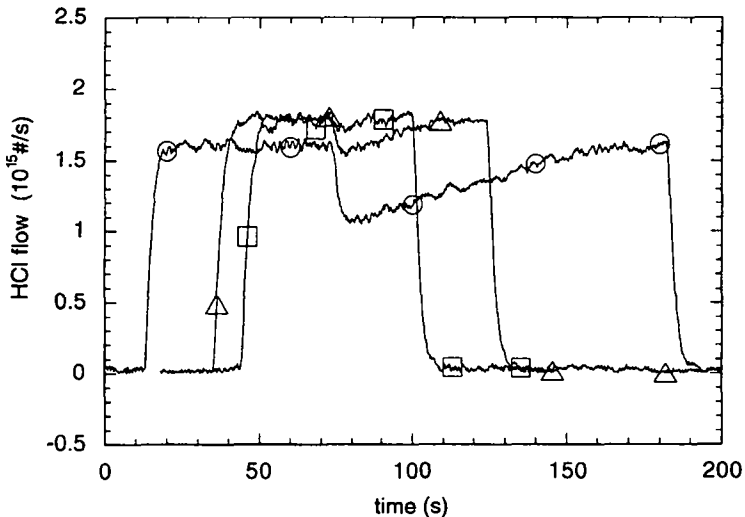

Figure 6.4: Uptake experiments of HCl on waxed sample support containing no ice sample (reference experiments) at 200K (open circles), 210K (open triangles) and 220K (open squares). Escape aperture: 4mm. Experiments 9, 10&12 of 13 September 1995.

For the uptake at 220 and 210K, the sample compartment was reopened at zero HCl flow at t=125s and t=145s, respectively, but no desorption of HCl could be observed. This corresponds thus to irreversible uptake of HCl on an unspecified internal surface. In a heat ramp experiment it has been observed that most of the adsorbed HCl will desorb only above 270K. Thus, HCl shows a non negligible interaction with halocarbon wax pointing towards a hysteresis behaviour of the adsorption as a function of temperature. This behaviour may possibly be enhanced due to the presence of water. As a consequence of this result we suggest that bare (not halocarbon wax coated) LTS should be used, particularly in experiments like the one displayed in Figure 6.5 in which a sample previously exposed to HCl and prepared by vapor deposition is evaporated in order to quantify its HCl content.

Figure 6.5 shows an uptake experiment at 200K on a condensed ice sample of $1.3 \cdot 10^{18}$ water molecules (in equilibrium with its gas phase). The idea of this experiment is to check the saturation of the ice sample as a function of HCl uptake. We assume that a change in uptake capability corresponds to a transition on the sample surface due to a variation in the HCl concentration.

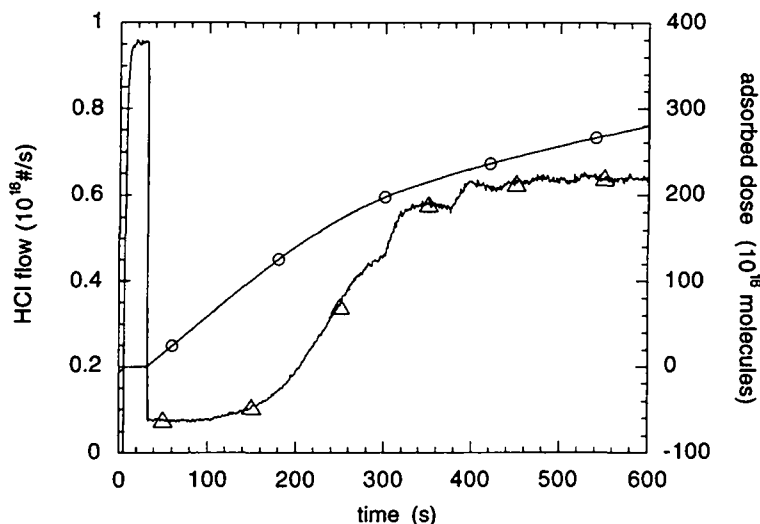**Figure 6.5:** Uptake experiment at 200K on a condensed ice sample of $1.3 \cdot 10^{18}$ water molecules. At t=35s the sample is exposed to an HCl flow of $9.5 \cdot 10^{15}$#/s (left hand ordinate, open triangles). At t=110s about $6 \cdot 10^{17}$ molecules of HCl have been incorporated (right hand ordinate, open circles). Escape aperture: 4mm. Experiment of 24 January 1996.

Beginning at t=35s the sample is exposed to a HCl flow of $9.5 \cdot 10^{15}$#/s (left hand ordinate, open triangles). The initial uptake corresponds to $\gamma = 8.8 \cdot 10^{-2}$. From t=110s to 400s the uptake decreases continuously to reach a value of $\gamma = 2.7 \cdot 10^{-3}$ (the small irregularities in the signal after t=300s are due to experimental problems with the temperature regulation of the LTS).

The right hand ordinate shows the dose of HCl adsorbed on the surface. When the change in uptake occurs at t=110s, about $6 \cdot 10^{17}$ molecules of HCl have been incorporated into the ice. This corresponds roughly to a sample concentration of 50% or dihydrate, $HCl \cdot 2H_2O$. When the new steady state uptake regime is reached at t=400s, the accumulated dose amounts to $2.3 \cdot 10^{18}$ molecules of HCl which is almost twice as much as the number of initially condensed water molecules. This corresponds to a mixture that exceeds even the concentration of monohydrate by almost 100% approaching the stoichiometric formula $2HCl \cdot H_2O$. The uptake reached at t=400s remains constant for at least 30 minutes and no further transition is observed (not shown in Figure 6.5). Unfortunately, such saturation experiments were not carried out systematically so that the statement about the different types of hydrates remains speculative.

6.2.2 Pulsed Valve Experiments

Pulsed valve experiments were carried out on ice samples at temperatures between 170 and 210K. The injected doses correspond to instantaneous HCl partial pressures in the range 10^{-6} to 10^{-3} Torr. The upper limit of the temperature as well as of the dose range is given by the Knudsen condition. This condition requires that the molecule's mean free path at a given total pressure of H_2O and HCl in the Knudsen cell is at least a factor of 3 larger than the orifice diameter.

Figure 6.6 a: pulsed valve experiment using an ice sample at 200K. The decay of the HCl signal is followed for three different doses: $3.6 \cdot 10^{14}$ molecules (open circles), $3.3 \cdot 10^{15}$ molecules (open squares) and $1.1 \cdot 10^{16}$ molecules (open triangles). As the dose increases, the decay starts to form a plateau tending towards a steady state level for the highest injected dose. Escape aperture: 15mm. Experiments 2 of 14 December 1995 and 1&7 of 23 January 1996.

Figure 6.6 a shows pulsed valve experiments in which three doses of HCl varying over two orders of magnitude are interacting with ice at 200K. We observe the formation of a plateau as a function of increasing dose. Moreover, this plateau always forms at the same level of HCl flow. As this level remains practically stable for a few seconds for a sufficiently high dose, we refer to it as

steady state level. After a duration proportional to the injected dose, the signal decreases to its initial background level. In fact, the steady state level is stable using the 4 and 8mm orifice while it decreases slightly when using the 15mm orifice (compare Figures 6.6 a and b).

Figure 6.6 b shows three pulsed valve experiments in which the steady state level is apparent using different reactor orifices. The first two pulses are performed using the 4 mm orifice while the third one corresponds to an experiment using the 8 mm orifice. We observe that in the case of the 8 mm orifice, the steady state level is larger by almost a factor of three compared to the case of the 4 mm orifice. It is part of the special feature of these experiments that the steady state level takes on a specific value for a given set of temperature and orifice size, regardless of the dose or pulse length.
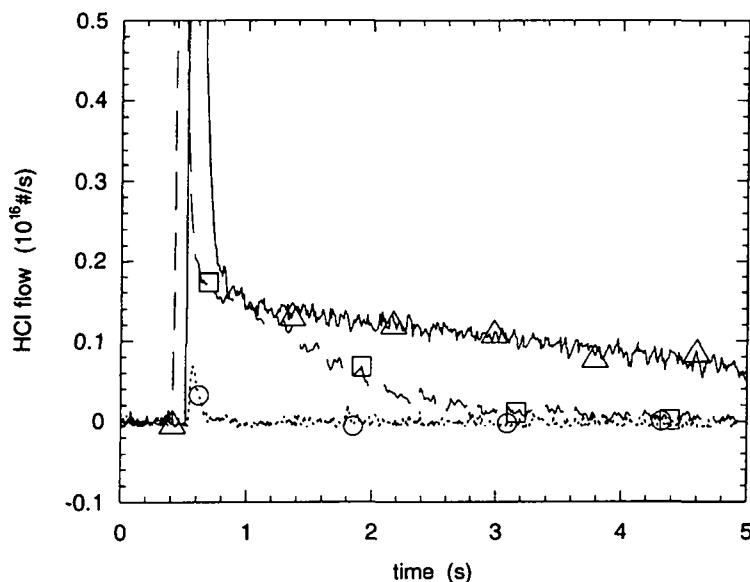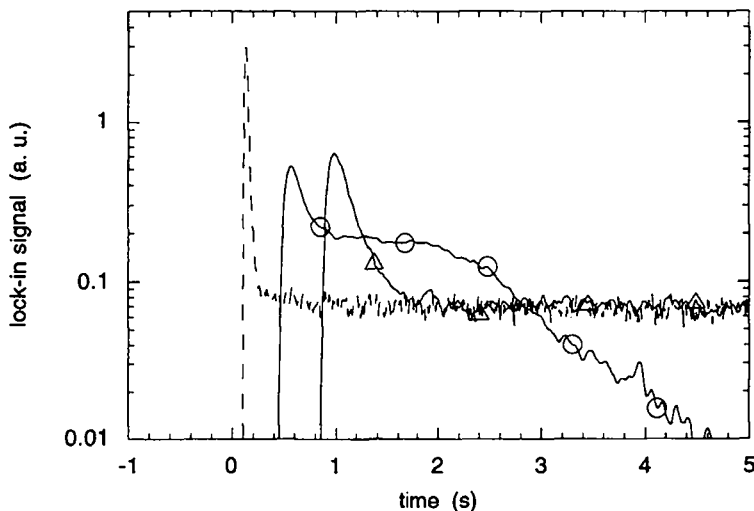

Figure 6.6 b: Pulsed valve experiment using an ice sample at 210K. The decay of the HCl signal is followed using two different escape apertures. The first and the third pulse are performed using the 4mm orifice (dashed line and line with triangles) while the second one corresponds to an experiment using the 8mm orifice (line with open circles). The respective doses correspond to $2.1 \cdot 10^{17}$, $2.1 \cdot 10^{16}$ and $6.5 \cdot 10^{15}$ molecules. First experiments of 7, 14 and 21 November 1995.

Moreover, from data such as presented in Figure 6.6 b we note that the decay of the pulses is of single exponential type corresponding to a decay constant k_{eff}. If

the steady state level appears, the determination of k_{eff} was performed with respect to this steady state level.

It is natural to address the question whether there exists a dose threshold above which a steady state level forms. As the sample characteristics change as a function of accumulated dose of HCl as observed during preceding steady state experiments (see Figure 6.1), it is difficult to determine such a dose threshold. **Figure 6.7** shows values of k_{eff} versus injected dose distinguishing between experiments where the steady state level is formed and where it is not, as a function of temperature. Due to the relatively large scatter in k_{eff} determined using the 4 mm orifice reactor, only k_{eff} corresponding to the 8 and 15 mm reactor orifice are displayed. After filtering in this manner and also taking into account the data at 190K, a threshold may tentatively be located at $8\pm2\cdot10^{14}$ molecules of injected HCl (dotted line). By analogy to the calculation for H_2O presented in Chapter 4, the sample surface 15.2 cm^2 corresponds to a formal monolayer of $3.6\cdot10^{15}$ molecules of HCl. In fact, a 20% wt solution of HCl coexisting with ice at 220K has a density of $1.1\,gcm^{-3}$ [26] corresponding to

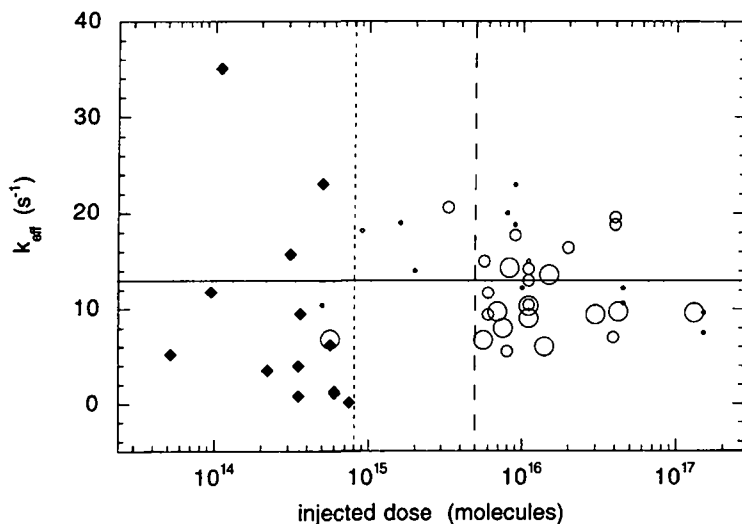**Figure 6.7:** Plot of k_{eff} vs. dose in order to determine the threshold above which the steady state level forms. Diamonds correspond to experiments not forming the steady state level (T=190 to 210K) while the open circles represent experiments forming a steady state level (small circles = 190K, medium circles = 200K and large circles = 210K). A dose threshold may be placed at $8\pm2\cdot10^{14}$ of injected molecules.

0.22/36·6.03·10^{23} equal to 3.67·10^{21} molecules of HCl in a cube of 1cm^3. Consequently, the formal monolayer is calculated as 15.2·[3.67·10^{21}]$^{2/3}$ = 3.6·10^{15} molecules of HCl on the sample surface in question. Thus, a threshold of 8±2·10^{14} molecules corresponds to about 22% of a formal monolayer of the 20% wt solution (3.6·10^{15} molecules of HCl) or an instantaneous partial pressure of HCl of 1.3·10^{-5} Torr in the reactor. This value is twice as high as the observed vapor pressure given by a solution of approximately 23% wt coexisting with ice at 200K (0.7·10^{-5}Torr) [25].

Moreover, we might expect the dose threshold to present a similar temperature dependence as the steady state levels. A pulse whose peak amplitude remains below the characteristic steady state level obviously can not give rise to such a level. However, the displayed experiments below the dose threshold do not present any observable temperature dependence. If we look for such a temperature dependence of experiments forming a steady state level, we see that only one point of the experiments at 200 and 210K lies below 5·10^{15} of injected molecules (see dashed line in Figure 6.7). Obviously, this value must be considered as the upper limit of the dose threshold at 210K. It corresponds to an instantaneous pressure of 8.3·10^{-5} Torr which is five times larger than the vapor pressure of the liquid solution (≈23%wt) forming at 210K (1.7·10^{-5} Torr). Thus, regarding the potential temperature dependence of the dose threshold, we suggest it to vary from 8·10^{14} to 5·10^{15} of injected molecules over the temperature range of 190 to 210K.

Furthermore, Figure 6.7 shows that the k_{eff} below the suggested threshold of 8·10^{14} molecules are highly scattered between 0.1 and 25s^{-1}, while the ones above threshold all lie around a value of 13±8s^{-1}, which may be explained by a more consistent characterization of the surface as soon as the solution is formed, while the surface is in an ill defined state in the case of pulses not forming the solution. This furthermore means that k_{eff} is not significantly dependent on the injected dose in the case where the steady state level is formed, while the investigated range of doses for the experiments below the threshold is too small to be conclusive.

One of the reasons why it is difficult to determine a dose threshold is presented in **Figure 6.8**: This figure shows pulsed valve experiments where a small dose of 5.0·10^{14} molecules corresponding to14% of a formal monolayer is injected over decreasing time intervals. The first pulse in a time series exponentially decreases to its initial background level, while the second one already decays back to a certain level. From the forth pulse on, a steady state level is formed which persists if the surface is "charged" continuously with

additional pulses of HCl. This experiment shows that even a dose below the threshold can form a steady state level if the pulses are repeated at a sufficiently high frequency. Assuming that the adsorbed molecules diffuse from the surface into the bulk along grain boundaries or hairline cracks, we may interpret this phenomenon by the occurrence of a bottleneck: When the accumulated dose of molecules at the surface becomes too large with respect to diffusion into the bulk, they are forced to wait on the surface with the possibility of desorbing back into the gas phase.
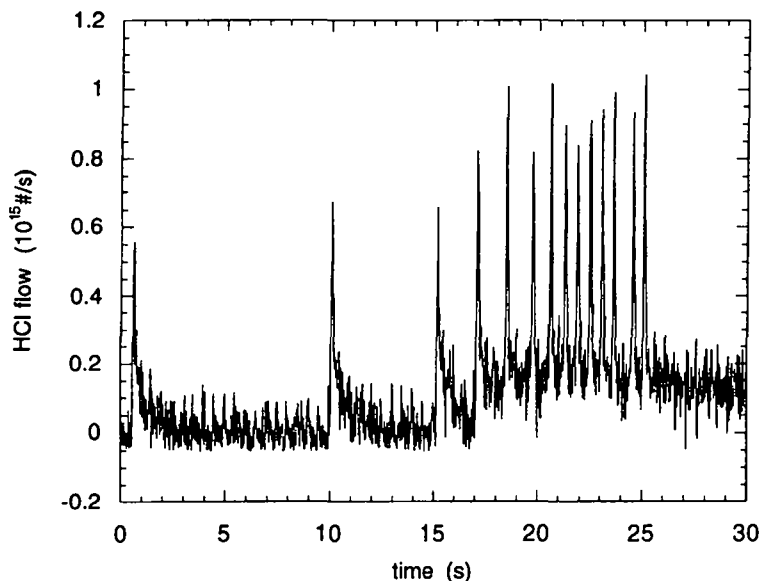
Figure 6.8: Consecutive pulsed valve experiments on ice at 190K using the 8mm reactor orifice. A steady state level forms when several small doses of $5 \cdot 10^{14}$ molecules are injected within a short time period. Experiment 3 of 5 March 1996.

It is necessary to address the question whether there is a difference in the k_{eff} measured on (a) a fresh ice surface, (b) a previously exposed ice surface with a given background level of HCl and (c) a surface forming a steady state level of desorbing HCl. In **Figure 6.9** we present the cases (b) and (c) while the case (a) is discussed in the next Chapter 6.3. The displayed pulse of $5.6 \cdot 10^{14}$ molecules on the background level at t=25.5 s is the fifth (lower trace) of a series of small pulses that slightly charged the surface. The same pulse is displayed on a

logarithmic scale in the zoom window on the right hand side (first pulse) and yields a k_{dec}=11.8±1 s^{-1} leading to k_{eff}=11.8-5.6=6.2±1 s^{-1} (k_{eff}=5.6 s^{-1}). The second pulse displayed in the same zoom window (dashed line) of k_{dec}=12.4±1 s^{-1} corresponds to the small pulse at t=27 s on the steady state level (3.5·10^{15}#/s) formed by the six preceding pulses (upper trace), each one consisting of 1.5·10^{16} molecules. From the two linear semi-logarithmic fits we draw the conclusion that within the experimental uncertainty of the measurement of k_{dec}, our method of surface probing does not detect a significant difference between a surface slightly charged with HCl (leading to a background level after desorption) and a surface with concomitant HCl desorption corresponding to a steady state level.
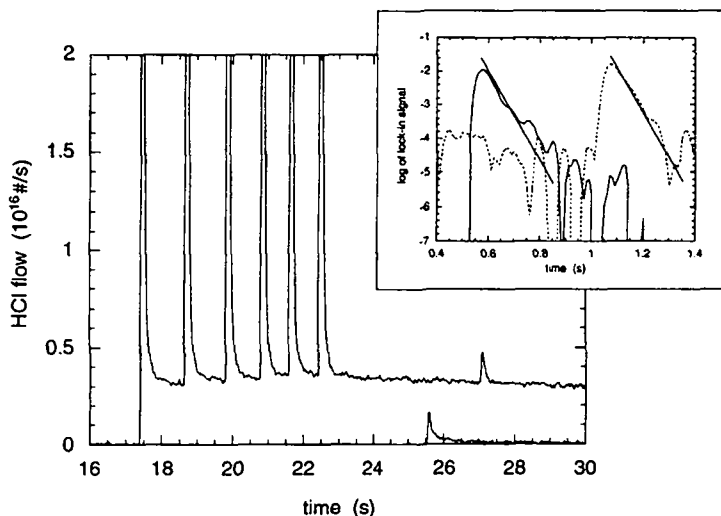
Figure 6.9: Comparison of a small dose pulse performed once on the background level (lower trace) and once on the steady state level (upper trace) using a previously exposed ice surface at 210K. The same pulses with their linear fits are displayed on a logarithmic scale in the zoom window (right hand side) and yield k_{dec}=11.8±1s^{-1} and k_{dec}=12.4±1s^{-1} respectively. Escape aperture: 15mm. Experiments 5&8 of 30 January 1996.

6.3 Discussion

As far as the pulsed valve experiments are concerned, we have two types of experimental observables which are the steady state levels characteristic of a certain orifice and temperature as well as the k_{eff} corresponding to the single exponential decay of a pulse. Consequently, we chose two different viewpoints to analyze the data. In the case where a steady state level is formed we apply the two state model presented in Chapter 5, while the decays given by k_{eff} are analyzed as a function of the different surface parameters like previous exposure and temperature.

6.3.1 Analysis of the Steady State Levels formed in Pulsed Valve Experiments

For the system HCl on ice the two state adsorption Scheme presented earlier (Chapter 5.2) is as follows:

$$\text{MS detection} \quad \xleftarrow{\quad k_e \quad} \quad \text{HCl (g)} \quad \underset{F_{ev}}{\overset{k_{ads}}{\rightleftharpoons}} \quad \text{HCl (ads)} \qquad (5)$$
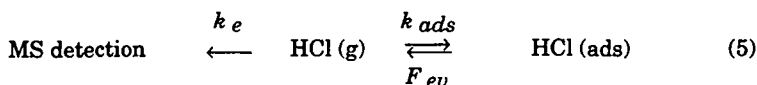
where k_e and k_{ads} are the unimolecular rate constants for the escape and the adsorption process respectively, while F_{ev} is the net flow of evaporation of HCl from the sample surface in units of molecules per second.

In analogy to the case of condensation of water vapor onto ice, the pair of steady state levels F^L and F^S (superscripts L for large and S for small orifice) allows us to write two independent steady state equations which can be solved for k_{ads} and F_{ev}:

$$k_{ads} = \frac{k_e^L \, k_e^S (r^{\frac{1}{3}} - 1)}{k_e^L - k_e^S \, r^{\frac{1}{3}}} \qquad (6) \qquad \text{and} \qquad F_{ev} = F^L \frac{k_e^L - k_e^S}{k_e^L - k_e^S \, r^{\frac{1}{3}}} \qquad (7)$$

where $\quad r^{\frac{1}{3}} = \dfrac{F^L}{F^S} \quad$ is the ratio of the two steady state levels. Moreover, an

equilibrium vapor pressure can be calculated as: $\quad \dfrac{G_{eq}}{V} = [G]_{eq} = p_{eq} = \dfrac{F_{ev}}{V k_c} = \dfrac{R_{ev}}{k_c}$

where R_{ev} is the rate of evaporation from the sample surface in units of $\#cm^{-3}s^{-1}$.

The experimental values of the steady state levels observed over the temperature range 180 to 220K together with their respective least squares fit are plotted in semi-logarithmic fashion in **Figure 6.10**. The values of F^L, F^M and F^S (superscript M for medium size orifice) used to calculate k_{ads}, F_{ev} and p_{eq} as presented in **Table 1.a and b** correspond to the linear least squares fits of the 15, 8 and 4 mm orifice data plotted on a logarithmic scale. Moreover, the values of F^L and F^M at 220K as well as the one for F^S at 180K are extrapolated according to these fits.
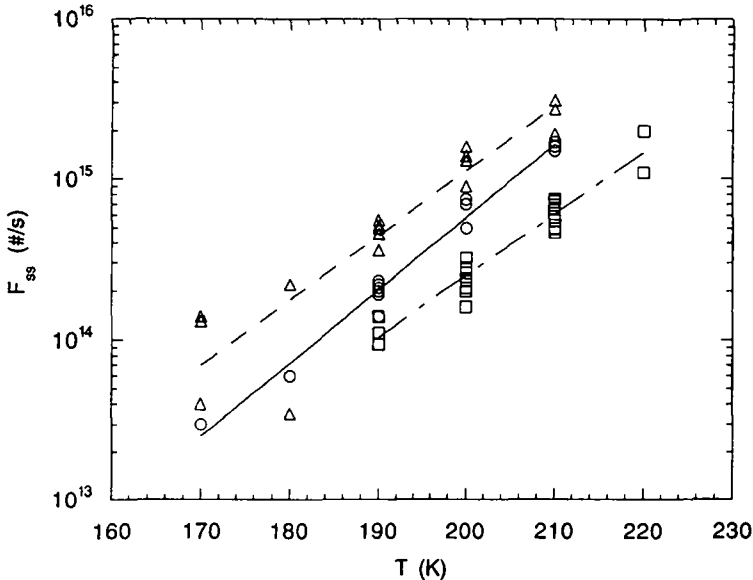
Figure 6.10: F_{ss} vs. temperature measured in pulsed valve experiments using three different escape apertures. The dashed line is the exponential fit corresponding to experiments using the 15 mm orifice (open triangles) given by $1.0 \cdot 10^7 * \exp(0.093 \cdot T)$. The solid line is the fit to experiments using the 8 mm orifice (open circles) given by $5.0 \cdot 10^5 * \exp(0.104 \cdot T)$, while the experiments using the 4 mm orifice (open squares) are fitted by $5.3 \cdot 10^6 * \exp(0.088 \cdot T)$.

As shown previously, $r^{L/S} = \dfrac{F^L}{F^S}$ must take a value in the interval between 1 and $k_e^L / k_e^S = 8.8$. Moreover, we need a value which does not approach either one of the limits to ascertain that the experimental yardstick is of the same order as the kinetic parameter to be determined. This is fulfilled in the case presented in

Table 6.1 a where k_{ads}, F_{ev} and $[G]_{eq}$ are calculated using the steady state levels corresponding to the 4 and 15 mm escape apertures, and we can thus expect an accurate measurement of the mentioned parameters. The rate constant of adsorption k_{ads} increases from 5.0 s⁻¹ at 180K to 8.5 s⁻¹ at 220K corresponding to a small activation energy of 1.0 kcal/mol, while the flow of evaporation F_{ev} increases in the same temperature range from $3.5 \cdot 10^{14}$#/s to $19.3 \cdot 10^{15}$#/s equivalent to an activation energy of 7.9kcal/mol. The values of F_{ev} pertain to the whole sample surface of 15.2 cm² which for a 20% wt solution of HCl is assimilated to a formal monolayer of $3.6 \cdot 10^{15}$ molecules of HCl (see Figure 6.7). Thus, $F_{ev} = 19.3 10^{15}$#/s at 220K corresponds to 5.4 monolayers of dissolved HCl evaporating per second. This number is much smaller than the number of monolayers of H₂O evaporating from pure ice at the same temperature (~500ML s⁻¹). On the other hand, comparing the dose threshold of $8 \cdot 10^{14}$ molecules to a formal monolayer of the 20% wt solution leads to the conclusion that a liquid is formed for an injected dose corresponding to a fraction of a monolayer. We are thus suggesting the formation of domains of solution on the ice surface without the necessity to form a coherent liquid layer across the entire sample surface.

Table 6.1 a: Calculation of k_{ads}, F_{ev} and p_{eq} by means of fitted F_{ss} using data corresponding to the 4 and 15mm orifice reactor.

temp K	fitted values of F^S a) $10(15)$#/s	fitted values of F^L a) $10(15)$#/s	$r^{L/S} = \dfrac{F^L}{F^S}$	k_{ads} s⁻¹	F_{ev} $10(15)$#/s	p_{eq} Torr
180	0.040	0.19	4.6	5.0	0.35	$1.2 \cdot 10^{-6}$
190	0.097	0.47	4.9	5.6	0.94	$2.9 \cdot 10^{-6}$
200	0.23	1.2	5.1	6.4	2.6	$6.8 \cdot 10^{-6}$
210	0.56	3.0	5.4	7.3	7.0	$1.6 \cdot 10^{-5}$
220	1.4	7.7	5.7	8.5	19.3	$3.9 \cdot 10^{-5}$

a) F^S and F^L correspond to the fitted values (see Fig. 6.10) of the HCl flow rates out of the reactor at steady state for the 4 and 15 mm orifice, respectively.

On the other hand, $r^{L/M} = \dfrac{F^L}{F^M}$ approaches $k_e^L / k_e^M = 2.8$ for lower temperatures and therefore the measurement of the mentioned parameters is less accurate (even impossible at 180K) in the case presented in **Table 6.1 b**, where k_{ads}, F_{ev} and $[G]_{eq}$ are calculated using the steady state levels corresponding to the 8 and

15 mm escape apertures. The rate constant of adsorption k_{ads} decreases from 25.3 s^{-1} at 190K to 4.3 s^{-1} at 220K corresponding to a negative activation energy of -4.9kcal/mol, while the flow of evaporation F_{ev} increases in the same temperature range from $2.6 \cdot 10^{14}$#/s to $13.5 \cdot 10^{15}$#/s equivalent to an activation energy of 4.6 kcal/mol. In spite of the important negative activation energy, the values of k_{ads} displayed in Table 6.1 b appear to agree better with the values of k_{eff} found in pulsed valve experiments where the steady state level is formed (see Figure 6.13) compared to the ones of Table 6.1.a which are too small by a factor of two. While the kinetic parameters k_{ads} and F_{ev} determined using two different orifice combinations are varying up to a factor of five (for example k_{ads} at 190K), the equilibrium vapor pressure is equal in both cases within less than a factor of two. This is also valid calculating the equilibrium vapor pressure by combining the 8 (M) and the 4 mm (S) orifice data. In summary, the determination of k_{ads} and F_{ev} according to the two state adsorption scheme (5) is very sensitive with respect to the choice of the orifice combination. However, the above method allows one to calculate an equilibrium vapor pressure and thus to determine the composition and the state of the surface in a consistent manner.

Table 6.1 b: Calculation of k_{ads}, F_{ev} and p_{eq} by means of fitted F_{ss} using data corresponding to the 8 and 15 mm orifice reactor.

temp K	fitted values of F^M 10(15)#/s	fitted values of F^L 10(15)#/s	$r^{L/M} = \dfrac{F^L}{F^M}$	k_{ads} s^{-1}	F_{ev} 10(15)#/s	p_{eq} Torr
190	0.19	0.47	2.5	25.3	2.6	$1.8 \cdot 10^{-6}$
200	0.54	1.2	2.2	11.7	3.7	$5.4 \cdot 10^{-6}$
210	1.5	3.0	2.0	6.8	6.7	$1.7 \cdot 10^{-5}$
220	4.3	7.7	1.8	4.3	13.5	$5.4 \cdot 10^{-5}$

a) F^M and F^L correspond to the fitted values (see Fig. 6.10) of the HCl flow rates out of the reactor at steady state for the 8 and 15 mm orifice, respectively.

Plotting the values of $[G]_{eq}$ in the phase diagram (**Figure 6.11**) established by Molina and coworkers [17], [25] shows that the equilibrium vapor pressure displayed in **Table 6.1 a and b** falls on the coexistence line of ice and the corresponding solution within experimental uncertainty. This leads to the conclusion that the observed steady state level originates from the evaporation of a solution of HCl that is formed immediately after injection of the pulse. Moreover, at each temperature a solution of a specific concentration is formed
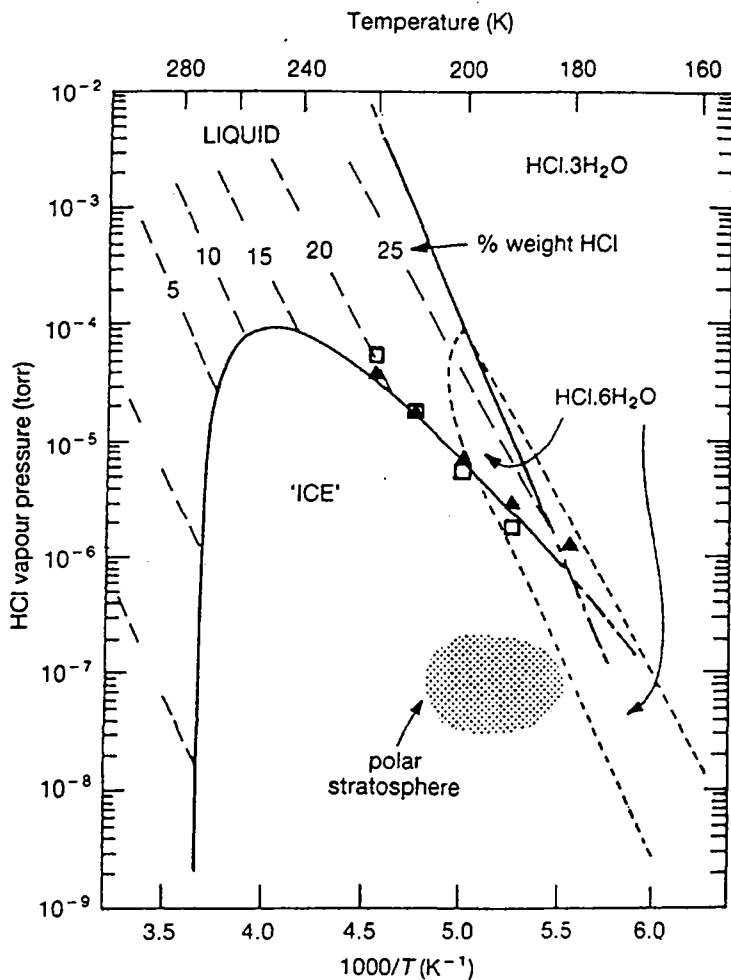
Figure 6.11: HCl vapor pressures as a function of temperature for the HCl/H_2O system according to Molina and coworkers [25]. The solid lines represent two-phase coexistence conditions. The dashed lines give vapor pressure for liquids whose composition is given in % weight HCl. The dotted lines enclose the region of thermodynamic stability for HCl hexahydrate. Triangles and squares mark our measurements of p_{eq} over ice-liquid equilibrium mixtures according to Table 6.1 a and b, respectively.

spontaneously. As the steady state levels are independent of the injected dose as shown in **Figure 6.6 a**, we assume the formation of a quasi liquid layer whose thickness is proportional to the dose as the concentration is given by the temperature. As there is no external HCl flow to compensate for evaporation, the solution evaporates completely with time. The eutectic point being at 186K [28], we have to assume that the steady state levels observed below 186K must correspond to a supercooled liquid as observed in various experiments by Hanson and Mauersberger [15].

6.3.2 Analysis of k_{eff} determined in Pulsed Valve Experiments as a Function of the State of the Surface at 170 and 180K

In order to make an accurate interpretation of k_{eff}, we obviously have to answer the question whether the liquid layer as mentioned above is formed or not when a burst of HCl interacts with the ice surface. Moreover, we have to account for the accumulated dose of HCl on the surface. Therefore, a simple classification
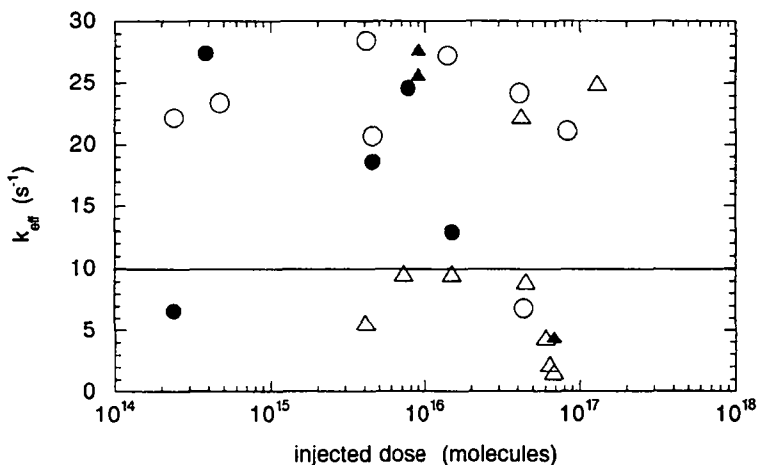
Figure 6.12: k_{eff} vs. dose at 170 and 180K as a function of the state of the surface The symbols correspond to experiments where a steady state level is formed (triangles) and where it is not (circles). The open symbols correspond to experiments on a previously exposed sample while the closed symbols represent experiments on a fresh ice surface. Escape apertures are confounded.

scheme for data analysis is to divide the experiments into 4 groups: two groups on a fresh sample (first uptake), one where the steady state level is formed, the other where there is no observable steady state level, and the two respective groups on a previously exposed sample having an accumulated dose of HCl. As we have determined an approximate dose threshold of $8\pm2\cdot10^{14}$ molecules at 190K, it may seem reasonable to state that the experiments in which the steady state level is observed correspond to experiments whose dose lies above the threshold. The experiment presented in Figure 6.8, however, shows that the dose itself is not a sufficiently decisive criterion to discriminate between experiments forming or not a liquid layer. In general, *no systematic pressure dependence of* k_{eff} has been observed apart from the fact that a quasi liquid layer is formed for injected doses above threshold, i.e. k_{eff} neither depends solely on dose nor escape aperture size. On the other hand, we have to exclude the measurements below 186K from these groups, because they seem to behave differently as shown in **Figure 6.12**. This Figure presents k_{eff} versus dose using different symbols to account for the state of the surface at 170 and 180K. At these temperatures we reach the detection limit for HCl evaporating from the surface. Depending on the reactor orifice, it is very difficult to observe a steady state level. Moreover, these two investigated temperatures are below the eutectic point of 186K [28] and the parameters leading to the formation of a supercooled liquid have not been studied so far. Most points are available for the case where the steady state is not observed. Except for one point, they all have high values. Omitting any classification, we have fifteen points which lie above $k_{eff}=10s^{-1}$ (mean value $23.4\pm4.1\ s^{-1}$) and ten points lying below this value (mean value $6.0\pm2.9\ s^{-1}$). Among the points corresponding to first exposure (fresh ice sample, filled symbols), there are six points lying above $k_{eff}=10s^{-1}$ while two points fall below this limit. Considering the first group of these points pertaining to first exposure experiments, k_{eff} takes a mean value of 23.4 s^{-1} which is clearly higher than the one for temperatures above 180K (see following Figures). On the other hand, it does not seem that these observed high values are only due to the formation of a liquid layer with subsequent acceleration of the uptake as shown in Figure 6.15 for temperatures above 186K, because many experiments on a previously exposed ice surface also show high values of k_{eff} thus excluding any acceleration effects.

6.3.3 Analysis of k_{eff} determined in Pulsed Valve Experiments as a Function of the State of the Surface between 190 and 210K

The following three Figures (6.13 to 6.15) show k_{eff} over the temperature range of 190 to 210K. In each Figure we compare two different sets of data in the order given below. Note that an identical set of data may appear in two Figures:

Figure 6.13: comparison between experiments on fresh and previously exposed samples, while the formation of the steady state level is observed.

Figure 6.14: comparison between experiments on fresh and previously exposed samples, while the steady state level is <u>not</u> formed.

Figure 6.15: experiments on a fresh sample distinguishing between cases in which the steady state level is formed or not.

Figure 6.13 presents a comparison between k_{eff} of the two sets in which the steady state level is formed, once on a fresh and once on a previously exposed sample. We observe in both cases k_{eff} to decrease from about 15 s^{-1} at 190K to 10 s^{-1} at 210K. The difference in the values of k_{eff} between both groups is not significant. As we have a relatively large number of data available for this
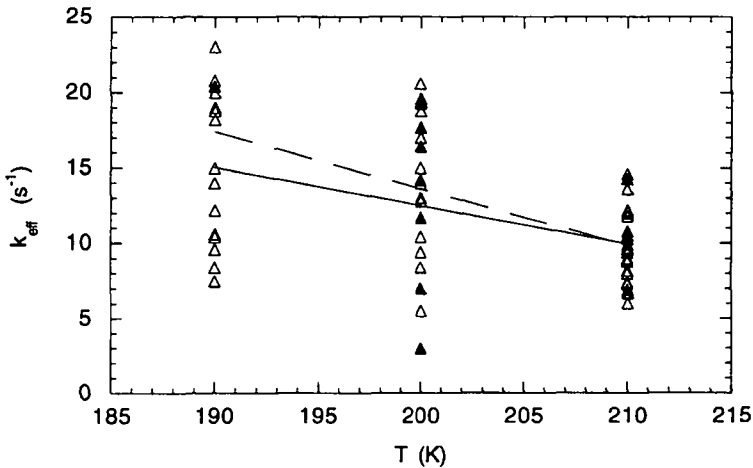
Figure 6.13: k_{eff} over the temperature range 190 to 210K for which a steady state level is formed. The open triangles represent experiments on a previously exposed ice surface (fitted by the solid line) while the filled triangles correspond to experiments on a fresh ice sample (fitted by the dashed line).

comparison, we may conclude with some certainty that for the uptake
experiments in which the liquid layer is formed, k_{eff} is independent of the
previously accumulated dose. The activation energy for the experiments on a
previously exposed sample is equal to -1.6±0.7 kcal/mol and is only slightly
higher for the experiments on a fresh sample. Assuming immediate formation of
the liquid layer in the case of steady state experiments (for a HCl flowrate of at
least 10^{15}#/s), we may compare these values for k_{eff} to the ones obtained by
Flueckiger [27] for k_{uni} in steady state experiments using the 15 mm escape
aperture. He observed values of k_{uni} varying from 12 to 23 s^{-1} in the temperature
range between 180 and 210K corresponding to a negative activation energy of
-1.9±0.25 kcal/mol. Within the experimental uncertainty, this activation energy
is equal to the one of -1.6±0.7 kcal/mol determined for the data presented in
Figure 6.13. As this Figure corresponds to experiments in which a solution is
formed, we may compare this activation energy to the one of k_{ads}, although it
appears that the calculation of k_{ads} according to equation 6 is not an accurate
measurement of the rate of adsorption. The activation energy of k_{ads} varies
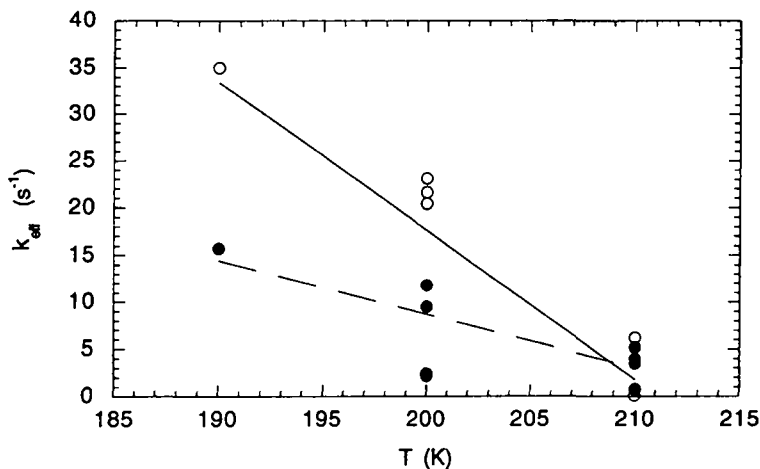
Figure 6.14: k_{eff} over the temperature range 190 to 210K for uptake
experiments without formation of a steady state level. The open circles
represent experiments on a previously exposed ice surface (fitted by
the solid line) while the filled dots correspond to experiments on a
fresh ice sample (fitted by the dashed line). Doses and escape
apertures are confounded.

between -4.5 and +1.0 kcal/mol depending on the choice of data set displayed in Table 6.1 a and 6.1 b. Therefore we have the result that the activation energy observed in pulsed valve experiments lies in the middle of this range, on the order of -1.6±0.7 kcal/mol. This conclusion is less certain if we compare the values of k_{eff} for the two sets where the steady state level is not formed, as presented in **Figure 6.14** due to the smaller number of experiments. In fact, for the two temperatures below 210K, k_{eff} takes higher values in the case of a previously exposed surface than in the one of a fresh sample (first uptake). For this plot we have only one point available for each group at 190K, and therefore, no conclusion can be drawn as far as the activation energy is concerned. Moreover, the scatter at 200K is significant, especially for the experiments on a previously exposed sample where k_{eff} takes values varying over an order of magnitude from 2.2 to 23 s^{-1}. At 210K we observe less scatter in the data, and the values of k_{eff} are approximately the same in both cases, but approximately 5 s^{-1} smaller than in Figure 6.13.
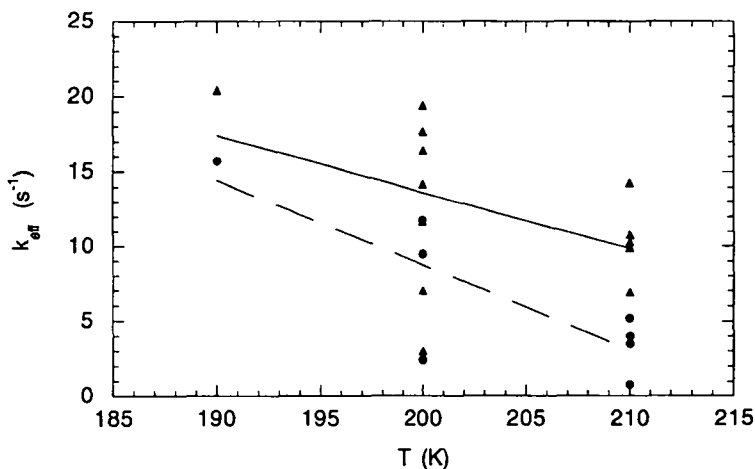
Figure 6.15: k_{eff} over the temperature range 190 to 210K for uptake experiments on a fresh ice sample where we distinguish experiments with and without formation of a steady state level (filled dots, solid line: no observation of a steady state level; filled triangles, dashed line: observation of a steady state level). Doses and escape apertures are confounded.

As far as the comparison between first uptake experiments is concerned (**Figure 6.15**), we observe a significantly stronger temperature dependence than

in Figure 6.13, with k_{eff} varying between 3 and 15 s^{-1} in the case where no solution is formed and between 10 and 20 s^{-1} for the uptake on the solution. Moreover, the values of k_{eff} observed in uptake experiments on a liquid layer (formation of a steady state level) are larger by approximately 5 s^{-1} compared to the ones without formation of a steady state level. Once again, the scatter is largest at 200K where most data are available, while we have only one point per group at 190K, and therefore, no conclusion can be drawn as far as the activation energy is concerned.

In summary, for the experiments on the solution layer (corresponding to the formation of a steady state level) we observe a negative temperature dependence of k_{eff} varying from 10 to 17 s^{-1} in the temperature range between 190 and 210K. This temperature dependence is independent of the previously accumulated dose of HCl and corresponds to a negative activation energy of -1.6±0.7 kcal/mol. The experiments without formation of a steady state level present an even stronger negative temperature dependence although the data are more scattered than in the preceding case. This may indicate a stronger influence of the substrate properties on the kinetics. On the other hand, in the case of uptake experiments on a fresh sample, it appears that the values of k_{eff} observed without formation of a steady state level are lower by 5 s^{-1} compared to the case in which the steady state level is formed. In the group of experiments on previously exposed samples with and without formation of the steady state level there has no difference been observed in k_{eff} for uptake experiments on the steady state or background level (see Figure 6.9).

As far as the activation energy in the temperature range of 190 to 210K is concerned, we observe a negative activation energy for all the four groups under consideration. While the two groups of uptake experiments on the solution yield an activation energy of -1.6±0.7 kcal/mol, the group of uptake experiments on fresh samples (first uptake) not forming the steady state level has a stronger activation energy of -7.0 kcal/mol. On the other hand, the group of experiments on previously exposed samples in which the liquid layer does not form consists of too few points to be conclusive.

6.3.4 Reversibility of HCl uptake determined in Pulsed Valve Experiments in the temperature range of 190 to 210K

The reversibility of the uptake of HCl on ice is assessed using pulsed valve experiments. In fact, we used the fraction of adsorbed molecules staying in the sample in relation to the injected dose as a measurement of the reversibility. That is, the higher the fraction of permanently adsorbed molecules is, the lower is the reversibility. In general, the fraction of adsorbed molecules is determined as the difference between the injected dose and the number of molecules which have left the cell after a certain time.

In the case of experiments not forming a steady state level, the number of effusing molecules is inversely proportional to $k_{dec}=k_e+k_{eff}$. In fact, this number may be determined analytically by the integral of the exponential decay corresponding to k_{dec}. Within our detection limit of $2\pm1\cdot10^{14}$#/s, such pulses always relax back to their initial background level which we assume to be the baseline. On the other hand, in the case of the experiments where we observe the formation of a steady state level, the number of effusing molecules must be determined by taking the integral of the flow out of the reactor over a time period at least as long as the steady state level persists.
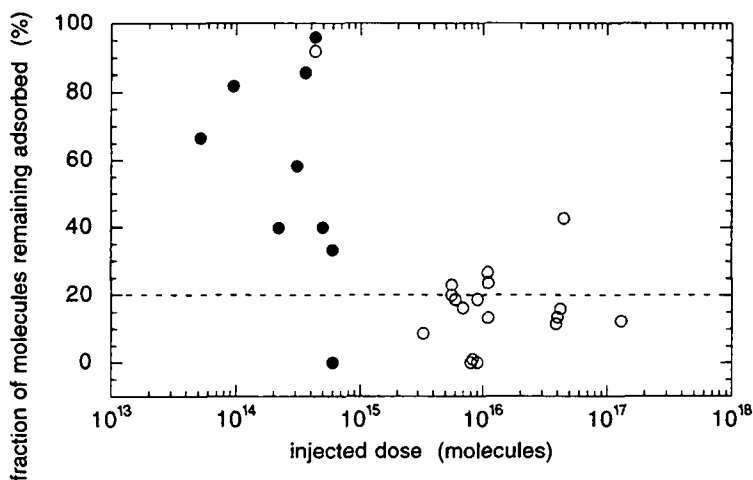
Figure 6.16: Fraction of adsorbed molecules as a function of injected dose. We distinguish experiments with and without formation of a steady state level (open circles: observation of a steady state level; dots: no observation of a steady state level). Data correspond to experiments above 180K using the 8 or 15 mm escape aperture as in Figure 6.7.

Figure 6.16 shows the fraction of adsorbed molecules as a function of injected dose for the same set of data as displayed in Figure 6.7 corresponding to experiments above 180K using the 8 or 15 mm escape aperture. Experiments forming a steady state level are plotted as open circles while the ones not leading to a steady state level are presented as filled dots. Obviously, we take note of the same dose threshold as a function of the state of the surface as for k_{eff} in Figure 6.7. Similarly to Figure 6.7, but this time for the fraction of adsorbed molecules instead of k_{eff}, the dispersion below the threshold is so large that we can not draw any conclusion as far as the reversibility of these experiments is concerned. On the other hand, the experiments above the threshold present a reversibility of 80±20%. Apparently after participating in the formation of the liquid layer, most of the adsorbed molecules evaporate due to the significant vapor pressure of this solution.
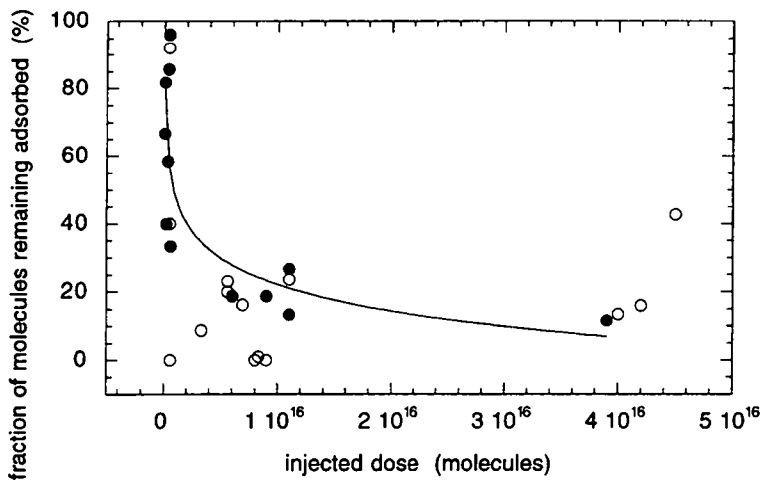
Figure 6.17: Fraction of adsorbed molecules as a function of injected dose. The dots represent experiments on a fresh ice sample (fitted by solid line) while the open circles correspond to experiments on a previously exposed ice surface. Data correspond to experiments above 180K using the 8 or 15 mm escape aperture.

Figure 6.17 shows the fraction of adsorbed molecules as a function of injected dose for the same experiments as in Figure 6.16. This time however, we discriminate between first uptake experiments (on fresh samples) and consecutive uptake experiments (samples with accumulated dose), and represent the injected dose on a linear scale. Most of the consecutive experiments

correspond to a dose above the threshold of $8 \cdot 10^{14}$ injected molecules. However, the experiments on a fresh sample are distributed more evenly as a function of dose. A logarithmic fit (curve in Figure 6.17) reveals a dose dependent reversibility: the higher the injected dose, the larger the reversibility. This feature is compatible with the picture of a bottleneck mentioned for the experiment displayed in Figure 6.8: there is competition between irreversible diffusion into the bulk and reevaporation from the surface.

6.3.5 Analysis of the Steady State Experiments

It follows from the negative temperature dependence of k_{eff} and the discussion of the steady state levels by noting the disagreement between k_{ads} and k_{eff} that the adsorption mechanism of HCl on ice is more complex than given by the two-state adsorption Scheme given by equation 5. In fact, we have to assume that the adsorption rate law is not of first order in HCl. In spite of this fact, we may calculate $k_{uni} = \dfrac{I_0 - I}{I} k_e$ from the steady state experiments using the 4 mm
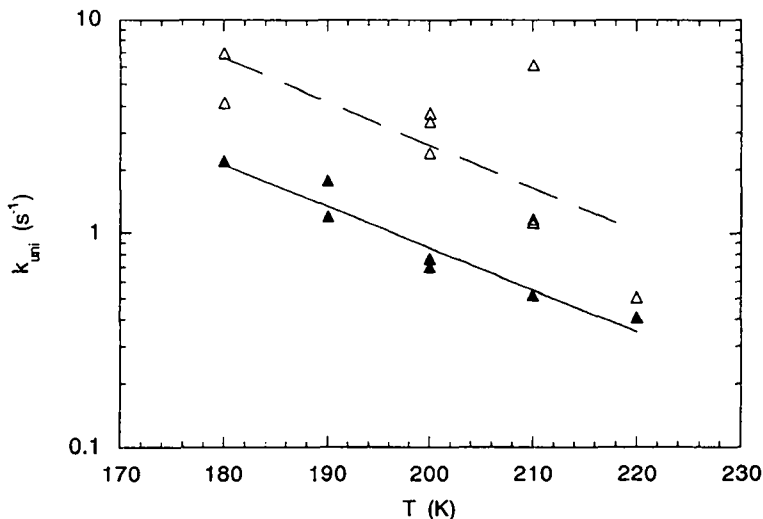
Figure 6.18: Arrhenius plot of k_{uni} determined in steady state experiments using the 4 mm escape aperture. The filled triangles represent experiments on a fresh ice sample (fitted by solid line) while the open triangles correspond to uptake experiments on a previously exposed sample (fitted by dashed line). Flowrates are confounded.

orifice (k_e=0.64 s^{-1}). Representing the calculated values of k_{uni} in an Arrhenius plot **(Figure 6.18)** yields a negative activation energy, namely 3.6±0.5 kcal/mol independent on the state of the surface (previously exposed or fresh ice). On the other hand, the values of k_{uni} corresponding to uptake experiments on a fresh ice sample are smaller by a factor of at least two compared to the ones on a previously exposed sample. However, even the values of k_{uni} in the case of a previously exposed sample are smaller by a factor of 3 to 4 than the ones for k_{eff} determined in pulsed valve experiments. We attribute this behaviour to a possible pressure dependence of the adsorption mechanism. In fact, steady state experiments performed on previously exposed samples by Flueckiger [27] using the 15 mm escape aperture yield k_{uni} varying from 12 to 23 s^{-1} over the temperature range of 180 to 210K. These values are larger by a factor of three at least compared to the experiments presented here using the 4 mm orifice. Planned experiments using the 8 mm escape aperture should give further insight into the detailed adsorption mechanism of HCl on ice.

6.4 Conclusion

The uptake kinetics of HCl on ice has been measured in the temperature range of 180 to 210K using two different techniques referred to as steady state and pulsed valve experiments and are discussed as a function of surface state. In fact, some of the pulsed valve experiments present a relaxation to a steady state level which depends only on temperature and escape orifice but not on the injected dose. Due to this feature and the operation of a two orifice reactor, we can calculate an instantaneous vapor pressure. Comparison to the phase diagram of HCl solutions and their respective hydrates [17], [28] shows that this vapor pressure corresponds to the coexistence line of "ice" and a solution of a HCl having a specific concentration at a given temperature. The threshold of injected dose leading to this liquid layer is estimated to be $8\pm2\cdot10^{14}$ molecules. This threshold corresponding to 22% of a formal monolayer may be explained by small domains of solution forming on the ice surface. As Molina and coworkers observed that diffusion of HCl is much faster in ice samples having visible imperfections like cracks [29], one might suggest that these domains also form along these cracks or grain boundaries. In fact, based on the observed bottleneck, the HCl molecules may accumulate in the cracks and start the solution process at these crystal imperfections. No clear temperature dependence of the threshold could be observed so far which may be due to the small range of concentrations of the respective solutions in the investigated temperature range. In fact, the solutions on the coexistence line with ice have a concentration varying roughly between 20 and 25%wt in the temperature interval of 220 to 186K. On the other hand, the suggested liquid layer has been observed even below the eutectic point of 186K [28] thus corresponding to the formation of a supercooled liquid. Within the detection limit, no difference in k_{eff} has been observed for pulses on the liquid or on a previously exposed sample without formation of the liquid. However, the k_{eff} data are widely scattered. Moreover, the decay of the gas phase HCl is always of single exponential type. As the temperature specific steady state levels are reached immediately, we suggest that the liquid forms on a time scale which is at least an order of magnitude faster than the adsorption process. The ice surface being very dynamic at these temperatures (see Chapter 5), the mixing of the H_2O and HCl molecules to form a given solution must be fast while sufficient water molecules are available.

We may assume that the solution layer is also formed during steady state experiments as soon as the pressure is high enough. Furthermore, the fact that the uptake remains constant over minutes (no saturation) is consistent with the

existence of this solution layer which apparently grows as HCl is incorporated into the sample. A change in steady state uptake only appears when the amount of adsorbed HCl approaches that of water molecules in the ice sample. Reference experiments on solutions of known concentration need to be performed. Furthermore, the state of the surface during such a constant uptake in a steady state experiment could be probed by pulsed valve experiments. Moreover, these constant steady state levels could be exploited for an analytical solution of a more complex adsorption mechanism taking into account diffusion processes. On the other hand, steady state experiments in the low pressure regime (HCl partial pressures of 10^{-7} Torr typical of the stratosphere) could yield further information on the reversibility of the HCl uptake on ice. So far, the reversibility above 180K has been investigated by means of pulsed valve experiments. In the case of pulses forming a solution layer, a fraction of 20±20% of the injected molecules remain permanently adsorbed on the surface. As far as the group of experiments on fresh ice is concerned, the reversibility presents a positive dose dependence in agreement with the picture of a bottleneck: When the accumulated dose of molecules at the surface becomes too large with respect to diffusion into the bulk, they are forced to wait on the surface with the possibility of desorbing back into the gas phase thus contributing to the reversibility of the system.

In the temperature range from 180 to 210K, the pulsed valve experiments yield values of k_{eff} roughly between 5 and 25 s^{-1} while k_{uni} determined by steady state experiments using the 4 mm escape aperture takes values that are significantly lower varying from 0.4 to 7 s^{-1}. Flueckiger [27], however, has observed values of k_{uni} varying from 12 to 23 s^{-1} using the 15 mm escape aperture thus being in agreement with the pulsed valve experiments. Moreover, the negative activation energy of -1.6±0.7 kcal/mol determined for k_{eff} is in agreement with the one for k_{uni} observed by Flueckiger in steady state experiments (-1.9±0.25 kcal/mol).

    The feature of orifice dependent steady state levels not only allows one to calculate an equilibrium vapor pressure but also the corresponding rates of accommodation and evaporation. While the rate of evaporation varies from $0.35 \cdot 10^{15}$#/s at 180K to $19.3 \cdot 10^{15}$#/s at 220K, the rate constant corresponding to unimolecular adsorption presents a slightly negative temperature dependence taking values between 5.7 and 4.6 s^{-1} in the same temperature interval (Table 6.1.b). Moreover, these last values are smaller by a factor of two compared to the ones determined by pulsed valve experiments. This disagreement together with the negative temperature dependence indicates that the adsorption mechanism is complex.

Although no dose dependence has been observed in the presented pulsed valve experiments, the fact that the determination of k_{uni} is dependent on the orifice size points towards a pressure dependence of the adsorption mechanism as it has been observed also by steady state experiments at 180K (see Figure 6.2). Before kinetic modeling can be undertaken, this pressure dependence must be assessed by additional steady state experiments using the escape apertures of 8 and 15 mm diameter.

6.5 References

[1] Toon, O.B. and Tolbert, M.A., Nature, 375, 218, 1995.

[2] Tabazadeh, A. et al., Geophys. Res. Lett. 21, 1619, 1994.

[3] Molina, M. J., T. L. Tso, L. T. Molina, and F. C. Y. Wang, Science, 238, 1253, 1987.

[4] Tolbert, M. A., M. J. Rossi, R. Malhotra, and D. M. Golden, Science, 238, 1258, 1987.

[5] Leu, M.-T., Geophys. Res. Lett., 15, 851, 1988.

[6] Hanson, D. R., and A. R. Ravishankara, J. Geophys. Res., 96, 5081, 1991.

[7] Abbatt, J. P. D., and M. J. Molina, Geophys. Res. Lett., 19, 461, 1992.

[8] Hanson, D. R., and A. R. Ravishankara, J. Phys. Chem., 96, 2682, 1992.

[9] Leu, M.-T., Geophys. Res. Lett., 15, 17, 1988.

[10] Tolbert, M. A., M. J. Rossi and D. M. Golden, Science, 240, 1018, 1988.

[11] Krishnan, P.N. and Salomon, R.E, J. Phys. Chem., 73, 2680, 1969.

[12] Seidensticker, R.G., J. Chem. Phys., 56, 2853, 1972.

[13] Gross, G.W.; Wong, P.M. and Humes, K., J. Chem. Phys., 67, 5264, 1977.

[14] Hanson, D. R., and K. Mauersberger, Geophys. Res. Lett., 15, 1507, 1988.

[15] Hanson, D. R., and K. Mauersberger, J. Phys. Chem., 94, 4700, 1990.

[16] Molina, M.J., Zhang, R., Woolridge, P.J., McMahon, J.R., Kim, J.E., Chang, H.Y. and Beyer, K.D., Science, 262, 1418, 1993.

[17] Molina, M. J., The probable role of stratospheric 'ice' clouds: Heterogeneous chemistry of the "Ozone Hole," in "The Chemistry of the Atmosphere: Its Impact on Global Change", edited by J. G. Calvert, Blackwell, Oxford, United Kingdom, 1994.

[18] Wolff, E.W., Mulvaney, R. and Oates, K., Geophys. Res. Lett., 16, 487, 1989.

[19] Chu, L.T. and Leu, M.-T., Paper presented at CHEMRAWN VII Conference, 1991.

[20] Dominé, F., Thiebert, E., Van Landeghem, F, Silvente, E. and Wagnon, P., Geophys. Res. Lett., 21, 601, 1994.

[21] Delzeit, L., Rowland, B. and Devlin, J.P., J. Phys. Chem., 97, 10312, 1993.

[22] Graham, J.D. and Roberts, J.T., Geophys. Res. Lett., 22, 251, 1995.

[23] Horn, A. B., Chesters, M.A., McCoustra, M.R.S. and Sodeau, J.R., J. Chem. Soc. Faraday Trans., 88, 1077, 1992.

[24] Gertner, B.J. and Hynes, J.T., Science, 271, 1563, 1996.

[25] Woolridge, P.J., Zhang, R. and Molina, M.J., J. Geophys. Res., 100, 1389, 1995.

[26] Handbook of Chemistry and Physics, 68th edition, CRC Press, Boca Raton, Florida, 1987.

[27] Flueckiger, B., unpublished results, 1996.

[28] Abbatt, J.P.D., Beyer, K.D., Fucaloro, A.F., McMahon, J.R., Woolridge, P.J., Zhang, R. and Molina, M.J., J. Geophys. Res., 97, 15819, 1992.

[29] Molina, M.J., Tso, T.-L., Molina, L.T. and Wang, F.C.-Y., Science, 238, 1253, 1987.

Chapter Seven - Outlook

While a detailed conclusion for each investigated system is given at the end of the respective chapter, we present here a list of experiments and technical improvements that will or might be implemented in the next future. On the other hand, it is up to the modellers to investigate the potential impact of the present observations on the evolution of the atmosphere. In what follows, we present some ideas of further investigation that may be conducted on the different systems.

7.1 Outlook for the System of NO₂ on Commercial Carbon Samples

The results presented in Chapter 3 are just the first stepping stone in our detailed understanding of the kinetic behavior of amorphous carbon. Future investigation may focus on two areas. First, aging processes of amorphous carbon are of interest as they are characterized by a changing distribution of functional groups on the surface of the amorphous carbon particles. Second, the heterogeneous kinetics of NO_2 on carbon will be studied as a function of temperature in view of their particular importance for the modeling of aircraft wakes [1].

At the same time, the rate of HONO formation as observed on acetylene soot has to be verified on the commercial samples. In fact, it is not clear so far whether the product analysis on these samples was made only after prolonged pumping. In this case, no HONO was observed in spite of lamp heating because the initial water content of the sample had been reduced by pumping. Therefore it has to be checked if a fresh sample shows any HONO formation. On the other hand, the activation by exposure to ozone is a new technique of sample preparation, and its effect on the commercial samples, in particular a change in hydrophobicity, has to be tested.

Moreover, one has to think of a sensitive method for sample analysis with respect to products that remain on the carbon surface, for instance CO and HNO_3. There are two major problems: First, this method must be very sensitive as the amount of product to be quantified is very small compared to the bulk of carbon, and second, the sample may be altered by exposure to ambient pressure while transferred from the vacuum compartment to the analysis system, reason for which one may suggest optical *in situ* probing.

Finally, a potential mass dependence of the uptake kinetics may be checked using a sample preparation that allows homogeneous deposition of very small quantities, for instance by preparation of suspensions and subsequent solvent evaporation off the sample substrate.

7.2 Outlook for the System of NO_2 on Acetylene Soot with subsequent HONO Formation

Systematic measurements of the water content of the acetylene samples and its temperature dependent desorption has to be investigated. In particular it has to be checked under which conditions, that is duration of exposure to ozone and partial pressure of water, the samples may take up water and are subsequently regenerated with respect to HONO formation.

On the other hand, concurrent experiments of a mixture of NO and NO_2 should be performed at various partial pressures in order to elucidate the mechanism of HONO formation.

Finally, the present flow calibration of HONO may be compared to an external HONO source developed by Fenter [2] and the conversion of HNO_3 into NO_2 should be checked by LIF detection of NO_2 and NO.

7.3 Outlook for the System of Water Vapor on Ice

A new technique of distinguishing experimentally between the rate of condensation and the rate of evaporation is by performing pulsed valve experiments using water of the isotope H_2O^{18}, that is water which contains a heavy oxygen atom. In such experiments gas phase H_2O^{18} is injected and interacts with bulk ice of normal water while evaporation of H_2O^{18} is still negligible. Another advantage of these experiments is the better detection limit needed to verify such a subtle effect as the dose dependence of the rate of condensation. In fact, we would be able to use direct MS detection at m/e20 without lock-in amplification due to the practical absence of evaporating molecules leading to a high level of background water. At 200K, the experiments of water on ice revealed that the ice surface is very dynamic while the uptake experiments of HCl on ice showed that an impinging molecule is swallowed immediately by the surface. In other words, the ice surface at the investigated temperatures is very "open". The experiments using isotopic water may elucidate furthermore the mechanism by which H_2O is incorporated into ice.

Experiments at low temperatures as we perform them are very sensitive to potential impurities that are trapped on the sample surface. The subtle effect of the dose dependence has to be checked against these impurities, that is, we have to find a technique to analyze the ice sample for trace substances. On the other hand, it has been shown by Allanic and Oppliger [3], that experiments on vapor condensed water ice give a better reproducibility compared to the ones on bulk ice. This may be due to the presence of cracks and other irregularities in the surface structure of bulk ice. For this reason, the projected experiments will be performed primarily on vapor deposited ice samples. Another way of sample preparation is to condense water vapor on the low temperature support in the presence of ambient air (1atm). A white condensate appears in this case which might be compared to snow. Experiments not presented in this work showed that the vapor pressure of such a sample was higher by almost an order of magnitude compared to that of the normal sample. On the other hand, the interaction HCl with this type of sample was faster than on the conventional sample.

At the moment of this writing, experiments are performed in order to assess as up to which decay constant a decaying burst of molecules may be followed using the present reactor geometry. These experiments are then compared to Monte Carlo simulations of the gas kinetics [4]. These simulations should also provide insight into what happens in the reactor in the 20ms following the injection of a burst of molecules. In fact, the MS signals have not been evaluated so far for this period of the rise time of the pulse.

7.4 Outlook for the System of HCl on Ice

From the preceding discussion, we conclude that future experiments of HCl on ice should be performed without lock-in amplification and on condensed water ice samples in order to have a larger signal to noise ratio as well as a better reproducibility of the data. Moreover, it has been observed [5] that diffusion of HCl into the bulk is much faster on samples with visible imperfections like cracks or gas inclusions. Therefore, it is important to use ice samples that are as homogeneous as possible.

So far it is not clear whether the steady state experiments point towards a pressure dependence of the uptake or not, and in which temperature range such a pressure dependence may be observable and/or significant. Therefore, systematic steady state experiments have to be performed using the 4, 8 and 15mm orifices. It appears that relatively fast reactions such as the uptake of HCl on ice must be investigated using a yardstick, that is k_e, of the same order of

k_{uni}. As it is difficult using the present experimental setup to increase the orifice diameter, we suggest to decrease the sample surface on the low temperature support in order to establish competition between adsorption on the ice and effusion from the reactor.

The fact that a relatively stable level of uptake is reached within a few seconds in the steady state experiments might be exploited in a steady state approximation. In fact, using two different orifices combined with two flow regimes (low and high flow) yields a set of four steady state equations with respect to the gas phase concentration. Furthermore, during such steady state experiments, the surface could be probed by pulsed valve experiments. Another idea would be to perform HCl uptake experiments on solutions of known HCl concentration for comparison.

In order to assess the influence of the accumulated dose, either a very strict experimental protocol has to be followed or/and continuous acquistion of the m/e36 signal is needed.

While investigation of the surface by optical methods [5] is an experimental improvement in the long term, the measurement of the electrical conductivity seems to be an easier and less expensive proposition. According to Abbatt et al. [6] this method allows one to determine if an electrolytic solution on the ice surface remains liquid or not.

Finally, as soon as the present observations are confirmed, completed and well quantified, chemical kinetic modeling will be performed. Eventually, the ice surface will have to be subdivided into several layers in order to account for 3-dimensional processes like diffusion and increasing thickness of the liquid solution.

7.5 References and Notes

[1] AERONOX, The Impact of NO_x Emissions from Aircraft Upon the Atmosphere at Flight Altitudes 8-15km, editor: U. Schumann, EC-DLR Publication on Research related to Aeronautics and Environment,1995.

[2] Fenter, F.F. and Rossi, M.J., J. Phys. Chem., 100, 13765, 1996.

[3] Allanic, A.; Oppliger, R., private communication.

[4] Fenter, F.F.; Caloz, F.; Tabor, K.; Gutzwiller, L.S. and Rossi, M.J., in preparation.

[5] Molina, M.J., Tso, T.-L., Molina, L.T. and Wang, F.C.-Y., Science, 238, 1253,
     1987.

[6] Abbatt, J.P.D., Beyer, K.D., Fucaloro, A.F., McMahon, J.R., Woolridge, P.J.,
     Zhang, R. and Molina, M.J., J. Geophys. Res., 97, 15819, 1992.

Appendix: Solution Strategy for Model Simulation

The goal is to find a set of the 6 fit parameters which approaches best the 6 experimental observables. The natural fit parameters of our model are k1 to k6. As we are conducting perturbation experiments, we may write a steady state condition for each species intervening in the mechanism, that is for G, P, S and I:

$$\frac{dG}{dt} = 0 = -k_e G_{ss}^L - k_1 G_{ss}^L S_{ss}^L + k_2 I_{ss}^L - k_5 G_{ss}^L P_{ss}^L + k_6 P_{ss}^L \qquad (1)$$

$$\frac{dS}{dt} = 0 = -k_1 G_{ss}^L S_{ss}^L + k_2 I_{ss}^L + k_3 I_{ss}^L - k_4 S_{ss}^L P_{ss}^L \qquad (2)$$

$$\frac{dI}{dt} = 0 = k_1 G_{ss}^L S_{ss}^L - k_2 I_{ss}^L - k_3 I_{ss}^L + k_4 S_{ss}^L P_{ss}^L \qquad (3)$$

$$\frac{dP}{dt} = 0 = k_3 I_{ss}^L - k_4 S_{ss}^L P_{ss}^L \qquad (4)$$

Writing these four equations (=steady state conditions) for one orifice (L=large) shows that (2) and (3) are linearly dependent so that only (1), (2) and (4) are linearly independent equations. This is due to the fact that we have a restrictive condition in our mechanism, namely the conservation of S and I: $S+I=S_0$. In the above equations intervene not only the 6 fit parameters but also the variables expressing the steady state concentration at the orifice under consideration, i.e. G_{ss}^L, S_{ss}^L, P_{ss}^L and I_{ss}^L.

On the other hand we are modeling experiments performed using two different orifices leading to a total of 6 linearly independent steady state conditions and two sets of steady state concentrations presented in the table below as two sets of 4 variables. Of this total of 8 variables, the two Gss are determined from experiment and are therefore called dependent. Furthermore, I_{ss}^i and S_{ss}^i are related to each other by $S+I=S_0$, where i corresponds to the large (L) and the small (S) orifice, so that only one of them is independent, let's say S_{ss}^i. This yields 4 dependent and 4 independent variables in the following table. This table is a summary of the observables, fit parameters and dependent and independent variables that intervene in our model calculation.

To sum up, we have 6 fit parameters (=rate constants) and 4 independent variables that interact in the simulation. We call this total of 10 entities the 10 unknowns. They are related to each other by the 6 (linearly independent) steady state conditions, and consequently 4 of them are undetermined corresponding to 4 degrees of freedom. We chose them as being k_1, k_3, k_5 and P_{ss}^L and call them the new fit parameters. In our case, some variables are more adequate to be

chosen as independent variables than others. For instance we know that k_1 and k_5 must be smaller or equal to ω, the sample collision frequency. In order to achieve the dose dependence, k_5 (auto-catalytic process) should be larger than k_1. That's why it is more convenient to chose k_1 and k_5 as independent variables and their reverse rate constants (k_2 and k_6) as the corresponding dependent variables. Furthermore we know that we need a low steady state concentration for P in order to get the required dose dependence, that's why it is convenient to chose it also as an independent variable rather than the remaining rate constants k_3 and k_4. This shows that it is most appropriate to chose the most hidden parameters as dependent variables which are in our case the rate constants of surface transformation k_3 and k_4.

6 experimental observables	G_{SS}(L,expt), k_{eff}(L, low dose), k_{eff}(L, high dose)
	G_{SS}(S,expt), k_{eff}(S, low dose), k_{eff}(S, high dose)
- of which are time independent	G_{SS}(L,expt), G_{SS}(S,expt)
- of which are time dependent	k_{eff}(L, low dose), k_{eff}(L, high dose)
	k_{eff}(S, low dose), k_{eff}(S, high dose)
6 initial fit parameters	$k_1, k_2, k_3, k_4, k_5, k_6$
variables	G_{SS}(L), S_{SS}(L), P_{SS}(L), I_{SS}(L), G_{SS}(S), S_{SS}(S), P_{SS}(S), I_{SS}(L)
- of which are dependent	G_{SS}(L,model)=G_{SS}(L,expt), I_{SS}(L)=S_0-S_{SS}(L),
	G_{SS}(S,model)=G_{SS}(S,expt), I_{SS}(S)=S_0-S_{SS}(S)
	S_0 is supposed to be known from theory
- of which are independent	S_{SS}(L), P_{SS}(L), S_{SS}(S) and P_{SS}(S)
10 unknowns	$k_1, k_2, k_3, k_4, k_5, k_6$ and
	S_{SS}(L), P_{SS}(L), S_{SS}(S), P_{SS}(S)
4 new fit parameters	k_1, k_3, k_5, P_{SS}(L),
11 unknowns	$k_1, k_2, k_3, k_4, k_5, k_6$ and
	S_{SS}(L), P_{SS}(L), S_{SS}(S), P_{SS}(S) G_{SS}(S,model)
5 new fit parameters	k_1, k_3, k_5, P_{SS}(L) and S_{SS}(L),

Calculating the dependent variables it may occur, of course, that we get a negative value for one of them, which does not correspond to a physical solution. It can even be difficult to find a set of rate constants that are all positive. In such a case it is convenient to draw a table displaying the variation of the dependent variables as a function of the independent ones.

In the above case, it turns out that the 4 fit parameters k_1, k_3, k_5 and P_{ss}^L do not afford sufficient flexibility in order to find an overall good fit to the 4 time dependent experimental observables $k_{eff}(L, \text{low dose})$, $k_{eff}(L, \text{high dose})$, $k_{eff}(S, \text{low dose})$, $k_{eff}(S, \text{high dose})$. One simple approach is to make a table of how the dependent variables depend on each other.

The idea is therefore to admit an error of 30% on two of the experimental observables. Being aware of the day to day variation of the steady state concentrations $G_{ss}(L, \text{expt})$ and $G_{ss}(S, \text{expt})$, it seems to be reasonable to choose these two (time independent) experimental observables that correspond to the two dependent variables $G_{ss}(L, \text{model})$ and $G_{ss}(S, \text{model})$. Consequently we can write:

$$Gss(L, \text{model}) = Gss(L, \text{expt}) \pm 30\%$$

and $\qquad Gss(S, \text{model}) = Gss(S, \text{expt}) \pm 30\%$.

By this procedure, we may assume that $Gss(S, \text{model})$ is not a strictly dependent variable anymore but becomes an independent variable. As it may be assimilated to an unknown, we have so formally increased the total number of unknowns to 11. Applying the 6 steady state conditions on these 11 unknowns then yields 5 new fit parameters: k_1, k_3, k_5, P_{ss}^L and S_{ss}^L .

The most obvious way to get more flexibility when modeling pulsed valve experiments is of course by increasing the number of rate constants. Generally, this implies increasing the number of species intervening in the mechanism. However, if we increase the number of species, we also increase the number of steady state conditions. In our case, with a two aperture reactor, for each added species we also introduce two more steady state conditions. In order to increase effectively the number of degrees of freedom, we therefore have to introduce more than two rate constants into the mechanism for each species added.

Algebraic Development

The detailed development of the above strategy goes as follows. First we solve the three linearly independent equations (1), (2) and (3) for the fit parameters k_2, k_4 and k_6. Namely, from equation 4:

$$k_4 = \frac{k_3 I_{ss}^L}{S_{ss}^L P_{ss}^L} \tag{5}$$

When k4 is introduced into equation 2 and solved for k2 we obtain:

$$k_2 = \frac{k_1 G_{ss}^L S_{ss}^L}{I_{ss}^L} \tag{6}$$

Upon inserting k2 into relation (1):

$$k_6 = \frac{k_e G_{ss}^L + k_5 G_{ss}^L P_{ss}^L}{P_{ss}^L} \tag{7}$$

The three rate constants k2, k4 and k6 are expressed as a function of k1, k3, k5, G_{ss}^L, P_{ss}^L, S_{ss}^L and I_{ss}^L of which only G_{ss}^L is known, and S_{ss}^L and I_{ss}^L are related to each other by I(t) + S(t) = S0, that is $I_{ss}^L - S_{ss}^L = S_0$. Using this approach of expressing three of the rate constants as a function of the initial conditions for the large orifice ascertains that all the concentrations relax to their initial value as must be the case in a perturbation experiment. In other words, the boundary conditions are satisfied for all species and any value of the (remaining) fitting parameters. In practice, this allows also to check whether the coupled differential equations in the program and the expressions of the calculated rate constants are correct. When all the species relax to the initial steady state level, we can be sure that there is no mistake of spelling or algebra in the program. This is a useful test, especially when developing mechanisms.

So far we have only used the steady-state conditions for the large orifice reactor. In order to obtain a consistent set of rate constants valid for both orifice reactors, we also need to take into account the steady-state conditions corresponding to the small orifice reactor in view of the additional observable Gss(S). Writing these conditions, the approach consists in solving them for the steady-state concentrations G_{ss}^S, P_{ss}^S, S_{ss}^S and I_{ss}^S instead of the still unknown rate constants k1, k3 and k5. This in spite of the fact that G_{ss}^S is known from the experiment. In fact, it can be shown that using the exact values of G_{ss}^L and G_{ss}^S, we do not obtain a good overall fit. The agreement is greatly improved if we admit to an uncertainty of about 30% for these values (see Table). Keeping in mind the day-to-day variation of the steady-state signal levels, 30% uncertainty is reasonable. From the steady-state conditions 1 to 4 written for the small instead of the large orifice reactor and solved for the initial concentrations we find:

$$P_{ss}^S = \frac{1}{k_5} \cdot \left(\frac{k_1 \cdot k_3 \cdot k_6}{k_2 \cdot k_4} - k_e^S \right) \tag{8}$$

$$G_{ss}^{S} = \frac{k_2 \cdot k_4 \cdot P_{ss}^{S}}{k_1 \cdot k_3} \tag{9}$$

$$S_{ss}^{S} = \frac{k_2 S_0}{k_1 G_{ss}^{S}} \bigg/ \left(1 + \frac{k_2}{k_1 G_{ss}^{S}}\right) \tag{10}$$

$$I_{ss}^{S} = S_0 - S_{ss}^{S} \tag{11}$$

where each expression is a function of the preceding one.

As we note from equation 8, we do not use the experimental observable G_{ss}^{S} in order to determine an additional rate constant but, to the contrary, we try to fit it as a function of the remaining degrees of freedom such as k_1, k_3, k_5, P_{ss}^{L} and S_{ss}^{L}. In other words, for each simulation we have to compare the calculated value of G_{ss}^{S} to the experimental one. In practice, it is rather easy to obtain good agreement for k_{dec} as well as for G_{ss}^{S}. In general, a steady state value too low by 30% had to be chosen for the large orifice, resulting in a 30% too high value for the small orifice.

FORTRAN Routine used together with the March 30, 1987 Version of the "Isode livermore solver" developed by Alan C. Hindmarsh

Reference: George D. Byrne and Alan C. Hindmarsh, Stiff ODE Solvers: A Review of Current and Coming Attractions, Journal of Computational Physics, 1987, 70,1.

```
     PROGRAM COMPLMECH
     EXTERNAL FEX, JEX
     DOUBLE PRECISION ATOL,RWORK,RTOL,T,TOUT,Y,YD
     DIMENSION Y(8),ATOL(8),RWORK(220),IWORK(55),YD(8)
     COMMON GAMMA,ALPHA,BETA,FLOW_IN,FOUT,FOUTM,
     COMMON CONESCB,CONESCM
     COMMON
CON1,CON2,CON3,CON4,CON5,CON6,CON7,CON8,CON9,CON10
     COMMON CON11,CON12


     ACCEPT 90,CON1           interactive input of a fit parameter
```

```
   90 FORMAT(F15.0)


      CONESCB=7.5                      defintion of kₑ and Fₛₛ resp Gₛₛ for
both orifices
      CONESCM=1.0                      and the dose
      FOUT=1.1
      FOUTM=0.16
C     GSSB=FOUT/7.5
C     GSSM=FOUTM/1
      DOSE_LO=0.14
      DOSE_HI=13.5


      STOT= 1.1            definition of the number of surface sites for the
large orifice
      PB= 0.05
      SB= 0.2
      BI= stot-sb
      SM=SB
      CON1= 50             definition of the remaining fit parameters
      CON3= 500
      CON5 = 150
      CON8 = 0



C   from P:                           calculation of the 6 unknowns
      CON4 = (CON3*BI) / (PB*SB)           according to 6 linearly
independent
                                      steady state conditions

C   from S/I   (A=0):

      CON2 = (CON1*GSSB*SB)
      $    / (BI)

C   from G    (C=0):

      CON6 = (CONESCB*GSSB+CON5*GSSB*PB
      $     ) / (PB)

      APM = (CON2*CON4*CON5) /( CON1*CON3)              (intermediate
variables)

      BPM = (CON2*CON4*CONESCM) /( CON1*CON3) - CON6

      CPM = 0

      PM = (- BPM + SQRT(BPM**2 - 4*APM*CPM) )/ (2*APM)

      GSSM = (CON2*CON4*PM) /( CON1*CON3)   calculation of Gss for the
small                                      orifice simulation
      SoverI = CON2/(CON1*GSSM)
```

SM = SoverI*stot/(1+SoverI)

SIM = STOT - SM


```
      WRITE(6,5)CON2,con4,CON6,con7
    5 FORMAT('CON2='E11.4' CON4='E11.4' CON6='E11.4' con7='E11.4)
      WRITE(6,6)BI,con10,SB,PB
    6 FORMAT('BI='E11.4' con9='E11.4' SB='E11.4' PB='E11.4)
      WRITE(6,7)gssm,pm,sm,sim
    7 FORMAT('GSSM='E11.4' PM='E11.4' SM='E11.4' SIM='E11.4)
```

```
      NEQ = 8

      Y(1) = GSSB + DOSE_LO                definition of the 8 initial
conditions
C                    GASPHASE H2O
      Y(2) = PB
C                    PRECURSOR
      Y(3) = SB
C                    SITES
      Y(4) = BI
C                    intermediate


      Y(5) = GSSB + DOSE_HI
C                    GASPHASE H2O
      Y(6) = PB
C                    PRECURSOR
      Y(7) = SB
C                    SITES
      Y(8) = BI
C                    intermediate


      T = 0.0D00                           definition of solver parameters
      TOUT = 0.0D-02
      ITOL = 2
      RTOL = 1.0D-08
      DO 10 JJ = 1,NEQ


  10 ATOL(JJ) = 1.0D-08
      ITASK = 1
      ISTATE = 1
      IOPT = 0
      LRW =212
      LIW = 28
      MF = 22
C

      write(3,12)GSSB,PB,BI,SB                        creating a data file
  12 format('GSSB='E11.4' PB='E11.4' BI='E11.4' SB='E11.4)
      WRITE(3,13)GSSM,PM,SIM,SM,CON1
  13 FORMAT('GSSM='E11.4' PM='E11.4'SIM='E11.4' SM='E11.4
     $ ' CON1='E11.4)
      WRITE(3,14)CON2,CON3,CON4,CON5,CON6
  14 FORMAT('CON2='E11.4' CON3='E11.4' CON4='E11.4' CON5='E11.4
     $ ' CON6='E11.4)
      WRITE(3,15)CON7,con8,CON9,con10
  15 FORMAT('CON7='E11.4' CON8='E11.4' CON9='E11.4' con10='E11.4)
      WRITE(3,17)
  17 FORMAT(' TIME LO_GAS LO_PREC HI_GAS HI_PREC HI_inter')

      G1_LO=LOG(Y(1) - GSSB)
```

```
      G1_HI=LOG(Y(5) - GSSB)

      DO 40 IOUT = 1,100
      CALL LSODE
(FEX,NEQ,Y,T,TOUT,ITOL,RTOL,ATOL,ITASK,ISTATE,IOPT,
     $        RWORK,LRW,IWORK,LIW,JEX,MF)

      WRITE(3,20)T,Y(1),Y(2),Y(5),Y(6),Y(8)
   20 FORMAT(E11.4,5E13.4)

      IF (TOUT .EQ. 0.02) THEN
        G5_LO=LOG(Y(1) - GSSB)
        G5_HI=LOG(Y(5) - GSSB)
        DECAY_LO = (G1_LO - G5_LO)/0.02
        DECAY_HI = (G1_HI - G5_HI)/0.02
      END IF

      IF(ISTATE .LT. 0) GO TO 80
   40 TOUT = TOUT + 0.01                    definition of the time
resolution


                              interactive check of the decay
constants                             and some calculated
unknowns

      WRITE(6,50) DECAY_LO,DECAY_HI,PB_final,con4
   50 FORMAT('DECAY_LO='E11.4' DECAY_HI='E11.4' final_PB='E11.4
     $       ' CON4='E11.4)

      WRITE(3,56)DOSE_LO,DECAY_LO,DOSE_HI,DECAY_HI
   56 FORMAT('DOSE_LO='E11.4' DECAY_LO='E11.4' DOSE_HI='E11.4'
     $       DECAY_HI='E11.4)

      STOP
   80 WRITE(3,91) ISTATE
   91 FORMAT(///22H ERROR HALT.. ISTATE =,I3)
      STOP
      END
C
C
      SUBROUTINE FEX(NEQ,T,Y,YDOT)         Subroutine where the
coupled
      DOUBLE PRECISION T,Y,YDOT            differential equations are
defined.
      DIMENSION Y(8),YDOT(8)

      COMMON GAMMA,ALPHA,BETA,FLOW_IN,FOUT,FOUTM
      COMMON CONESCB,CONESCM
      COMMON
CON1,CON2,CON3,CON4,CON5,CON6,CON7,CON8,CON9,CON10
      COMMON CON11,CON12
```

```
C     WRITE(3,'(2X,5E12.4)') (Y(I),I=1,3)
C
C  DIFF EQUATIONS FOR LOW DOSE

      YDOT(1) = - CONESCB*Y(1) + CON2*Y(4) - CON1*Y(1)*Y(3)
     $       - CON5*Y(1)*Y(2) + CON6*Y(2)


      YDOT(2) =
     $       + CON3*Y(4) - CON4*Y(2)*Y(3)


      YDOT(3) = + CON2*Y(4) - CON1*Y(1)*Y(3)
     $       + CON3*Y(4) - CON4*Y(2)*Y(3)


      YDOT(4) = - CON2*Y(4) + CON1*Y(1)*Y(3)
     $       - CON3*Y(4) + CON4*Y(2)*Y(3)



C   DIFF EQUATIONS FOR HIGH DOSE

      YDOT(5) = - CONESCB*Y(5) + CON2*Y(8) - CON1*Y(5)*Y(7)
     $       - CON5*Y(5)*Y(6) + CON6*Y(6)


      YDOT(6) =
     $       + CON3*Y(8) - CON4*Y(6)*Y(7)


      YDOT(7) = + CON2*Y(8) - CON1*Y(5)*Y(7)
     $       + CON3*Y(8) - CON4*Y(6)*Y(7)


      YDOT(8) = - CON2*Y(8) + CON1*Y(5)*Y(7)
     $       - CON3*Y(8) + CON4*Y(6)*Y(7)

C     WRITE(3,'(5E12.4)') (YDOT(I),I=1,3)
      RETURN
      END
C
      SUBROUTINE JEX (NEQ,T,Y,ML,MU,PD,NRPD)
      DOUBLE PRECISION PD,T,Y
      RETURN
      END
```

Acknowledgments

My best thanks go to Professor Hubert van den Bergh, director of the Laboratoire de Pollution Atmosphérique et Sol (LPAS), who spontaneously invited me to write a Ph.D. thesis. I also thank Dr. Michel J. Rossi who has successfully directed this work in an encouraging and constructive manner.

I would like to testify my gratefulness to the staff of the LPAS, in particular to Dr. Kevin Tabor who accompanied me in the pioneering phase of mounting the experiment, to Dr. Fred Fenter who gave critical inputs and to Axel Thielmann who carried out some of the experiments presented in this work as part of his diploma thesis. Moreover, I owe a lot to my fellow Ph.D. students Marçal Pires, François Caloz, Raoul Oppliger, Arnaud Allanic, Benoit Flueckiger, Patrick Füri and Pierre Voumard. A very special thank goes to Andres Thöny, Martin Forrer and Renato Zenobi who initiated me to winter mountaineering and with whom I spent very special moments outside of the lab. Furthermore, it is my pleasure to acknowledge the very collaborative attitude of our mechanic Flavio Comino: thanks to his calm hands no challenge was too tough.

Finally, the success of this work should also be considered as a reward to my parents, my brother and my two sisters for their continuous support, as well as to Cristina for her patience and attentive care. Of course, my sincerest thanks go also to all my friends who encouraged me in many ways during this work.

CURRICULUM VITAE

Name :	Lukas Stefan GUTZWILLER
Address :	Route Neuve 87
	1024 Ecublens
	Switzerland
	Tel: +41 21 691 94 30
Place, Date of Birth :	Zurich, August 16, 1966
Nationality :	Swiss

Education

1986-1992	Studies of **physics** at the Swiss Federal Institute of Technology in Lausanne. Undergraduate Thesis on aerosolphysics (fieldmeasurements on Mount Rigi, Central Switzerland) at the Laboratory for Atmospheric Physics at the Swiss Federal Institute of Technology in Zürich.
1992-1996	**Ph.D Thesis** "Heterogeneous Kinetics of some Atmospherically Relevant Reactions. Experiments and Modeling." at the Laboratory of Air and Soil Pollution of the Swiss Federal Institute of Technology in Lausanne.

Most important publications

Tabor, K.; Gutzwiller, L.; Rossi, M.J.: The Heterogeneous Interaction of NO_2 with Amorphous Carbon Geophys. Res. Lett., 1993, 20 (14), 1431.

Tabor, K.; Gutzwiller, L.; Rossi, M.J.: Heterogeneous Chemical Kinetics of NO_2 on Amorphous Carbon at Ambient Temperature, J. Phys. Chem. 1994, 98, 6172.

Gutzwiller, L.; Tabor, K.; Rossi, M.J.: Kinetics of Condensation and Evaporation of Water on Ice Surfaces between 160 and 220 K. submitted to J. Phys. Chem., 1996.

Language expertise

German:	mother tongue
French.	fluent with excellent writing skills
English:	fluent with good writing skills, First Certificate grade "A"
Spanish:	fluent with good writing skills
Italian:	basic knowledge
Portugese:	basic knowledge

Hobbies

Sports:	Mountaineering, dance, swimming
Music:	French Horn, self-made Alphorn, choir